Detailing Radio Frequency Controlled Hyperthermia and its Application in Ultrahigh Field Magnetic Resonance

DISSERTATION

zur Erlangung des akademischen Grades

doctor rerurm naturalium

(Dr. rer. nat)

im Fach Biophysik

eingereicht an der

Mathematisch-Naturwissenschaftlichen Fakultät I

der Humboldt-Universität zu Berlin

von

Dipl.-Ing. Lukas Winter

Präsident der Humboldt-Universität zu Berlin:

Prof. Dr. Jan-Hendrik Olbertz

Dekan der Mathematisch-Naturwissenschaftlichen Fakultät I:

Prof. Stefan Hecht, Ph.D.

Gutachter/in: 1. Prof. Dr. Thoralf Niendorf

2. Prof. Dr. Peter Wust

3. Prof. Dr. Beate Röder

Tag der mündlichen Prüfung: 15 Juli 2014

Acknowledgements

I would like to thank…

Prof Niendorf for his guidance, his trust and for giving me the freedom that I needed. Prof. Vrba and Prof. Wust for motivating me to pursue this project.

All B.U.F.F.'lers, collaborators, students and friends for the wonderful time and working atmosphere and for teaching me so much.

Moim kochanym rodzicom. Tą pracę dedykuję Wam. Dziękuję Wam za te piękne życie, które mi umożliwiliście. Nie mogę w przybliżeniu oddać Wam wszytko to, co od Was otrzymałem.

Der allerbesten Schwester auf der ganzen Welt.

Mi amor Blanca y mi hijo Leo. El equilibrio y la motivación de mi vida.

Last but not least I would like to thank everyone:

…who doesn't live in a nutshell

…who loves more than fears

…who has an open mind open mouth open heart

…who values the common goal above the individual gain

"Physics isn't the most important thing. Love is."

– Richard P. Feynman

Die vorliegende Arbeit wurde im Zeitraum von Januar 2010 bis Februar 2014 im Arbeitskreis von Prof. Dr. Thoralf Niendorf, in der Berlin Ultrahigh Field Facility (B.U.F.F.), Max-Delbrück Zentrum für Molekulare Medizin, Berlin, durchgeführt.

Auszüge aus dieser Arbeit wurden publiziert in:

A. Graessl, W. Renz, F. Hezel, M. Dieringer, **L. Winter**, Oezerdem C, P. Kellman, D. Santoro, T. Lindel, T. Frauenrath, H. Pfeiffer, and T. Niendorf, "Modular 32 Channel Transceiver Coil Array for Cardiac MRI at 7T," *Magnetic Resonance in Medicine,* 2014; 72(1):276-290.

L. Winter, C. Özerdem, W. Hoffmann, D. Santoro, A. Müller, H. Waiczies, R. Seemann, A. Graessl, P. Wust, and T. Niendorf, "Design and Evaluation of a Hybrid Radiofrequency Applicator for Magnetic Resonance Imaging and RF Induced Hyperthermia: Electromagnetic Field Simulations up to 14.0 Tesla and Proof-of-Concept at 7.0 Tesla," *PLOS ONE,* 2013; 8(4):e61661.

T. Niendorf, A. Graessl, C. Thalhammer, M. A. Dieringer, O. Kraus, D. Santoro, K. Fuchs, F. Hezel, S. Waiczies, B. Ittermann, and **L. Winter**, "Progress and promises of human cardiac magnetic resonance at ultrahigh fields: A physics perspective," *Journal of Magnetic Resonance,* 2012; 229(0):208-222.

C. Thalhammer, W. Renz, **L. Winter**, F. Hezel, J. Rieger, H. Pfeiffer, A. Graessl, F. Seifert, W. Hoffmann, F. Von Knobelsdorff Brenkenhoff, V. Tkachenko, J. Schulz-Menger, P. Kellman, and T. Niendorf, "Two-dimensional Sixteen Channel Transmit/Receive Coil Array for Cardiac MRI at 7.0 Tesla: Design, Evaluation and Application," *Journal of Magnetic Resonance Imaging,* 2012; 36(4):847-857.

L. Winter, P. Kellman, W. Renz, A. Gräßl, F. Hezel, C. Thalhammer, F. Von Knobelsdorff Brenkenhoff, V. Tkachenko, J. Schulz-Menger, and T. Niendorf, "Comparison of three multichannel transmit/receive radiofrequency coil configurations for anatomic and functional cardiac MRI at 7.0T: implications for clinical imaging," *European Radiology,*2012; 22(10): 2211-2220.

T. Niendorf, **L. Winter**, and T. Frauenrath, "Electrocardiogram in an MRI Environment: Clinical Needs, Practical Considerations, Safety Implications, Technical Solutions and Future Directions," in *Advances in Electrocardiograms - Methods and Analysis*, R. M. Millis, Ed., ed HR: Intech, pp. 309-324, 2012.

A. Gräßl, **L. Winter**, C. Thalhammer, W. Renz, P. Kellman, C. Martin, F. Von Knobelsdorff Brenkenhoff, V. Tkachenko, J. Schulz-Menger, and T. Niendorf, "Design, evaluation and application of an eight channel transmit/receive coil array for cardiac MRI at 7.0T," *European Journal of Radiology,* 2011; 82(5):752-759.

Zusammenfassung

Die vorliegende Arbeit untersucht die grundsätzliche Machbarkeit, Radiofrequenzimpulse (RF) der Ultrahochfeld (UHF) Magnetresonanztomographie (MRT) ($B_0 \geq 7.0$ T) für therapeutische Verfahren wie die RF Hyperthermie oder die lokalisierte Freigabe von Wirkstoffträgern und Markern zu nutzen. Bei höheren RF Frequenzen ($f > 300$ MHz) kann eine erhöhte Selektivität und Effizienz eines zu erwärmenden lokalen Zielgebietes erreicht werden, wie in der Arbeit mit Hilfe theoretischer Überlegungen unterlegt und mittels numerisch elektromagnetischer Feldsimulationen gezeigt wird. Um das Ziel eines hybriden MRT Systems mit gleichzeitiger RF Hyperthermieanwendung zu erreichen, wurden RF Multikanalspulen entwickelt, konstruiert, charakterisiert und evaluiert. Diese Neuentwicklungen wurden zunächst für die MR Bildgebung des Herzens und des Hirns bei 7.0 T eingesetzt, um deren grundsätzliche Eignung für die MRT Bildgebung aufzuzeigen. Der hierbei gewonnene Erkenntnisgewinn wurde genutzt, um die physikalischen, konzeptionellen und technischen Voraussetzungen für einen integrierten 8-Kanal Sende/Empfangsapplikator zu schaffen, der bei einer Protonenfrequenz von 298 MHz operiert. Mit diesem weltweit ersten System konnte in der Arbeit experimentell bewiesen werden, dass die entwickelte Hardware sowohl zielgerichtete lokalisierte RF Erwärmung als auch MR Bildgebung und MR Thermometrie (MRTh) realisiert. Der Applikator kann überdies mit einem in das MR System integrierten mehrkanaligen Sendesystem betrieben werden. Die hierzu erhobenen Ergebnisse zeigen, dass mit den zusätzlichen Freiheitsgraden (Phase, Amplitude) eines mehrkanaligen Sendesystems der Ort der thermischen Dosierung gezielt verändert bzw. festgelegt werden kann. In realitätsnahen Temperatursimulationen mit numerischen Modellen des Menschen, beruhend auf MRT Daten, wird in der Arbeit aufgezeigt, dass mittels des entwickelten Hybridaufbaus eine kontrollierte und lokalisierte thermische Dosierung im Zentrum des menschlichen Kopfes erzeugt werden kann. Nach der erfolgreichen Durchführung dieser Machbarkeitsstudie wurden in theoretischen Überlegungen, numerischen Simulationen und in ersten grundlegenden experimentellen Versuchen die elektromagnetischen Gegebenheiten von MRT und lokal induzierter RF Hyperthermie für Frequenzen größer als 298 MHz untersucht und bis auf eine Frequenz von 1.44 GHz ausgedehnt. In diesem Frequenzbereich konnte der Energiefokus in den benutzen Untersuchungsobjekten mit Hilfe spezialisierter RF Antennenkonfigurationen entscheidend weiter verkleinert werden, sodass Temperaturkegeldurchmesser von wenigen Millimetern erreicht wurden. Gleichzeitig zeigten die numerischen Simulationen der elektromagnetischen Felder, dass die vorgestellten Konzepte ausreichende Signalstärke der zirkular polarisierten Spinanregungsfelder (B_1^+) bei akzeptabler oberflächlicher Energieabsorption erzeugen, um eine potentielle Machbarkeit von *in vivo* MRT bei B_0=33.8T oder *in vivo* Elektronenspinresonanz (ESR) im L-Band zu demonstrieren.

Abstract

The presented work details the basic feasibility of using radiofrequency (RF) fields generated by ultrahigh field (UHF) magnetic resonance (MR) ($B_0 \geq 7.0$ T) systems for therapeutic applications such as RF hyperthermia and targeted drug delivery. Theoretical considerations and numerical electromagnetic field (EMF) simulations conducted in this work demonstrate the increased selectivity and efficiency for thermal dose applications at higher RF frequencies (f > 300 MHz). *En route* to an integrated MR system that supports RF hyperthermia application and imaging simultaneously, RF coil arrays were designed, constructed and evaluated. This novel RF technology was first applied in cardiac and brain MR imaging (MRI) at 7.0 T to examine and demonstrate the basic feasibility of this approach for *in vivo* imaging. The lessons learned from these pilot studies were employed to develop the physical, conceptual and technical underpinnings of a truly hybrid 8-channel transmit/receive (TX/RX) applicator operating at the 7.0 T proton MR frequency of 298 MHz. The proposed hybrid is a class of its own since it is the world's first. Experimental verification conducted in this work demonstrated that the hybrid applicator supports targeted RF heating, MR imaging and MR thermometry (MRTh). The applicator supports a single feeding RF power amplifier regime but can be also operated via multi-channel RF transmission hardware integrated into the MR scanner. The approach offers extra degrees of freedom (RF phase, RF amplitude) that afford deliberate changes in the location and thermal dose of targeted RF induced heating. While this approach makes additional RF hardware components (RF power amplifiers, RF electronics, filters, RF heating antennas) or software to drive these components obsolete, it allows for high spatial and temporal MR temperature mapping due to intrinsic signal-to-noise ratio (SNR) gain of UHF MR together with the enhanced parallel imaging performance inherent to the multi-channel receive architecture used. Temperature simulations in human voxel models revealed that the proposed hybrid setup is capable to deposit a controlled and localized RF induced thermal dose in the center of the human brain. After demonstrating basic feasibility, theoretical considerations and proof-of-principle experiments were conducted for RF frequencies of up to 1.44 GHz to explore electrodynamic constraints for MRI and targeted RF heating applications for a frequency range larger than 298 MHz. For this frequency regime a significant reduction in the effective area of energy absorption was observed when using dedicated RF antenna arrays proposed and developed in this work. Based upon this initial experience it is safe to conclude that the presented concepts generate sufficient signal strength for the circular polarized spin excitation fields (B_1+) with acceptable specific absorption rate (SAR) on the surface, to render *in vivo* MRI at B_0 = 33.8 T or *in vivo* electron paramagnetic resonance (EPR) at L-Band feasible.

List of Abbreviations

$\vec{\mu}$	magnetic moment
$\vec{J}$	total angular momentum
γ	gyromagnetic ratio
l	orbital quantum number
j	total angular momentum quantum number
s	spin quantum number
$\hbar$	quantum angular momentum
m_j	magnetic quantum number
h	Planck's constant
$\vec{H}_0$	static magnetic field
$\vec{B}_0$	static magnetic flux density
$\overrightarrow{e_x}, \overrightarrow{e_y}, \overrightarrow{e_z}$	unit vectors
E	energy
ω_0	Larmor precession frequency
t	time
$\vec{B}_1$	time varying magnetic flux density applied for spin energy level transitions
f_0	resonance frequency
γ_e	gyromagnetic ratio for a free electron
γ_p	gyromagnetic ratio for a free proton
e	elementary charge
m_e	electron mass
g_e	electron g-factor
μ_B	Bohr magneton
m_p	proton mass
g_p	proton g-factor
μ_N	nuclear magneton
N_+	spin ensemble parallel to an external static magnetic field
N_-	spin ensemble anti-parallel to an external static magnetic field
k_B	Boltzmann constant
T	temperature
ΔN	spin excess
N_A	Avogadro's constant
M_0	longitudinal magnetization of a sample when placed in a static magnetic field
ρ_0	spin density per unit volume
V	volume
$\vec{B}_{ext}$	external magnetic flux density
T_1	relaxation time constant describing spin-lattice interactions
T_2	relaxation time constant describing spin-spin interactions
T_2^*	relaxation time constant taking into account susceptibility losses
τ_{RF}	radio frequency pulse duration
α	flip angle
G	magnetic field gradient
ϕ	MR signal phase
k_x	k-space read direction sampling point
k_y	k-space phase encoding sampling point
$s(t)$	MR signal in time domain
$s(k)$	MR signal in frequency domain

TE	echo time
TR	repetition time
SE	spin echo
GE	gradient echo
B_{eff}	effective local static magnetic flux density
σ_s	shielding or screening constant
ξ	PRFS thermal coefficient
Z	impedance
L	inductance
C	capacitance
R	resistance
d	RF loop coil diameter
Q	Q-factor
X	reactance
$\langle \epsilon_n^2 \rangle$	time averaged Johnson-Nyquist noise
Δf	noise bandwidth
i	spectral noise current
λ	wavelength
v	phase velocity of a wave
ε_r	relative permittivity
μ_r	relative permeability
ε_0	vacuum permittivity
$\vec{E}$	electric field
σ	electric conductivity
P	electric power
m	mass
p	p-value for statistical significance testing
R_p	reduction factor for parallel imaging
$CEM_{43}°C$	cumulative equivalent number of minutes at 43°C
R_c	empirical factor to determine rate of cell death for the $CEM_{43}°C$

1. Introduction

The clinical value of regional radio frequency (RF) hyperthermia as a multimodal treatment strategy in conjunction with radiotherapy and chemotherapy has been demonstrated [1-8]. In current clinical RF hyperthermia practice, RF antenna arrays are used to focus specific absorption rate (SAR) hotspots on a targeted region in order to induce a desired temperature change [9]. Treatment planning, spatiotemporal monitoring of temperature and treatment efficacy is evaluated by means of magnetic resonance imaging (MRI) [10-12]. While characteristic RF transmission induced heating interventions are operated at frequencies of 70-100 MHz [9, 13], MR imaging at 1.5 T corresponds to ^{1}H nuclear magnetic resonance (NMR) frequency of 64 MHz. Notwithstanding the benefits of combining RF hyperthermia with the vast diagnostic capabilities of MRI, a separation of RF transmission for therapy and diagnosis has detrimental clinical implications. Extra hardware retrofitted into the MR suite – notably antennas, amplifiers and frequency filters – has the trait of limiting patient comfort, limiting ease of use, driving costs and potentially inducing imaging artifacts [14]. Another limitation is the RF frequency itself that is used for current MR guided RF hyperthermia therapies. The RF wavelength corresponding to 100 MHz is approximately 29 cm in tissue, which is relatively long compared to the geometry of a human torso, let alone the geometry of the human brain. As a consequence the selectivity of the effective treatment area and the spectrum of interventions [1] and therapies is restricted using MR guided RF hyperthermia. Here ultrahigh field (UHF) MR imaging with magnetic fields of $B_0 \geq 7.0$ T and associated ^{1}H proton excitation frequencies of $f > 298$ MHz offers an immense potential for a truly hybrid MR guided RF hyperthermia system. For targeted RF heating an effective wavelength of ~12 cm is reached, which is well below the size of the torso or the human brain. For diagnostic imaging pre- and post-treatment information may further benefit from the inherent signal to noise ratio (SNR) advantage of UHF MR [15, 16]. For MR thermometry (MRTh) enhanced spatial and temporal fidelity is to be expected at ultrahigh field strengths [17].

For all these reasons it is conceptually appealing to combine diagnosis, therapy and therapy monitoring in a single UHF MR system utilizing a single frequency for MRI and RF hyperthermia. To meet this goal, this work investigates the electrodynamic basis to combine effectively circular polarized magnetic fields needed for MRI and electric fields utilized for power absorption induced temperature increases. Such investigations expand to the concept of multi-channel RF transmission, which adds necessary degrees of freedom to change RF power and RF phase by individual channels. With this in mind novel RF antennas are simulated, designed, implemented, validated and their applicability is examined for human *in vivo* UHF MR imaging at 7.0 T. The lessons learned from these efforts are used to drive towards the design and implementation of a novel RF antenna configuration

and a multi-channel transmit applicator. This hybrid affords MRI and localized RF hyperthermia. Proof-o-principle is demonstrated at 7.0 T applying the proposed setup in phantoms mimicking the human head. In particular these studies show that our targeted and controlled RF heating setup can be integrated in a commercially available whole body 7.0 T MR research system expanding its scope from diagnostic imaging to therapeutic use. Based upon this breakthrough numerical electromagnetic field (EMF) simulations were carried to human *in vivo* models. The results obtained in this part of the project suggest that an RF hyperthermia application in the human brain is feasible with the proposed RF antenna design. To push the envelope further, theoretical considerations and first experimental results are extended to frequencies well above what is available today in MR research ($f > 1$ GHz). Regardless of increased power absorption levels at the surface with an increase in frequency, we could demonstrate that multi-channel transmit strategies can be employed to overcome some of these restrictions dictated by physics. These explorations are tailored to not only break ground for ^{1}H MRI at magnetic field strength significantly larger than 7.0 T (B_0=33.8 T), they can be translated to implications for *in vivo* electron paramagnetic resonance (EPR) suggesting that human *in vivo* EPR might be feasible in L-Band (1-2 GHz) or even above, which is unattainable so far [18]. While sufficient spin excitation is ensured, targeted RF hyperthermia selectivity benefits from reduced temperature hotspot sizes in higher frequency regions.

A truly hybrid RF hyperthermia system in synergy with UHF MR imaging has the potential for a vast clinical application repertoire ranging from RF hyperthermia applications in adjunctive cancer treatments, temperature enhanced diagnostic imaging to localized temperature triggered drug delivery systems. Our work could demonstrate for the first time that such a system is feasible and bears the potential to live up to its expectations.

2. Magnetic Resonance Imaging

Magnetic Resonance Imaging is an integral part of clinical diagnostics and has become the method of choice in imaging technology for a multitude of radiological examinations [19]. With an ever-growing number of clinical indications the clinical use of MRI continues to grow with its applications being not merely limited to anatomical and pathological imaging. Functional organ imaging, metabolic probing using *in vivo* MR spectroscopy, functional mapping of brain function, molecular imaging, interventional procedure monitoring and tissue characterization applications can be performed non-invasively and non-carcinogen since the underlying principles of MR are not based on ionizing radiation. This versatility of MRI provides physicists, engineers, clinicians, biologists, computer scientists and related disciplines sheer endless opportunities to drive innovations with the ultimate goal to improve medical healthcare.

The physics of MRI builds on the nuclear magnetic resonance phenomenon. The basics of NMR and MRI are introduced in this chapter, which builds on key textbooks [20-22].

2.1 Nuclear Magnetic Resonance

The underlying principle of MRI is the nuclear magnetic resonance effect, which enables the measurement of nuclear magnetic moments present in an external magnetic field by means of electromagnetic absorption and emission [23-25]. This enabled a powerful investigational method, since chemical compounds or molecular structures alter the electromagnetic environment of single nuclei, which can be detected by the changes in the emitted electromagnetic radiation. NMR spectroscopy is being used widely and has been an irreplaceable analytical tool in material science, chemistry or structural biology to study e.g. the structure and dynamics of proteins [26].

2.1.1 Discrete Angular Momentum

The basic concept of NMR can be derived from a single hydrogen atom. A ^{1}H atom consists of a hydrogen nucleus with one proton and with one unpaired electron “orbiting” the nucleus. Each proton, neutron and electron of such an atom possesses an angular momentum known as spin. A spin can be thought of as a circulating electric current, which has a magnetic moment, Equation (1). This magnetic moment $\vec{\mu}$ is directly proportional to the total angular momentum vector $\vec{J}$,

$$\vec{\mu} = \gamma \vec{J} \qquad (1)$$

with a proportionality constant γ called the gyromagnetic ratio. In general $\vec{J}$ combines contributions from orbital motion and from its intrinsic spin. For simplicity we neglect the orbital motion ($l = 0$) so that the total angular momentum quantum number equals the spin angular momentum ($j = s$). The total angular momentum is discrete based on the laws of quantum mechanics and can be expressed by multiples of a quantum angular momentum $\hbar$,

$$\mathrm{J}_z = m_j \frac{h}{2\pi} = m_j \hbar \tag{2}$$

with Planck's constant h and the magnetic quantum number m_j ,

$$m_j = -j, -j+1, \dots, j-1, j \tag{3}$$

with j being a positive integer or half-integer. The spin of an electron, proton and neutron is $s = \frac{1}{2}$ and following Equation (3) the discrete magnetic quantum number for these elements is $m_j = \pm\frac{1}{2}$. If an external static magnetic field ($\overrightarrow{H_0}$) is applied, the spins align either parallel ($+\frac{1}{2}$) or anti-parallel ($-\frac{1}{2}$) to the static magnetic flux density direction $\overrightarrow{B_0} = B_0 \cdot \overrightarrow{e_z}$, which leads to discrete energy values E,

$$\mathrm{E} = -\vec{\mu} \cdot \overrightarrow{B_0} = -\mu_z B_0 = -\gamma m_j \hbar B_0 \tag{4}$$

The two energy levels are shown in Figure 1 and depict an example of the general Zeeman effect, while the difference between these two energy states is proportional to the magnitude of the applied magnetic field.

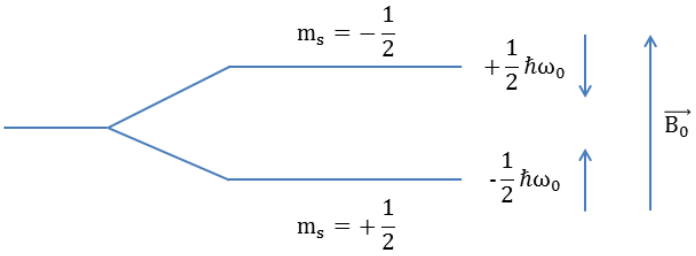

Figure 1: Two energy levels of the general Zeeman effect. At the lower energy state the spin is parallel to the external field $\overrightarrow{\mathbf{B_0}}$ [20].

For a constant B_0-field a transition between the higher (spins antiparallel) and the lower energy state (spins parallel) can be performed, by either absorption or emission of an energy quantum or photon of the value ΔE,

$$\Delta \mathrm{E} = \mathrm{E}\left(\mathrm{m_s} = -\frac{1}{2}\right) - E\left(m_s = +\frac{1}{2}\right) = \frac{1}{2}\gamma\hbar B_0 - (-\frac{1}{2}\gamma\hbar B_0) = \hbar\omega_0 \quad (5)$$

with ω_0 being the Larmor precession frequency following the relation

$$\omega_0 = \gamma B_0 \quad (6)$$

By applying an additional oscillating magnetic flux density $\overrightarrow{B_1}$ with the resonance frequency $f_0 = \frac{\omega_0}{2\pi}$ and a circular polarization in the plane perpendicular to the direction of $\vec{B}_0$

$$\vec{B}_1(t) = B_1(\overrightarrow{e_x}\cos\omega_0 t - \overrightarrow{e_y}\sin\omega_0 t) \quad (7)$$

a transition between the two energy states can be initiated. This is the basic underlying process for nuclear magnetic resonance or NMR applications. Table 1 shows the most important nuclides for NMR and MRI applications.

Nucleus	Spin	Magnetic moment in [μ_N]	$\gamma/2\pi$ in [MHz/T]
^1H	$^1/_2$	2.79	42.58
^2H	1	0.86	6.54
^{13}C	$^1/_2$	0.70	10.71
^{14}N	1	0.40	3.08
^{17}O	$^5/_2$	-1.89	-5.77
^{19}F	$^1/_2$	2.63	40.05
^{23}Na	$^3/_2$	2.22	11.26
^{31}P	$^1/_2$	1.13	17.24
^{43}Ca	$^7/_2$	-1.32	2.87

Table 1: List of selected nuclei with their nuclear spins, magnetic moment in units of the nuclear magneton and gyromagnetic ratios. A negative sign (magnetic moment, gyromagnetic ratio) refers to an anti-parallel alignment to the angular momentum vector [20].

On a nuclear scale with multiple particles present, NMR applications are restricted to nuclei of isotopes with a total angular momentum of $\vec{J} > 0$ (Equation (1)), which is based on the individual spin contributions of the protons and neutrons present. If an even number of protons and an even number of neutrons is present the total angular momentum vector sums up to $\vec{J} = 0$ and hence the nucleus can't be "excited" with an externally applied oscillating magnetic field $\vec{B}_1$. Nuclei of even mass number have integer spins and nuclei of odd mass number, like the hydrogen atom ^{1}H with one proton in the nucleus, have half-integer spins and can be used in NMR experiments.

What could be deduced for the total angular momentum of nucleons can be also applied to the electron. Paired electrons cancel out their magnetic moments. However for our ^{1}H example with one unpaired electron, the magnetic resonance phenomena can potentially be observed. The gyromagnetic ratio for an isolated electron is described by Equation (8),

$$\gamma_e = \frac{|-e|}{2m_e} g_e = \frac{g_e}{\hbar} \mu_B \tag{8}$$

with the elementary charge e, electron mass m_e, the electron g-factor $g_e \approx 2$ and the basic magnetic moment unit the Bohr magneton

$$\mu_B \equiv \frac{e\hbar}{2m_e} = 9.27 \times 10^{-24}\, J/T \tag{9}$$

In an equivalent fashion the gyromagnetic ratio for a free proton is

$$\gamma_p = \frac{e}{2m_p} g_p = \frac{g_p}{\hbar} \mu_N \tag{10}$$

with the proton mass m_p, proton g-factor $g_p = 5.59$ and the basic magnetic moment unit the nuclear magneton

$$\mu_N \equiv \frac{e\hbar}{2m_p} = 5.05 \times 10^{-27} J/T \tag{11}$$

For a free proton with half spin the magnetic moment is $\mu = 2.79 \cdot \mu_N$, which as well is the case for the ^{1}H nucleus. The Bohr magneton is an order of magnitude higher than the nuclear magneton primarily due to the mass difference between protons and electrons. The factor between both gyromagnetic ratios is hereby

$$\frac{|\gamma_e|}{\gamma_p} = 658 \tag{12}$$

which would imply that for electron excitation at a constant static magnetic field a frequency of 658 times the frequency of proton excitation needs to be applied. For a 1.5 T MR system with a proton resonance frequency of 64 MHz an electron resonance frequency of ~42GHz would be needed. In MRI nuclear spins are being used for imaging exploiting the NMR effect, whereas the electron magnetic resonance (EMR) effect is being used in electron paramagnetic resonance or electron spin resonance (ESR). In the following text only NMR and proton excitation is being examined. EPR and its application *in vivo* is being discussed in Chapter 6.2 together with some results obtained throughout this study.

2.1.2 Population of a System of Spins

On the macroscopic level ensembles of nuclei in molecular bonds rather than single atoms exist and need to be considered. When an external static magnetic field B_0 is applied, the spin system aligns itself parallel (N_+) or anti-parallel ($N\_$) to the direction of B_0. The probability to allocate one of these two states is described by their Boltzmann distributions,

$$\frac{N_+}{N_-} = \exp(\frac{\hbar\omega_0}{k_B T}) \tag{13}$$

with the kinetic energy $k_B T$ and the Boltzmann constant k_B. T is the temperature at which thermal exchange interactions takes place and lift the energy slightly above the lower energy state, the ground state (N_+). For a static magnetic flux density of B_0 = 1.0 Tesla the energy difference of the protons has a value of $\Delta E = 176\ neV$, whereas the thermal energy of protons at body temperature ($T = 310K$) exhibits a much greater value of $26\ meV$. With the assumption $k_B T \gg \hbar\omega_0$ a first order Taylor series approximation to the exponential function in Equation (13) can be performed

$$\exp\left(\frac{\hbar\omega_0}{k_B T}\right) \cong 1 + \frac{\hbar\omega_0}{k_B T} \tag{14}$$

and the spin excess (ΔN) can be summarized as

$$\Delta N \equiv N_+ - N_- \cong \frac{N}{2} \cdot \frac{\hbar\omega_0}{k_B T} \tag{15}$$

As can be seen in Equation (15) only a very small number of proton spins align with the magnetic field, due to the comparatively high thermal energy present. For 1.0 T at 310K the spin excess per total number of spins leads to a relatively small value of $\Delta N/N = 3.4 \cdot 10^{-6}$. However, Avogadro's constant, which is used to define the number of particles in one mol of a given substance, has a sufficiently large value of $N_A = 6.02 \cdot 10^{23} mol^{-1}$ for a longitudinal magnetization $M_z(t \to \infty) = M_0$ to be measured. For protons M_0 becomes

$$\mathrm{M}_0 \backsimeq \frac{1}{4}\rho_0 \frac{\gamma^2 \hbar^2}{k_B T} B_0 \tag{16}$$

with $\rho_0 = \frac{N}{V}$ being the density of the spins per unit volume V.

2.1.3 Relaxation and Bloch Equations

The magnetization M_0 was introduced as the equilibrium state ($t \to \infty$) of the more general term $\vec{M}(\vec{r}, t)$. Any perturbation of the equilibrium state will alter the magnetization vector and lead to relaxation processes towards the equilibrium state, which can be described mathematically and can be used to differentiate between different samples in NMR and MRI experiments. When an external magnetic field

$$\vec{B}_{ext} = \vec{B}_0 + \vec{B}_1\ (t) \tag{17}$$

is applied, the phenomenological description of these macroscopic relaxation processes can be described by the Bloch equation [24]

$$\frac{\mathrm{d}\vec{\mathrm{M}}}{dt} = \gamma \vec{M} \times \vec{B}_{ext} + \frac{1}{T_1}(M_0 - M_z)\vec{e_z} - \frac{1}{T_2}(M_x \vec{e_x} + M_y \vec{e_y}) \tag{18}$$

with the longitudinal relaxation time T_1 and the transversal relaxation time T_2. The cross product describes the torque of the interaction of the magnetic moment of the spin excess in the external magnetic field. For the three spatial components Equation (18) can be rewritten as

$$\frac{dM_x}{dt} = \gamma[M_y B_0 + M_z B_1 \sin \omega_0 t] - \frac{M_x}{T_2} \tag{19}$$

$$\frac{dM_y}{dt} = \gamma[M_z B_1 \cos \omega_0 t - M_x B_0] - \frac{M_y}{T_2} \tag{20}$$

$$\frac{dM_z}{dt} = \gamma\left[-M_x B_1 \sin\omega_0 t - M_y B_1 \cos\omega_0 t\right] + \frac{M_0 - M_z}{T_1} \tag{21}$$

If solely a static magnetic field is present ($B_1 = 0$) the solutions for the components of the magnetization vector are given by

$$M_{xy}(t) = M_{xy}(0)e^{-\frac{t}{T_2}}e^{-i(-\omega_0 t+\phi_0)} \tag{22}$$

$$M_z(t) = M_z(0)e^{-\frac{t}{T_1}} + M_0(1 - e^{-\frac{t}{T_1}}) \tag{23}$$

where ϕ_0 represents the M_{xy} magnetization phase at $t = 0$. Equation (22) and (23) present a clockwise rotation around the axis of the static magnetic field z, with the magnetization decaying exponentially both in xy-plane and in z-direction towards their steady state solutions $M_x(\infty) = M_y(\infty) = 0, M_z(\infty) = M_0$ as depicted in Figure 2.

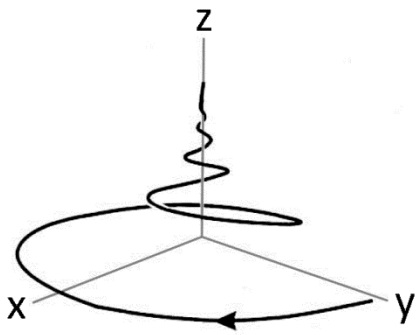

Figure 2: Time dependent decay of M_{xy} and M_z with the static magnetic field vector pointing in positive z-direction and the starting point position on the y-axis [20].

The decay rate is inverse proportional to the relaxation time constants T_1 and T_2. T_1 corresponds to the spin-lattice interaction, where spin transitions from the excited state N_- to the groundstate N_+ settle towards thermodynamic equilibrium as described by Equation (15). T_2 is considered as the spin-spin interaction, which represents a loss of phase coherence due to local field changes in the presence of neighboring spins leading to local differences in their precession frequencies. A third relaxation constant may be introduced, namely the effective relaxation time T_2^* which is defined as

$$\frac{1}{T_2^*} = \frac{1}{T_2} + \frac{1}{T_2'} \tag{24}$$

with T_2' representing a decay in magnetization due to field inhomogeneities, e.g. magnetic susceptibility differences between different tissue types. In general the three relaxation constants follow the relation $T_2^* < T_2 < T_1$.

Assuming that the steady state solution of Equation (22) and Equation (23) is present, by applying a short RF pulse with duration τ_{RF} ($\tau_{RF} \ll T_1, T_2$) a spin excitation field $\vec{B}_1(t)$ can be induced that causes a precession about B_1, as shown in Figure 3.

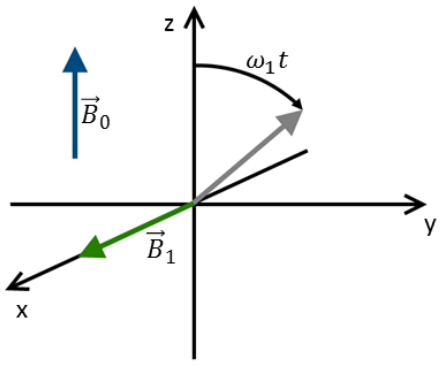

Figure 3: Nuclear spin magnetization vector after the application of an external magnetic field perpendicular to the static magnetic field [22].

Then the magnetization vector can be described as

$$M_x = M_0 \sin \omega_1 t \sin \omega_0 t \tag{25}$$

$$M_y = M_0 \sin \omega_1 t \cos \omega_0 t \tag{26}$$

$$M_z = M_0 \cos \omega_1 t \tag{27}$$

with $\omega_1 = \gamma B_1$. Equation (25)-(27) demonstrate that the tilting angle $\Delta\alpha = \omega_1 t$, the so-called flip angle (α), depends on the amplitude of the applied RF-pulse and its duration with α being given by:

$$\alpha = \gamma \int_0^{\tau_{RF}} B_1(t')dt' \tag{28}$$

2.2 From NMR to MRI

Magnetic Resonance Imaging was born by superimposing spatially varying magnetic field gradients to the main static magnetic field [27-29]. This concepts invokes spatial Larmor frequency variations

along the magnetic field gradient direction (Equation (6)), which provide means for spatial encoding in three dimensions and pose the basis of modern MRI. To understand a simple 2D imaging experiment, slice selection together with a gradient echo and a spin echo imaging technique are introduced, which form the basis for many MRI applications.

2.2.1 Spatial Encoding and the k-Space

To acquire spatial information, which can be translated into an image, magnetic field gradients in the scale of $[mT]$ are superimposed to the static magnetic flux density, which is usually found in the order of $[T]$. Assuming that the magnetization has been tipped by an RF pulse at $t = 0$ in the transverse plane, placing a gradient $G(t)$ along the x-axis results in

$$B_x(x,t) = B_0 + xG(t) \tag{29}$$

which deviates the angular frequency from the Larmor frequency by

$$\omega_G(x,t) = \gamma x G(t) \tag{30}$$

along the x-direction. The MR signal $s(t)$

$$s(t) = \int \rho(x) e^{i\phi_G(x,t)} dx \tag{31}$$

consequently accumulates phase $\phi_G(x,t)$

$$\phi_G(x,t) = -\gamma x \int_0^t G(t')dt' \tag{32}$$

depending on the gradient strength, time and location of the signal along the gradient direction. After defining a spatial frequency $k = k(t)$

$$k(t) = \frac{\gamma}{2\pi} \int_0^t G(t')\, dt' \tag{33}$$

Equation (33) may be rewritten to

$$\mathrm{s}(k) = \int \rho(x) e^{-i2\pi kx} \mathrm{dx} \tag{34}$$

which represents the Fourier transform of the spin density of the sample. In this way the spin density by the sample was Fourier or frequency encoded along the direction of a linear gradient and the inverse Fourier transform can retrieve the spatial dependent spin density of the sample. The data space which accommodates spatial frequencies k is called k-space and the x-axis along which data sampling points are acquired is the read axis or frequency encoding axis. To add a second dimension in order to create a 2D image another gradient G_y to encode spatial information along the y-axis is needed. Since data sampling by means of Equation (34) is limited to a single dimension, the second gradient needs to be incremented to get 2D spatial frequency information, which is referred to as phase encoding. Figure 4 shows the k-space together with the sampling points in k_x and k_z direction for a Cartesian sampling scheme, which is commonly used in MRI.

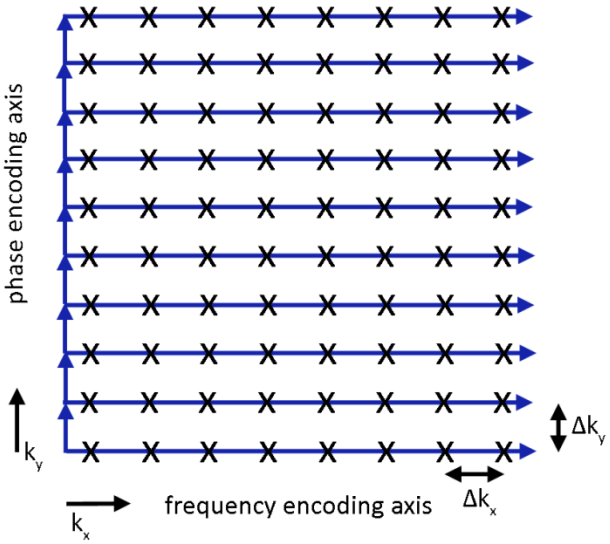

Figure 4: k-space sampling points (dots) and k-space sampling direction (lines) in k_x and k_y direction for a Cartesian sampling scheme. The resolution is depicted by Δk_x and Δk_y [20].

This principle of incrementing a gradient in phase encoding direction can be extended to 3D imaging by just adding a second phase encoding direction perpendicular to the first phase encoding gradient to cover a 3D k-space. There are numerous arbitrary and regular ways of sampling k-space and generating contrasts in MRI. A complete presentation of sampling schemes is out of scope for this work and can be found in detail in the literature [19-22].

2.2.2 Slice Selection for 2D Imaging

To choose a selected region for MRI, we can restrict our spin excitation to 2D slices. To do so, slice selective gradients are applied together with an amplitude and phase modulated RF B_1 pulse with a given bandwidth as illustrated in Figure 5.

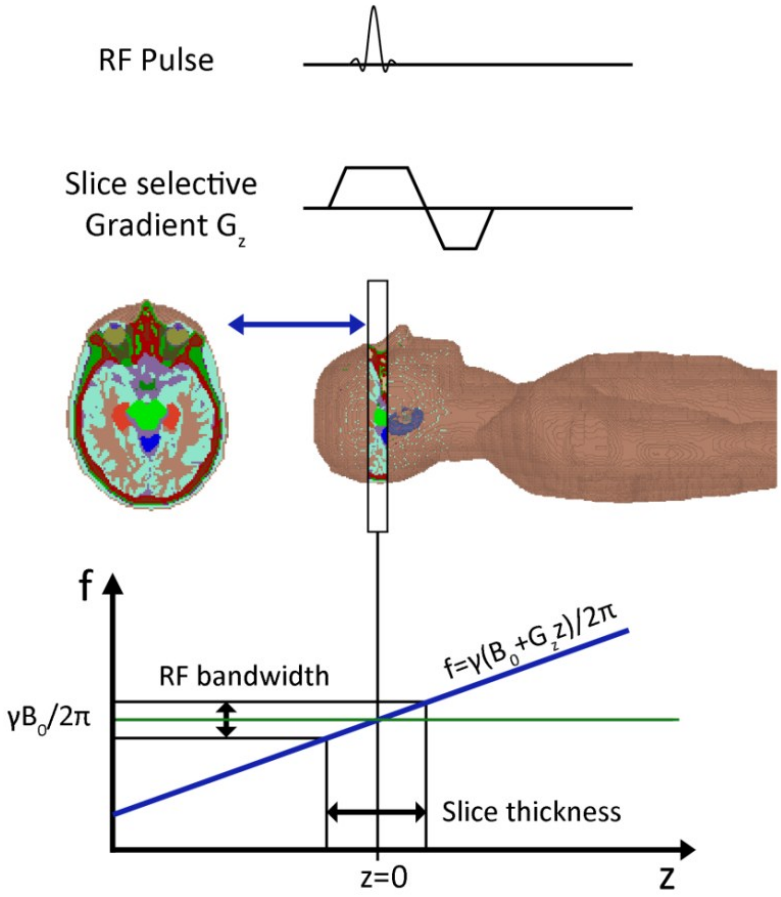

Figure 5: (a) Slice selection gradient G_z applied during B_1 spin excitation using an amplitude modulated RF pulse with a given bandwidth. (b) Only spins are excited in a slice through the object, where the Larmor frequency matches the RF pulse frequency. (c) The resulting slice thickness and position can be determined by the RF pulse center frequency and any offset to the center frequency, the RF pulse bandwidth as well as the gradient amplitude [20].

When a gradient G_z is switched on along the z-axis, the Larmor frequency along z deviates from the center frequency $\gamma B_0/2\pi$. An RF pulse with the Larmor frequency will therefore only excite spins around the Larmor frequency depending on the bandwidth of the RF pulse. The thickness of the excited slice depends on the gradient strength and the RF bandwidth (Figure 5) and can be determined by the following relation:

$$Slice\ Thickness = \frac{Bandwidth_{RF}}{G_z\gamma/2\pi} \tag{35}$$

Extending the concept of slice selective gradients during RF excitation to of G_x, G_y and G_z, arbitrary 2D slice orientations can be chosen for imaging. The gradient with polarity opposite to the slice selection gradient, as shown in Figure 5, is applied to rephase and balance out dephasing that was induced by the slice selection gradient.

2.2.3 Fundamental Imaging Techniques – Gradient Echo and Spin Echo

After an initial application of an RF pulse ($\overrightarrow{B_1}(t)$) to tip the nuclear magnetization vector in the x-y plane a free induction decay (FID) signal is observable at the receiver as exemplified with a 90° RF pulse in Figure 6.

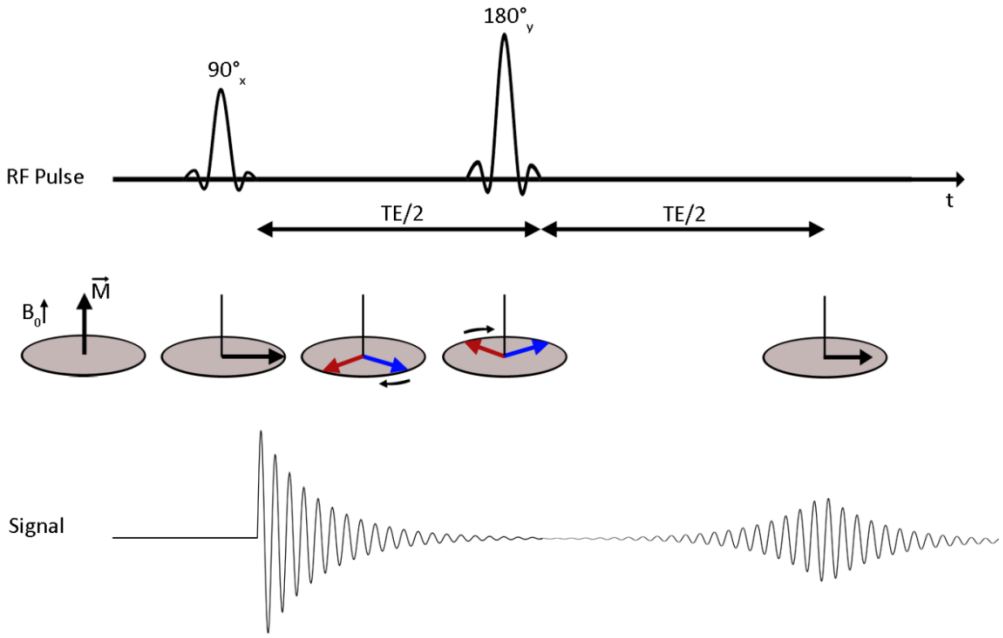

Figure 6: Schematic description of a spin echo technique using a 90° RF pulse followed by a 180° RF pulse. The initial signal decay of the FID signal after 90° RF pulse application decays with T_2 or T_2^*, while the spin echo refocused magnetization amplitude decays with T_1.

The signal decays with T_2 or T_2^*, due to decoherence of individual spins which result in slight angular frequency differences as illustrated in Figure 6. The FID signal can potentially be used for MRI, however it is challenging due to relatively short relaxation times. Readout and slice selective gradients need to be applied and a simultaneous reception while applying RF transmission pulses could introduce unwanted noise contributions or saturate the receiver [30]. A way to overcome this is the use of so-called spin echoes (SE), which enable a flexible way to gather measurement data at defined time points after the initial RF pulse application [30]. If a second 180° RF-pulse is being transmitted at TE/2, the transverse spin magnetization vectors are being rotated in space, so that the slower angular frequency components meet with the faster contributions at the echo time (TE) to form a spin echo, as depicted in Figure 6. This signal, whose amplitude decays with T_1 with respect to the initial amplitude, can now be readout with appropriate gradient modulation and sampled to fill the k-space. A similar principle is used with the so-called gradient echo (GE) technique. Here instead of a second RF pulse, gradients are being used to refocus the magnetization as shown in Figure 7.

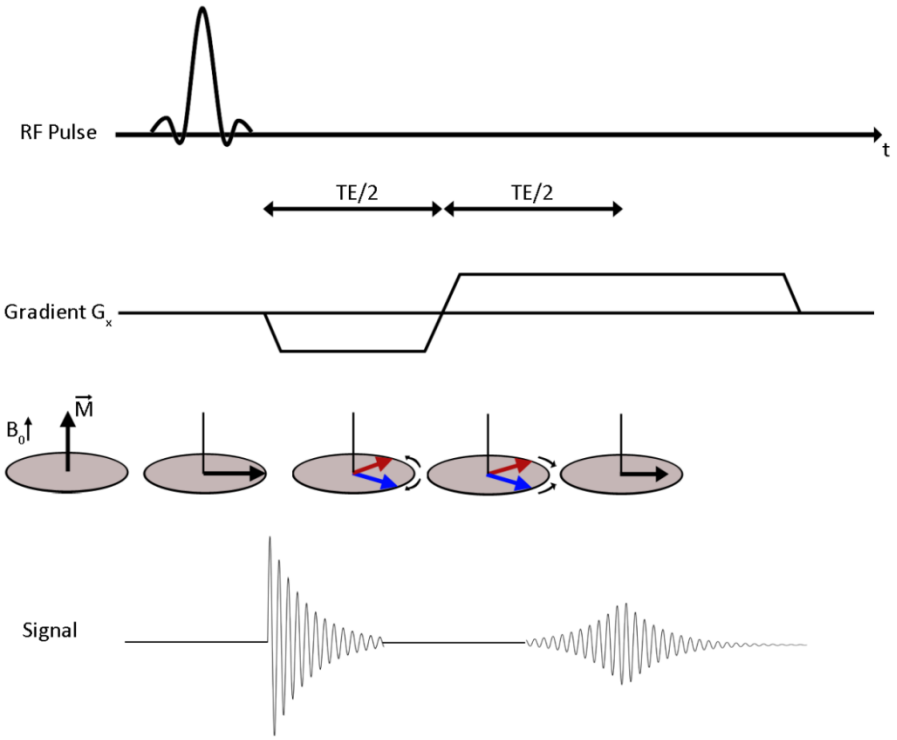

Figure 7: Schematic description of a gradient echo technique using a 90° RF pulse followed by a gradient in frequency encoding direction. The initial signal decay of the FID signal after 90° RF pulse application is additionally decreased by the played out gradient, which changes the precession frequency of the spins slightly. This dephasing is reversed by changing the polarization direction of the gradient, to form a spin echo at TE. The gradient echo refocused magnetization amplitude decays hereby with T_2^*.

The gradients are applied along frequency encoding direction (x-direction) directly after the RF pulse, when the magnetization is found along the x-axis. The additional gradients cause the nuclear spin magnetic moments to dephase faster than the usual T_2 relaxation. Switching the gradient polarity while maintaining its amplitude, reverses the dephasing process and refocuses the magnetization at TE to form a gradient echo. Since dephasing is enforced by the gradients and not by naturally occurring T_2 decaying times, the echo times can be chosen very short in comparison to the spin echo. The amplitude decay of the GE as compared to the FID follows hereby T_2^* decaying times, since these components are not refocused like in the spin echo approach.

2.3 MR Thermometry

A major advantage of MRI is its versatility in deriving non-invasively multiple information from the human body next to classical anatomical imaging. One such parameter is an indirect measurement of the temperature, which is a variable in many MR equations. E.g. the equilibrium magnetization introduced in Equation (16) already shows a proportionality of $1/T$ known as the Curie law.

Consequently it is apparent that it is possible to determine temperature changes based on proton density weighted images, as the proton density itself is unaffected by temperature changes. Other ways to acquire temperature information is due to the temperature dependences of T_1 and T_2 relaxation times of water protons, of the diffusion coefficient in diffusion weighted imaging, of magnetization transfer (MT) exchange rates in MT techniques and of a proton resonance frequency shift (PRFS) [17, 31, 32]. Especially the PRFS method has some advantageous features for *in vivo* applications and will be described in more detail throughout this chapter since it is being used in the experiments.

The resonant frequency of a free proton is slightly different from the resonance frequency of a proton in a molecular bond, which is referred to as chemical shift. This effect is due to slight local changes of B_0 at the position of the nucleus, which depends on the given molecular structure. The total effective field B_{eff} may be described as

$$B_{eff} = B_0(1 - \sigma_s) \tag{36}$$

where σ_s is the shielding or screening constant and represents small secondary field contributions generated by the electrons e.g. of the water (H_20) molecule. Consequently the resonant frequency change can be expressed as

$$\omega = \gamma B_0(1 - \sigma_s) \tag{37}$$

Hydrogen bonds of many neighboring H_20 molecules reduce the electronic shielding by distorting the electronic configuration, which otherwise is predominantly shielded by the electron cloud. Such characteristics are being utilized in NMR spectroscopy to characterize the structure of e.g. proteins. With an increase in temperature these hydrogen bonds loose stability and break, which increases the shielding constant and lowers the proton resonance frequency. The electron-screening constant varies linearly with temperature in our temperature range of interest:

$$\sigma_s(T) = \xi T \tag{38}$$

with the PRFS thermal coefficient ξ, which for H_20 has a value of $-1.02 \pm 0.02 \cdot 10^{-8}/K$ [33]. These local static magnetic field changes induced by temperature can be measured by e.g. the phase information of the previously introduced gradient echo imaging technique [34] as illustrated in Figure 8.

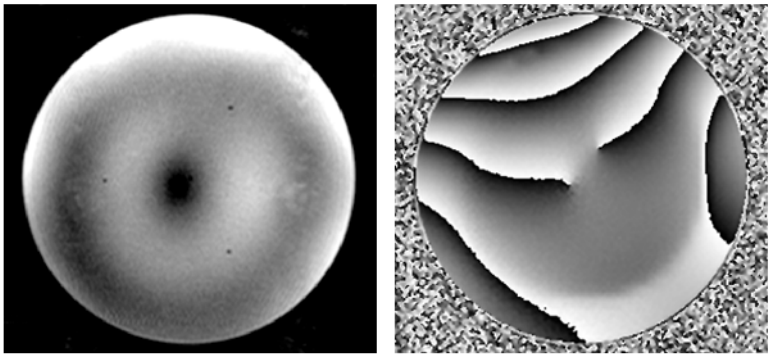

Figure 8: Magnitude (left) and phase (right) images of a phantom surrounded by eight MR antennas. The inhomogeneous phase distribution is due to B_0 field inhomogeneities. The number of phase wraps in the phantom is determined by the phase evolution during the echo time TE. Please note that the two singularities visible in the phase image are reconstruction errors due to low MR signal contributions.

The phase map presented in Figure 8 shows B_0 field inhomogeneities due to imperfect MR magnet construction implying that the phantom itself is free from susceptibility gradients. In an ideal case all phase contributions should display an equal value. Nevertheless a relative phase change due to temperature changes can be deduced which can be converted to a relative temperature map by the following equation:

$$\Delta T = \frac{\phi(\mathrm{T}, \vec{\mathrm{r}}) - \phi(\mathrm{T}_0, \vec{\mathrm{r}}\,)}{\gamma \xi B_0 TE} \tag{39}$$

with the phase information $\phi(T_0, \vec{\mathrm{r}})$ of the reference image prior to the temperature change and $\phi(T, \vec{\mathrm{r}})$ after the temperature change. A few corrections need to be considered in an experimental measurement setup. Superconducting magnets that generate the B_0 field exhibit field drifts over time [35] which for our 7.0 T MR system (Magnetom, Siemens Healthcare, Erlangen, Germany) is in the range of 0.02 ppm/h. This field drift alone would account for a temperature error of ~2°C in a single hour. One way to correct for such error is the use of external lipid reference probes such as oil [36]. Lipid resonance frequencies show almost no temperature dependent shift, making them ideal candidates to record and subtract the field drift of the scanner during MR thermometry (MRTh) experiments. Another source of error is a temperature dependent change in electrical conductivity which affects the PRFS thermal coefficient [37]. This effect is independent of TE and can be corrected with the so-called double-echo PRFS-method, where two echo times are acquired and subtracted [37-39]. Applying these measures the final temperature correction term is:

$$\Delta T_{corr} = \frac{(\Delta\phi_{\mathrm{H_2O}}(TE_2) - \Delta\phi_{\mathrm{H_2O}}(\mathrm{TE}_1)) - (\Delta\phi_{oil}(TE_2) - \Delta\phi_{oil}(TE_1))}{\gamma \xi B_0 (TE_2 - TE_1)} \tag{40}$$

An example of the phase change at a constant TE due to a temperature increase in a homogeneous phantom is displayed in Figure 9.

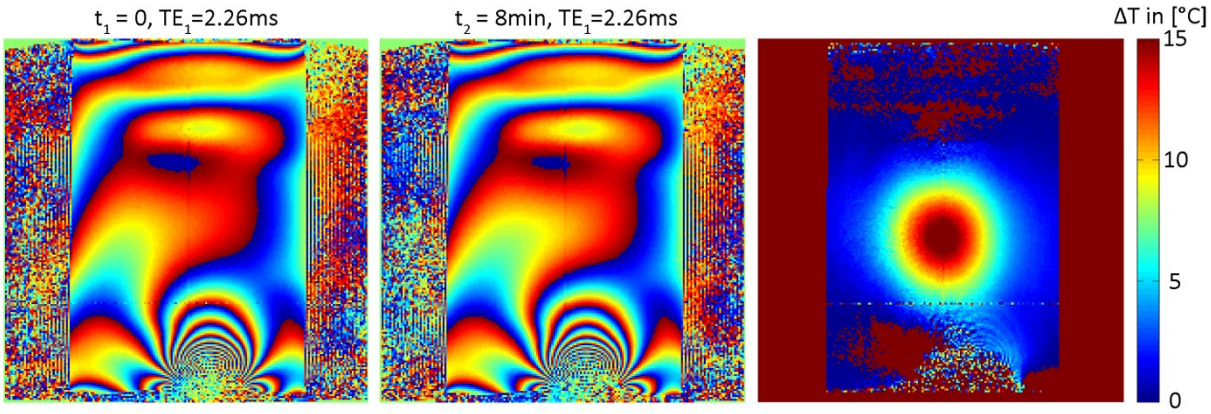

Figure 9: Phase map of a GRE imaging technique prior to RF heating experiments (left) and after 8 minutes of RF heating (middle). Resulting temperature map (right) acquired with the double-echo PRFS method (TE_1 = 2.26 ms, TE_2 = 6.34 ms) at 7.0 T.

3. MR Systems Hardware

To enable the complex process of MR imaging, the interplay of multiple hardware components demanding high performance criteria is needed to transform physical theory to experimental practice. The static B_0 field is achieved by using windings of low temperature superconductors cooled off with liquid helium to temperatures below 4 K. Passive iron shims and active shim coils correct for remaining B_0 field inhomogeneities. For spatial encoding gradient fields $\vec{G}(t)$ in the range of mT/m are switched at kHz frequencies using coil windings driven by high power amplifiers allowing for high peak and root mean square (rms) current output. Finally radiofrequency coils are used to generate the circularly polarized magnetic flux density B_1^+ (the + indicates hereby the positive circularly polarized field rotating in direction of the Larmor precession of the spins [40]) for spin excitation. Pulsed high peak power RF power amplifiers (RFPA) are driving these RF coils in the MHz range. RF coil development in particular is of high importance to achieve high SNR levels that can be exploited by MR imaging techniques for clinical applications. This chapter introduces fundamentals of RF coils, the challenges of RF coil development, the basics of RF coil characterization together with the fundamentals of RF components incorporated in the RF chain that connects the coil with the RF transmitter or RF receiver.

3.1 Fundamentals of RF Coils

RF coils and RF coil development can be thematically separated in transmission and reception characteristics. In current clinical practice at 1.5 T and 3.0 T birdcage volume resonators are commonly used for transmission to excite the nuclei of interest [41, 42]. The practical advantage of a volume resonator is its capability of uniform spin excitation over a large field of view (FOV). For signal reception surface RF coils placed in close proximity to the object are commonly used because of the filling factor and SNR advantage over using large volume resonators for reception [43]. Further SNR benefits can be achieved by expanding a single element surface RF coil to a multi-element RF coil array [44]. The geometric splitting of the MR sensitivity profiles of these RF coil arrays furthermore enabled the use of parallel imaging techniques to significantly reduce MR acquisition times [45, 46].

3.1.1 Matching and Tuning

An RF coil, as illustrated in Figure 10a, is a resonant circuit consisting of complex impedances of frequency dependent inductors and capacitors. Whereas an inductive impedance Z_L

$$Z_L = j\omega L \tag{41}$$

with an inductance L (depending on the conductor diameter, length and material) acts as a low-pass filter, a capacitive impedance Z_C

$$Z_C = \frac{1}{j\omega C} \tag{42}$$

with the capacitance C, presents a high-pass filter. Combining both yields a resonance at a specific frequency or a band-pass filter, which can be used to transmit the energy needed for MRI. Setting the frequency to our desired target frequency is referred to as *tuning*. For an efficient energy transmission, with low reflection losses, the target impedance should match the cable impedance (usually 50 Ω). This process is called *matching* and refers to the adjustment of the real impedance to the cable impedance, which is connected to a transmitter (RFPA) or to a receiver (preamplifier and analog-to-digital converter (ADC)). The challenges of RF coil design arise from the non-trivial interaction between the RF coil resonant circuit and the object to be imaged. Due to heterogeneous electromagnetic tissue properties and the near-field regime – distance between the RF coil and the human body smaller than the RF wavelength – parasitic capacitances arise, which alter the electromagnetic structure of the resonant circuit and may influence both the tuning and matching conditions. To correct for these unwanted power/signal losses, so-called matching circuits are applied using ideally lossless reactive components such as variable capacitances. An example of a matching circuit is depicted in Figure 10b.

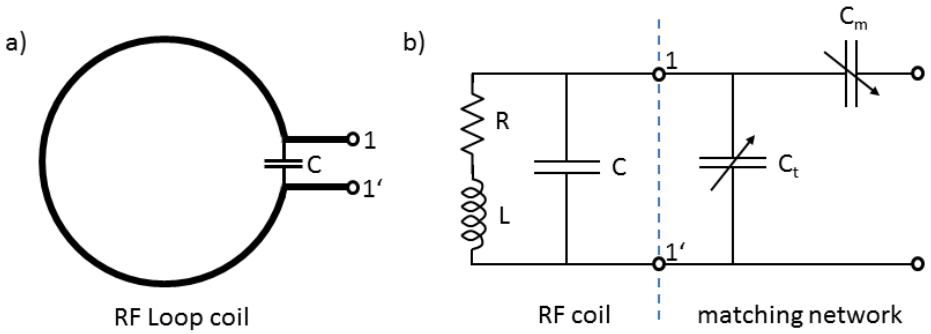

Figure 10: (a) Schematic of a simplified RF loop coil and (b) its electric circuit representation with resistive losses R, RF coil inductance L, capacitance C connected to a matching network with variable capacitors $\mathbf{C_t}$ and $\mathbf{C_m}$.

The solutions of this simple circuit in terms of input impedance with $C_t' = C + C_t$ as seen by the amplifier is

$$\mathrm{Z} = \frac{1}{j\omega C_m} + \frac{\left(\frac{1}{j\omega C_t{}'}\right) \cdot (R + j\omega L)}{R + j\omega L + \frac{1}{j\omega C_t{}'}} \tag{43}$$

with C_t being a variable tuning capacitor and C_m a variable matching capacitor. Rearranging equation (43) in real and imaginary part, leads to

$$\mathrm{Z} = \frac{R \cdot \left(\frac{1}{\omega C_t{}'}\right)^2}{R^2 + (\omega L - \frac{1}{\omega C_t{}'})^2} - j\frac{1}{\omega C_t{}'} \cdot \left(\frac{R^2 + (\omega L)^2 - \frac{L}{C_t{}'}}{R^2 + (\omega L - \frac{1}{\omega C_t{}'})^2} + \frac{C_t{}'}{C_m} \right) \tag{44}$$

The goal for maximal power transfer ($Re\{Z\} = 50\Omega$ and $Im\{Z\} = 0$) can now be reached by varying C_t and C_m in Equation (44) under the condition that the value of C is chosen in a reasonable range to compensate for inductance (L) contributions from the loop.

3.1.2 Receive only Phased Arrays

Ideal current pattern calculations at B_0 = 1.5 T suggest that circulating circular current pattern form around the imaging object, which would yield ultimate intrinsic SNR [47, 48]. To resemble such patterns either RF loop coils, as schematically presented in Figure 10a, or quadrature surface RF coils can be utilized [48, 49]. RF Loop coils are predominantly used as receive elements for $B_0 \leq 3.0$ T, whereby the loop diameter d determines the location p with the maximum achievable SNR for the given loop configuration at the point $p = d$ [44]. However since the loop diameter cannot be varied in practice, a single surface RF loop coil element is only capable to cover a limited region of the volume with the optimal SNR at position p and a decrease towards the depth of the volume. To increase total SNR even further, the addition of a second or multiple circular surface elements can be used to combine the individual RF coil sensitivity profiles, improve the “vision” of the RF coil to the total dimensions of the combined phased array and eventually resemble the ideal current paths dictated by ultimate SNR considerations [44, 48]. To reach higher SNR at surface regions (p < d), the only way to increase SNR is the use of smaller diameters for the RF coil elements [44].

Notwithstanding the SNR advantage of multi-element RF coil arrays, for a practical implementation certain design criteria need to be considered. When placing two or more resonant loops in close proximity to each other, mutual coupling between the RF coils might occur, which may shift the resonance frequency f_0 of each individual RF coil. To counteract coupling phenomena and coupling induced SNR reduction, various decoupling strategies were proposed. This includes overlapping RF coil areas [44], using external circuits [50], shared capacitors [51] or low input impedance

preamplifiers [44]. By applying these techniques, NMR phased arrays can be successfully implemented with SNR increases of 87% while moving from a single channel RX RF coil to a 16-channel RX RF coil array [52], by up to 204% using a 32-channel array as compared to an 8-channel RF coil [53, 54] or even 220% with a 128-channel receive RF coil array as compared to a 24-channel RF coil [55].

3.2 RF Coil Characterization

Characterizing RF coil performance is not a straightforward task. Depending on the application SNR is not the single most important parameter to investigate. In this chapter RF coil characterization for receive arrays is presented, whereas chapter 4 introduces considerations for transmit RF coils tailored for UHF-MR.

3.2.1 Q-Factor

The Q-Factor is a measure of the damping of the resonant circuit and indicates the rate of energy loss in relation to the stored energy in the circuit. It can be calculated for each component, which is being introduced into an electric circuit and offers an indication how much loss has been inserted (insertion loss) into the circuit.

$$Q = \frac{X}{R} \tag{45}$$

With X representing the reactance of the component (inductance or capacitance) and R its resistance. For a parallel resonant circuit as represented by a RF loop coil in air, the unloaded q-factor can be described as:

$$Q = \sqrt{\frac{L}{C}}\frac{1}{R} \tag{46}$$

The quality factor is inverse proportional to the resistive losses in the RF coil as can be seen in Equation (46), concluding that a lower resistance increases Q. High Q-factors are important for the components used in RF coil design as the voltage generated by the magnetization flux variation in the receiving RF coil is multiplied by almost Q to measure the final voltage at the input port. However the Q-factor impacts both signal and noise voltages from the sample and hence does not influence SNR [56]. Being a measure of insertion losses, the Q-factor is also used to measure an increase in losses

once the imaging sample is brought in close proximity to the RF coil. In this condition, parasitic capacitances are being formed between the RF coil and the imaging object, which usually possess very low Q-factors. This can be expressed by the ratio of unloaded (no sample) to loaded (with sample) Q-factor and indicates if the sample or the RF coil is predominantly responsible for RF losses. Bigger RF coil diameters will increase the ratio of $Q_{unloaded}/Q_{loaded}$ as depicted in Figure 11 and shown in [57]. Consequently the losses introduced by the sample using small RF coil diameters are low making the electric losses of the RF coil the dominant source.

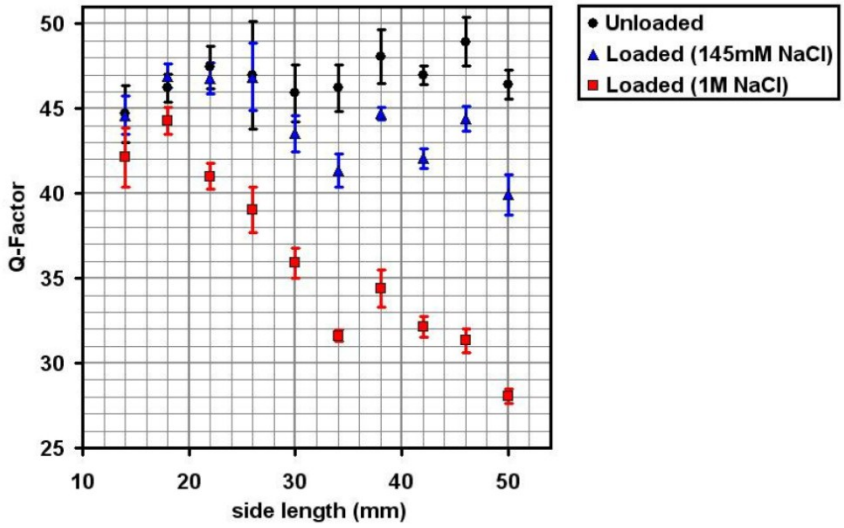

Figure 11: Measured unloaded and loaded Q-factors of rectangular RF loop coils as a function of the side length of the loop and loading of the RF coils (reprinted with permission from author [58]).

3.2.2 Noise Correlation

Noise is based on thermally driven Brownian motion of electrons within a conducting sample [59], e.g. the patient or as electric circuit noise within any RF components such as the MR RF coil itself [56, 60, 61]. The electrons travel random RF currents in a number of eddy current loops, thus randomly varying the EMF, which eventually induce a voltage in the receiving RF coil. In the given frequency range this noise, which increases with f_0, is predominantly coming from the patient for high Q-factor RF coils. In the presence of multiple receiver elements, even if the receiver elements are fairly well decoupled and no mutual inductance or net flux is present, the random thermal motion in the sample will produce correlated noise in both elements. This has implications both on SNR and parallel imaging performance [44, 62, 63]. The noise in a single RF coil due to Brownian motion or Johnson-Nyquist noise is given by:

$$\langle \epsilon_n^2 \rangle = 4k_B T \Delta f R \tag{47}$$

With Δf the noise bandwidth, k_B the Boltzmann constant in joules per kelvin, T absolute temperature of the resistor, R resistor value of the sample, the <> brackets indicate a time average [62]. The integration over the sample volume yields the mean square noise current

$$\langle i_1^2 \rangle = 4kT\Delta f \iiint \rho_r (\sum_i |a_{1i}|^2)\, dx\, dy\, dz \tag{48}$$

with ρ_r the electric isotropic resistivity and i a summation over x, y, z [62]. a_{1i} is a complex constant which takes into account RF coil and sample parameters. Introducing a second RF coil, the correlated sample noise currents in each RF coil are

$$\langle i_{1s} i_{2s} \rangle = 4kT\Delta f \iiint \rho_r (\sum_i |a_{1i}||a_{2i}| \cos(\phi_{1i} - \phi_{2i}))\, dx\, dy\, dz \tag{49}$$

with the phase contributions ϕ_{1i}, ϕ_{2i}. The spectral noise correlation by the noise from the RF coil elements and the sample at a single frequency can be described as the real part of the inverse impedance matrix Z_T

$$\langle i_1 i_2 \rangle = 4k_B T Re\left({}^{1}/_{Z_T}\right) \tag{50}$$

with the spectral noise currents i_1, i_2 [62, 63]. This formulation of noise is most relevant for MRI experiments since it is limited to the data sampling bandwidth of the MR scanner, which in most cases is narrower than the RF coil bandwidth [63]. Consequently for multi-channel arrays a noise correlation matrix including all channels can be measured using a network analyzer or by noise scans (no RF power applied) as shown exemplified for an 8-channel RF coil in Figure 12.

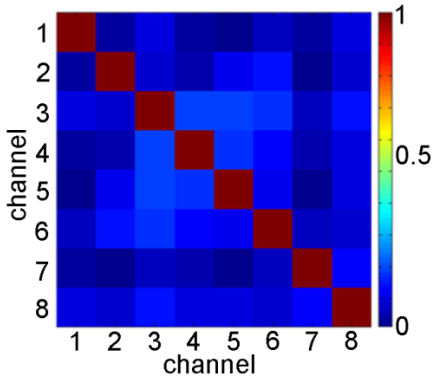

Figure 12: Calculated noise correlation matrix of an 8-channel transmit/receive array for UHF MR head imaging. Noise was acquired *in vivo* by means of noise pre-scans [64, 65].

3.2.3 Signal to Noise Ratio (SNR) Measurements

Signal to noise ratio is one of the most important parameters to determine MR image quality. SNR dependents on the hardware used but also on the imaging parameters, spin densities from image anatomy and physiology and can be used to provide insights into the performance of a RF coil array. The most straightforward technique to determine SNR is by performing a statistical analysis of a region of interest (ROI) within the tissue of interest and a ROI outside of the imaging object representing the noise distribution. However, for multichannel receive RF coil arrays and parallel imaging techniques noise may not be spatially uniform and its statistical noise distribution may be unknown. The ROI approach for SNR determination could lead to inaccurate results and needs to be replaced when using multichannel arrays [66].

Throughout this work a full reconstruction in SNR units is being used as proposed and implemented by Peter Kellman [64, 67]. This method operates on per pixel basis and is compatible with parallel imaging as well as various element combining methods like root-sum-of-squares magnitude combining or B_1^+ weighted combining [44]. Prior to each scan, noise statistics are being estimated by calculating the noise covariance matrix using pre-scan (no RF power applied) noise data samples from all individual RF coil elements [63, 64, 67]. The pre-scan noise measurements are performed *in vivo* to include noise dependency on RF coil loading for the final SNR reconstruction. In the next stage, as illustrated in Figure 13, the standard imaging sequence is played out following an image reconstruction of both the signal and noise combined and the noise only data [64, 67].

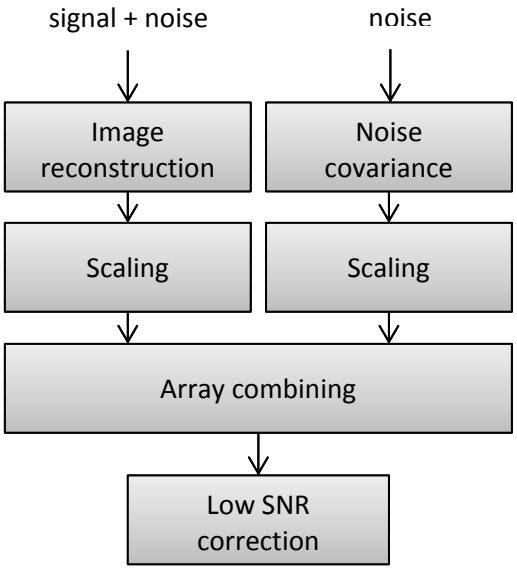

Figure 13: Schematic view of the generation of SNR maps based on [64, 67].

Each post-processing step such as fast Fourier transform (FFT) scaling, interpolation, windowing, zero-filling etc. may potentially change the noise standard deviation output versus its input and needs to be considered. To account for system specific noise dictated by the receiver bandwidth, a calibration measurement of the power spectrum is performed to determine the scaling factors [64, 67]. In the final stage, array combining is performed to create the final SNR maps. For low SNR an additional correction step is executed accounting for the number of receive channels in operation [64, 67]. For SNR assessment of parallel imaging data spatially dependent noise amplifications need to be accounted for due to the ill-conditioning of the image reconstruction process. Here the scaled noise is utilized in complex RF coil sensitivity maps to combine the images using image domain based or k-space domain based reconstruction techniques [45, 68, 69].

3.2.4 Parallel Imaging and the G-Factor

One of the most important MR techniques developed in recent years is parallel imaging which supports k-space undersampling and hence enables a significant acceleration of image acquisition. For this purpose parallel imaging techniques use RF coil sensitivity information of multi-channel receive RF coil arrays. With dedicated RF coil implementations acceleration factors of up to 12-16 were reported to be feasible for *in vivo* studies [54, 55, 70-73]. Reconstruction and unfolding of undersampled k-space data comprises two categories: image space and k-space based techniques [45, 46, 68]. A more detailed overview of the reconstruction algorithms can be found in [74].

All parallel imaging reconstruction techniques require an accurate knowledge of the individual RF coil element sensitivities of a RF coil array. This information is usually derived from a fully sampled, low-resolution reference scan. Positioning of the RF coil elements and the resulting RF coil sensitivity profiles in phase encoding direction are highly important as the reduction is performed along this dimension. In other terms, an RF coil array can be designed specifically to allow high acceleration factors with its RF coil sensitivity profiles spatially distributed along the imaging direction [58, 75, 76]. To evaluate the RF coil efficiency in terms of parallel imaging performance the geometry factor (g-factor) [46] is used :

$$g = \frac{SNR_{optimal,unaccelerated}}{SNR_{accelerated} \cdot \sqrt{R_p}} = \frac{SD_{accelerated}}{SD_{optimal,unaccelerated} \cdot \sqrt{R_p}} \tag{51}$$

with R_p being the reduction factor and SD the standard deviation. The optimal SNR can be calculated by taking into account the noise correlation matrix between elements and by using proper noise scaling as previously described.

3.3 Radio Frequency Chain

Apart from the RF coil itself, other RF components and hardware components are of relevancefor RF coil design and need to be considered. In Figure 14 a schematic view of the functionality of an MRI system is presented. The operator defines the imaging parameters which are being translated into gradient and pulse waveform by a waveform generator. The digital signal waveforms are being transformed by a digital-to-analog converter (DAC) before being amplified by either the gradient amplifier or the RF power amplifier (RFPA). The gradient amplifiers are driving three independent gradient coils placed along three directions in space for spatial encoding. The RF power amplifier is connected to a transmitter and a power supervision unit, which measures forward and reflected power as a basis for specific absorption rate estimations.

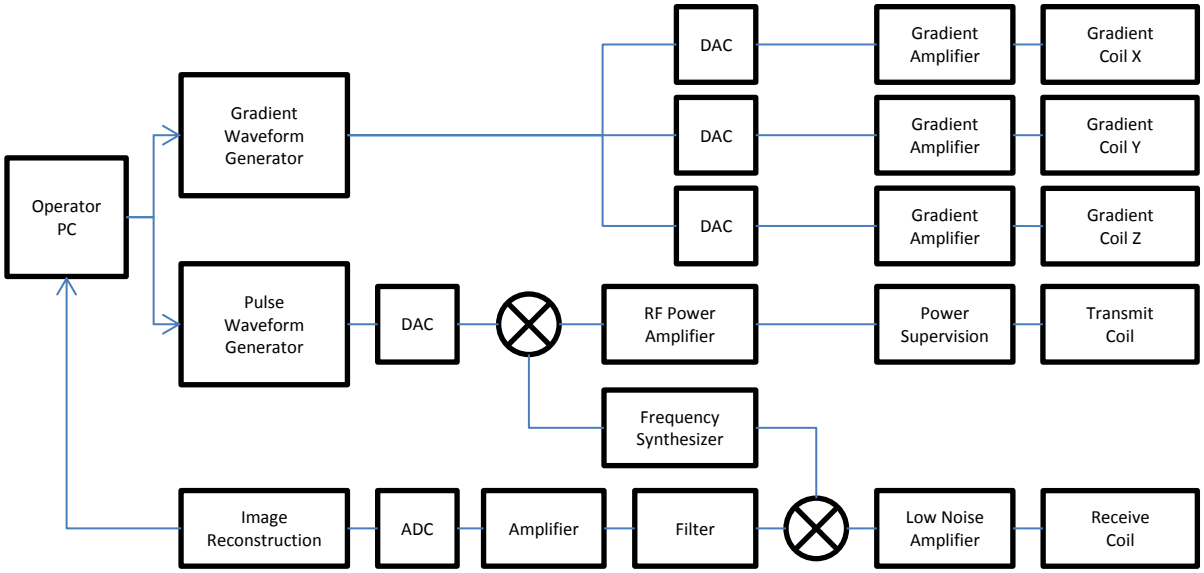

Figure 14: Schematic of the principle functionality of a MRI system.

On the receive side low noise and low impedance preamplifiers are being used. The preamplifiers are ideally placed close to the receiver RF coil to amplify the MR signal and to avoid excessive weighting of additional noise sources hampering SNR. If a transmit/receive RF coil is in place, the transmit path needs to be decoupled from the receive path in order to prevent harm by the use of high transmit peak powers to the preamplifiers. This can be performed by using active and/or passive decoupling circuits in the transmit path. An example of such a circuit is presented in Figure 15a. During transmission both PIN diodes (D1 and D2) are switched on (forward biased) by an appropriate DC current enabling RF power to be send to the RF coil. On the receive path, the capacitor C2 is shortened by the biased PIN Diode D2 leading to C2 and L form a parallel resonant circuit (parallel trap circuit), which shows a high impedance towards the transmit path and decouples it from the input to the low noise preamplifier (LNA). Alternatively instead of a pi-network (C1, C2, L) a λ/4-cable can be used to transform the low impedance generated by the biased PIN Diode D1 to a high impedance as seen by the transmitter [77]. If not used actively, the PIN Diode D1 could be used passively as well, if the transmitted RF power is high enough to exceed its breakdown voltage, D1 conducts and isolates the LNA by means of the parallel resonant circuit (C2 and L) described above [77]. The PIN Diode D2 is used to prevent noise coupling from the transmit to the receive path. To further improve the isolation of the given circuit an inductance can be placed in parallel to the PIN Diodes, to counteract the capacitance of the PIN diodes themselves, which is present in reverse biased operation [77, 78]. To guarantee a proper impedance transformation of the low impedance of the preamplifiers to the RF coil, the electrical length from the LNA to the RF coil needs to be adjusted to 180° [78]. If multi-channel RF coils with multiple TX/RX switches are being used, the electrical length of the transmit path should yield comparable values between individual TX/RX switches to

allow reproducible transmitted pulse shapes. In our experimental setup transmit/receive switches from Stark Contrasts (Stark Contrasts, Erlangen, Germany) which are operated by a 100mA DC current sent by the MR scanner were being used. These switches also include a self-activation circuit to protect the preamplifier (Siemens Healthcare, Erlangen, Germany) for PIN bias failures and allow for transmit power attenuations of >50dB, noise isolations of >40dB and insertion losses of ~0.3 dB. An 8-channel switchbox assembled by my collaborator Harald Pfeiffer (PTB, Berlin. Germany) utilizing theses TX/RX switches is illustrated in Figure 15b.

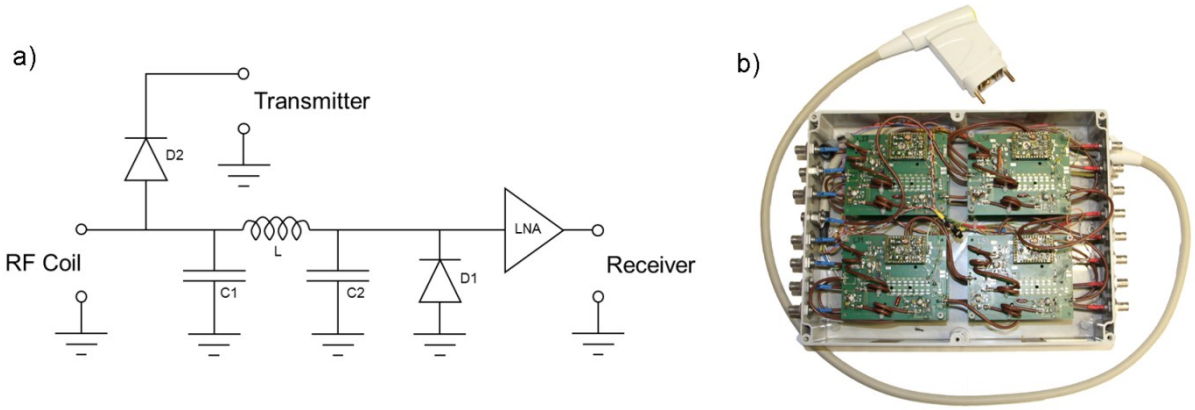

Figure 15: (a) Schematic of the functionality of a transmit/receive switch to isolate the high transmitted voltage peaks in the magnitude of up to ~550 V from the low noise preamplifier (LNA) which operates to attenuate receive signals in mV range [77]. (b) Picture photograph of an 8-channel transmit/receive switchbox, assembled by my collaborator Harald Pfeiffer (PTB. Berlin, Germany), with a vender specific RF coil plug cable to be used on a Siemens 7.0 T MR scanner.

After the received signal is transformed to the pre-amplification, it continues to a filter stage and an additional amplification stage after which an analog-to-digital (ADC) converter per receiver channel creates and saves this information as RAW data. The image reconstruction unit processes the memory consuming RAW data into the open standard of digital imaging and communications in medicine (DICOM) standard to be saved in the database.

3.3.1 Multichannel RF Transmission

RF power transmission is usually performed using a single channel transmission line to feed a large volume or a local RF coil. For multichannel transmission approaches, two concepts are feasible:

1) A semi-dynamic multi-channel transmission approach using electronic components with a fixed phase & amplitude relation between the channels [79, 80]
2) A fully dynamic multi-channel transmission system using dedicated hardware to play out independent but synchronized RF pulse forms per channel [81]

The semi-dynamic approach yields fixed phase and amplitude conditions for a single scan setup and can be modified through hardware changes. This approach provides a legitimate and cheap alternative to a fully dynamic system to apply fixed B_1^+ shim phase settings or SAR reduction [57, 82]. The hardware settings can be realized using power splitters - for example Wilkinson power dividers [83]- with additional phase cables to change the relative phase between channels. A hardware example of a power splitter used throughout the study is shown in Figure 16, here pi-networks are being used for impedance matching which allows for a very compact design tailored for a center frequency of 297 MHz.

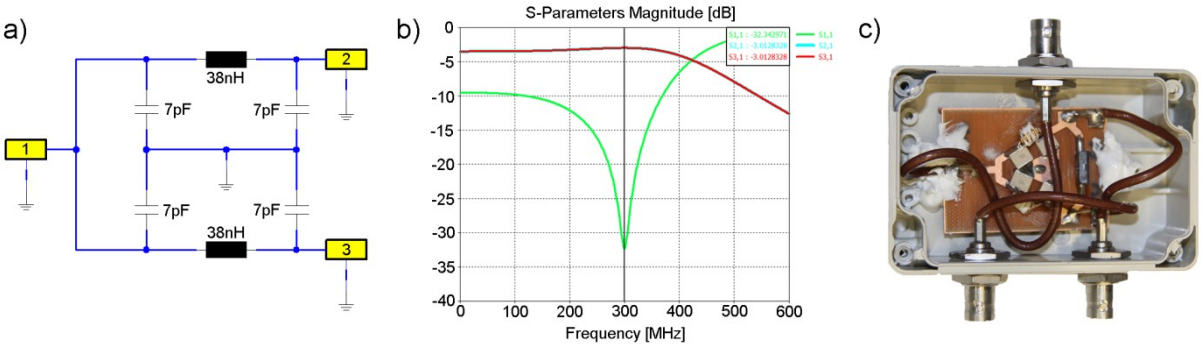

Figure 16: (a) Circuit simulation example of a 1:2 power splitter consisting of a pi-network per channel for impedance transformation between input (Port1) and output (Port2 and Port3). (b) Resulting S-parameter simulation disregarding RF component losses and cable losses. At 298 MHz $S_{21} = S_{31} = -3.0$ dB with $S_{11} < -30$ dB enabling an equal split of the input RF power in two channels. (c) Picture photograph of a constructed 1:2 power splitter (courtesy of MRI.TOOLS GmbH, Berlin, Germany). Please note that the circuit has to be build up symmetrically to avoid phase differences between the two output channels.

Another approach for power splitting is the use of a so-called Butler matrix, which is a beam forming network employing a combination of 90° hybrid couplers and phase shifters [84]. The schematic view of a 4x4 butler matrix is presented in Figure 17a. By using hybrid couplers multiple modes can be generated from a single power input. E.g. a power input at connection 1L (Figure 17a) results in a relative phase increment of 45° and the relative phases A1=0°, A2=90°, A3=45° and A4=135. Figure 17b shows a picture photograph of a 16x16 butler matrix used throughout the study, which was provided by the PTB Berlin, Germany. This configuration comprises 32 hybrid couplers (Figure 17c) (10010-3, Anaren Microwave Inc., New York, USA) and phase shifting cables.

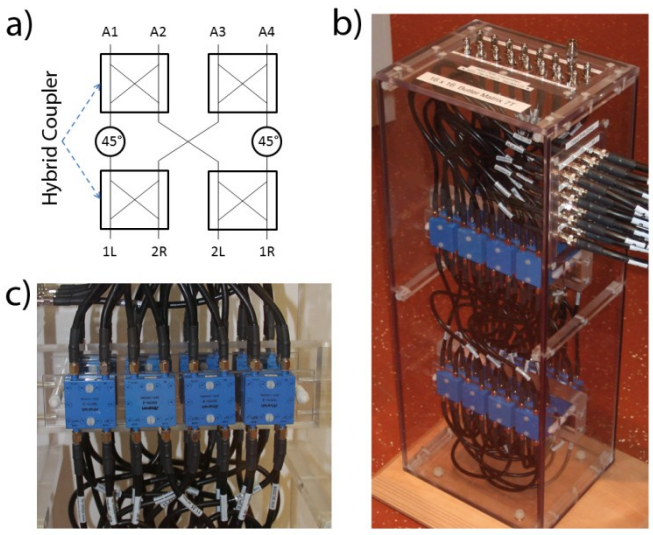

Figure 17: (a) Principle schematic of a 4x4 Butler matrix design. (b) 16x16 channel Butler matrix used throughout the study, which was provided by the Physikalisch Technische Bundesanstalt (PTB) Berlin, Germany. (c) Zoomed view of the hybrid couplers and phase shifting cables used in the 16x16 channel Butler matrix.

Notwithstanding the functionality of the given power splitting approach via phase cables or a Butler matrix, a fully dynamic multi-channel system allows exquisite control of phase and amplitude for each RF channel simultaneously. The MR multi-channel transmit system (TX-Array, Siemens Healthcare, Erlangen, Germany) at the Berlin Ultrahigh Field Facility consists of eight individual channels providing a max power output of 1 kW at the output of the 2x4 RFPA modules. The hardware is being controlled over a Master/Slave architecture of two host computers simulating in total eight MR scanner units, which drive the necessary pulse forms to the RFPAs and are being synchronized by the master system. As compared to the semi-dynamic approach, this has several advantages. The additional degree of freedom opens up room for applications like static B_1^+ shimming [85, 86], dynamic B_1^+ shimming [87, 88], SAR reduction [45, 89], spatial selective excitations [69, 76] or targeted RF heating applications [65]. However care needs to be applied regarding RF safety as the change of relative amplitude and phase contributions alters the applied electromagnectic field distribution inside the human body and consequently SAR. In a single-channel feeding system both forward and reflected power are being monitored over this channel. This static scenario enables sufficient and conservative estimates of the absorbed power used to set safe RF power deposition conditions. For a multi-channel system and time-varying pulses, all individual channels need to be monitored independently. In addition to forward and reflected power recordings, the phase between the channels needs to be acquired. For this purpose directional couplers are being used to get a realistic insight of the power summation over all channels. Once the power distribution is known, electromagnetic field simulation models may be utilized for SAR estimation to limit the power values to safe RF exposure limits [90, 91].

4. RF Coil Developments for UHF MR at 7.0 T

An important precursor to combine targeted RF heating together with UHF MR imaging is the knowledge and capability to design RF coils for UHF MR. The electro-dynamic constraints, physics phenomena and practical obstacles of UHF MRI include but are not limited to excitation field inhomogeneities (B_1^+) and RF power deposition limits. Addressing these challenges requires rather complex RF hardware solutions and insights into the nature of complex EMF field patterns inside the human body [92]. In particular for imaging the human heart at ultrahigh fields , which is regarded as a steam engine of innovation but also as one of the most challenging MR applications. Here the challenges arise primarily from an increase in the ratio of body dimensions versus the RF wavelength, from the arbitrary shape of the upper torso, from the various air/tissue and tissue/tissue interfaces surrounding the heart but also from extended depth penetration requirements due to the location of the heart in the upper torso versus imaging the human brain which simply speaking can be almost considered as a uniform spherical volume. With this in mind this work first focused on the development of many-element transceiver arrays tailored for cardiac MR to master the design, evaluation and application of multi-channel RF coil technology. For this purpose this chapter introduces the benefits and challenges of UHF-MRI, transmit RF coil design criteria and RF coil developments conducted throughout the course of this PhD project.

Fractions of the content presented in this chapter were published in [16, 57, 82, 93-95].

4.1 Benefits and Challenges of UHF-MRI

SNR is the main motivation of applying UHF MRI. It is the driving force for a multitude of clinical applications potentially enabling improved diagnostics for anatomical, functional and metabolic MRI [16, 96-100]. SNR can be significantly increased by increasing the B_0 field strength since the number of excited spins (ΔN) is frequency dependent. SNR is estimated to increase linearly with the field strength and frequency [101]:

$$SNR \sim f \sim B_0 \tag{52}$$

The SNR gain inherent to UHF is accompanied by a number challenges based on physics law and practical obstacles, which needs to be addressed by technological developments. The main difficulties at higher fields arise from static magnetic field inhomogeneities (B_0), RF non-uniformities (B_1^+) and RF power deposition constraints. Whereas B_0 field inhomogeneities are mainly attributed to

practical and economic constraints of the magnet design, B_1^+ non-uniformity and RF power deposition are phenomena introduced by physics and shall be discussed further in this chapter.

4.1.1 B_1^+ Field Inhomogeneities

One of the main challenges at UHF is the increased Larmorfrequency of the circular polarized magnetic flux density B_1^+ [102]. The RF wavelength λ is given by the ratio between the phase velocity v and frequency f. In a dielectric medium – dielectric constant or relative permittivity $\varepsilon_r > 1$ – the wave velocity is reduced and the wavelength is shortened by the refractive index $\sqrt{\varepsilon_r \mu_r}$. In biological tissue, which is a lossy dielectric, the tissue conductivity further reduces the wavelength based on:

$$\lambda(f) = \frac{\sqrt{2}}{f\sqrt{\mu_r \mu_0 \varepsilon_r(f) \varepsilon_0}} \left[\sqrt{1 + \left(\frac{\sigma(f)}{2\pi f \varepsilon_r(f) \varepsilon_0} \right)^2} + 1 \right]^{-1/2} \tag{53}$$

with the vacuum permittivity $\varepsilon_0 = 8.85 \cdot 10^{-12} F/m$. The frequency dependent effects of conductivity, relative permittivity and the wavelength for various representative biological tissues are plotted in Figure 18. At 1.5 T the wavelength in muscle tissue is approximately $\lambda(64MHz)$ ≈40cm. At 7.0 T the wavelength is significantly reduced to $\lambda(298MHz) \approx 12cm$. At UHF the wavelength becomes relatively short compared to the human torso geometry or even compared to the human brain.

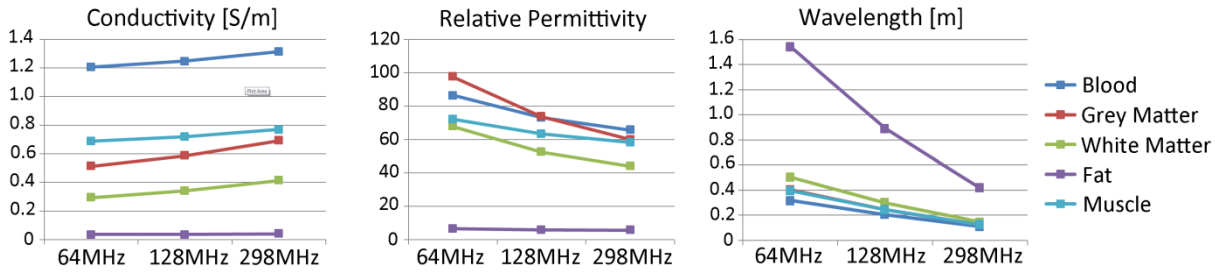

Figure 18: Conductivity, relative permittivity and wavelength dependent on the applied frequency of a 1.5 T (64 MHz), a 3 T (128 MHz) and a 7 T (298 MHz) MR system of/in biological tissue [103-105].

The short wavelength regime constitutes a major challenge for imaging due to highly complex interference patterns and non-uniform B_1^+ distributions inducing signal non-uniformities if not signal voids as demonstrated in Figure 19. Large volume birdcage body coils, while widely used in clinical 1.5 T and 3.0 T MR systems, become ineffective for UHF human MR imaging (B_0 > 7.0 T) due to the lack of freedom to adjust the current density pattern on the RF coil in order to compensate for B_1^+

field inhomogeneities [102]. This challenge can be addressed by using B_1^+ shimming techniques and multi-channel transmit RF technology [57, 85, 106].

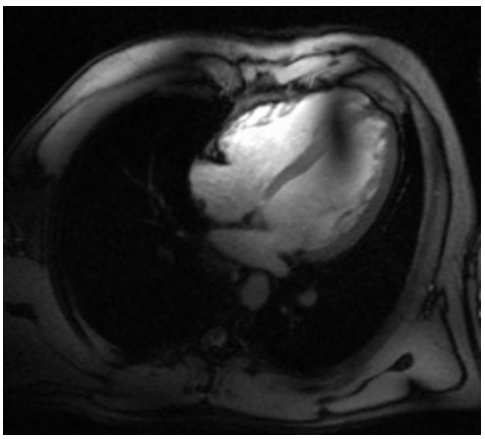

Figure 19: Signal voids through the apical and midventricular septum of a four chamber view of the heart acquired at 7.0 T due to B_1^+ transmission field inhomogeneities at UHF. The RF coil used was a 4-channel TX/RX array together with a fixed B_1^+ shim setting calculated from EMF simulations [80]. A fixed phase setting, which is being optimized based on a single torso geometry and anatomy, might lead to B_1^+ inhomogeneities for different base parameters like body mass index and/or positioning of the RF coil. Proper RF coil design may counteract these limitations and provide more robust transmission field homogeneities over a wider range of human geometries and electromagnetic properties [57].

4.1.2 RF Power Deposition Considerations

For frequencies ranging between 100 kHz to 10 GHz the predominant effect of RF power deposition in biological tissue is tissue heating based on energy absorption [107]. RF power deposition considerations play a pivotal role for MR safety and hence govern the design and development of MR hardware and methodology. Since it is challenging to measure internal body temperature changes, RF heating in biological tissue is evaluated by the assessment of the specific absorption rate (SAR) [91]. SAR at the location $\vec{r}$ in tissue is given by:

$$SAR = \int \frac{\sigma(\vec{r}, f)|\vec{E}(\vec{r})|^2}{\rho(\vec{r})} d\vec{r} \tag{54}$$

with $\sigma(\vec{r}, f)$ the frequency dependent conductivity of tissue, $\rho(\vec{r})$ the tissue density and $\left|\vec{E}(\vec{r})\right|$ the magnitude of the electric field vector. According to equation (54) SAR is proportional to the square of the magnitude of the E-field vector generated by the transmit RF coil. RF power deposition limits relevant for MR are given by the International Electrotechnical Commission (IEC) guideline IEC (2010) 60601-2-33 [91]. This guideline defines limits for whole body average SAR (normal mode: 2.0 W/kg,

1st level controlled mode: 4.0 W/kg), partial body average SAR (normal mode: 2.0-10.0 W/kg, 1st level controlled mode: 4.0-10.0 W/kg) and maximum local SAR (averaged over a cube of 10 g averaging mass, normal mode: 10.0 W/kg, 1st level controlled mode: 20.0 W/kg). For MRI at 1.5 T and 3.0 T a volume body coil is commonly used for transmission so that whole body SAR is considered to be the limiting factor for RF input power. At UHF-MR local transceiver RF coils are typically positioned close to the body region of interest so that maximum local SAR can be applied for RF power assessment. Careful SAR evaluation is required before any RF coil array can be employed in human MR studies. For this purpose numerical electromagnetic field simulations are applied. SAR evaluation should not be limited to maximum local assessment but should also include transmit efficiency and power efficiency to characterize RF coil performance:

$$Transmit\ efficiency = B_1^+ / \sqrt{P_{delivered}} \tag{55}$$

$$Power\ efficiency = B_1^+ / \sqrt{maxLocal\ SAR_{avg}} \tag{56}$$

With $P_{delivered}$ being the input peak power delivered to the RF coil.

Due to the short wavelength regime at ultrahigh field fields, which affects also the E-field distribution inside the body and offsets some of the SAR predictions governed by [108]:

$$SAR \propto \frac{B_1^2 B_0^2 \tau_{RF}}{mTR} \tag{57}$$

with τ_{RF} being the duration of the RF pulse, TR representing the repetition time of RF, τ_{RF} the RF pulse duration and m referring to the tissue mass. In other words, for the same input power the B_1^+ field generated by a RF coil at location x is lower at higher frequencies. Thus, a higher power needs to be applied to the RF coil to achieve similar flip angles. This additional increase in power elevates the E-field components as well and leads to higher energy absorption governed by tissue equation (54). Additionally the frequency dependent increase in conductivity increases SAR even more at higher field strengths (Figure 18). RF power deposition is substantially affected by the geometry of the upper torso, by positioning of the RF coil with respect to the torso or the head, by the RF coil design, by the number of RF transmission channels as well as by the RF driving conditions. Here, numerical electromagnetic field simulations are instrumental if not essential to provide an insight into the local SAR distribution.

Figure 20 illustrates $B_1^+/\sqrt{kW}/\sqrt{Max\ local\ SAR_{10g}}$ distribution for a cardiac optimized four-channel TX/RX array at 1.5 T, 3.0 T and 7.0 T [16, 80]. For this purpose the two RF coil formers were placed in an anterior and posterior position with respect to the upper torso of the voxel model ''Duke'' from the virtual family [109]. For this configuration a lower B_1^+ is achieved for the given local SAR values when moving to higher frequencies. Consequently, a higher RF power deposition is needed to achieve the same flip angle at higher fields. For the 4-channel transceiver configuration the increase in local SAR to achieve the same flip angle is not as pronounced as previously reported for a single RF loop cardiac coil [110]. For this 4-channel configuration a B_1^+ decrease of a factor 3.7 was observed for the mid-ventricular septum when moving from 1.5 T to 7.0 T. In comparison, the same myocardial region showed a 1.7-fold B_1^+ decrease when moving from 3.0 T to 7.0 T. For an apical region a B_1^+ decrease of factor 2.9 (7.0 T vs. 1.5 T) and factor 1.5 (3.0 T vs. 1.5 T) was obtained. The resulting increase in SAR as compared to a 1.5 T system is depicted in Figure 21.

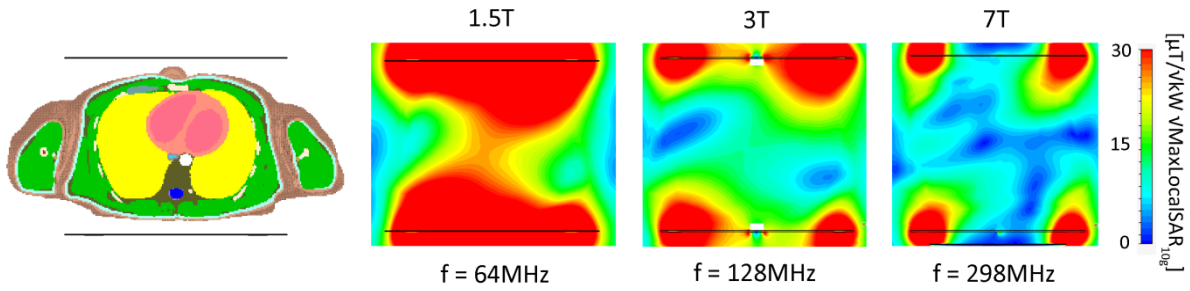

Figure 20: RF power deposition of a cardiac optimized 4-channel RF coil array at 1.5 T, 3.0 T and 7.0 T. For each configuration identical phase settings are used for B_1^+ and local SAR (10g average, 1W input power) calculations. The $\mathbf{B_1^+/\sqrt{kW}/\sqrt{max\ local\ SAR_{10g}}}$ distribution is shown for three discrete MR frequencies and normalized to an efficiency of $\mathbf{30\mu T/\sqrt{kW}/\sqrt{W/kg}}$. The local SAR_{10g} had comparable values at 1.5 T (0.30W/kg), 3.0 T (0.30 W/kg) and 7.0 T (0.22 W/kg) [16].

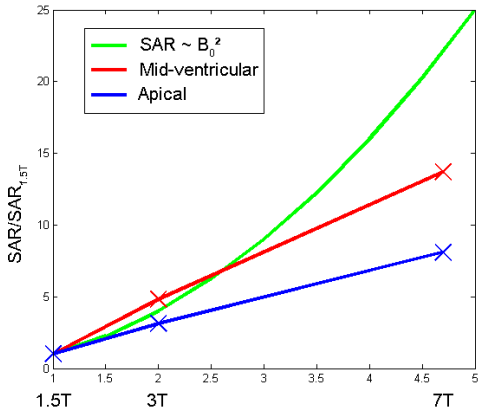

Figure 21: Simulated increase in RF power deposition of a 4ch TX/RX cardiac RF coil at 1.5 T, 3.0 T and 7.0 T in comparison to the increase governed by the squared ($SAR \sim B_0^2$) relation.

Regional SAR differences reported for UHF-MR underline that local SAR depends on the geometry and location of the target anatomy, the RF coil configuration and the transmission field uniformity applied for UHF-MR. Furthermore a change in amplitude and phase of each individual transmit channel – commonly used for transmission field shimming [89] or parallel transmission [69, 76, 87, 88] –may induce significant alterations in local SAR as demonstrated in Figure 22.

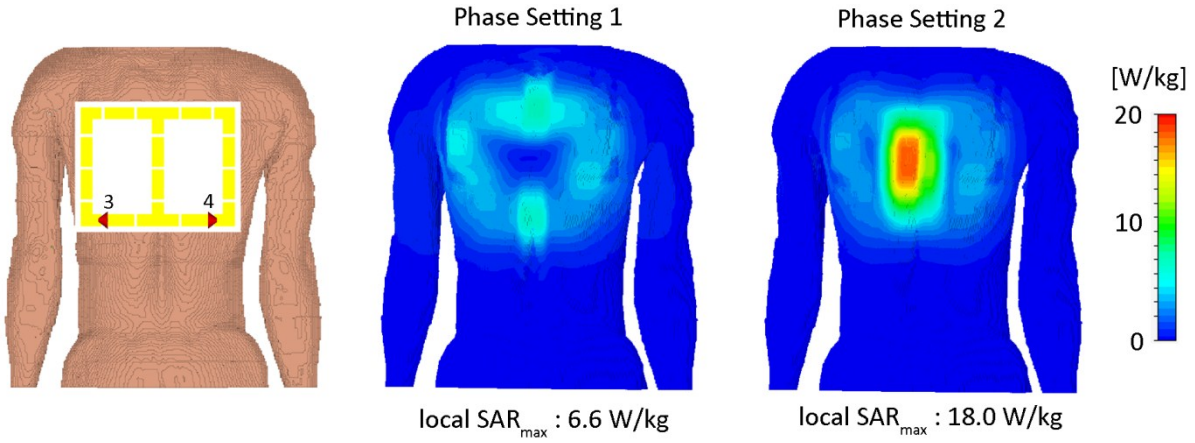

Figure 22: Impact of B_1^+-shimming on 10g average local SAR in the posterior (Ch3, Ch4) part of a simulated 4-channel TX/RX cardiac array (left) [80] and the voxel model "Duke" from the virtual family [109]. Local SAR_{10g} of phase setting 1 (Ch1 = 0°, Ch2 = 180°, Ch3 = 0°, Ch4 = 180°) (middle) and of the same cardiac RF coil with a cardiac optimized phase setting 2 (Ch1 = Ch2 = Ch3 = Ch4 = 0°) (right). Please note that only the phase contributions of each channel were modified which leads to local SAR_{10g} changes by a factor as high as ~2.7 [82].

The maximum local SAR increases by a factor of 2.7 when using two different phase settings (phase setting 1: channel 1 = 0°, channel 2 = 180°, channel 3 = 0°, channel 4 = 180°, phase setting 2: phases of channel 1 = 0°, channel 2 = 0°, channel 3 = 0°, channel 4 = 0°); no amplitude modulation was applied.

Although SAR is key for RF safety evaluations it should be noted that the temperature distribution – which is the cause of tissue damage based on RF heating – does not follow SAR in a straightforward manner [111]. Thermoregulation and heat transfer inside the body (e.g. blood vessels) need to be considered while moving towards a more realistic scenario. Here ongoing research already focusses on temperature modeling instead of SAR models, suggesting a thermal tissue damage threshold $CEM_{43}°C$ known from thermal therapies [112-114]. These explorations will help to advance towards enhanced MR safety assessment for UHF-MR. While the technical details of characterizing SAR and temperature are being perfected, methods for interpreting the results of these calculations in the light of regulatory limits also warrant discussion [111]. Numerical simulations showed that maximum local SAR regulatory limits were exceeded by a significant factor when whole body volume RF coil

configurations at 1.5 T and 3 T were adjusted to whole body SAR power limitations [111]. This implies that today's UHF MR widely operates at more conservative assumptions than generally used for MR at lower fields adding an additional factor on RF power deposition constraints for UHF MR. However, RF coil design might provide a valuable tool to improve transmit efficiency, power efficiency and RF homogeneity in order to enable SAR intense imaging applications such as steady state free precession (SSFP) [115, 116] or Rapid Acquisition with Relaxation Enhancement (RARE) [117, 118], which up to date are elusive in e.g. a clinical setting for UHF cardiovascular MRI (CMR) at ultrahigh fields. $\vec{E}$

4.2 Basic RF antenna concepts for UHF MR

RF antenna concepts used for UHF body imaging can be categorized in three basic concepts: 1) Loop RF coils [80, 99, 119, 120], 2) stripline arrays [102, 106, 121] and 3) the recently introduced dipole antenna [122]. The three fundamental designs, together with their characteristic transmitted E- and H-field distributions are displayed in Figure 23. The most common element design for receive only RF coils at current clinical field strengths ($B_0 \leq 3.0$ T) is the RF loop coil (Figure 23). The main reason behind the use of loop arrays for reception are ultimate intrinsic SNR calculations favoring a circular current path for such field strengths [47, 48, 123]. A RF loop coil generates a circular H-field polarization along the current path of the conductive loop. At the center of the loop a magnetic field vector is generated which is perpendicular to the phantom surface, whereas at the same time the E-field components are restricted to the proximity of the conductor and lumped elements, avoiding power deposition in tissue along the center of the loop. RF loop coils have successfully been implemented in UHF MR for head imaging [124, 125] as well as whole body applications [80, 119]. Another design that was among the first suggested RF coil arrays for UHF imaging is the so-called stripline or transmission line array [106, 126, 127]. One element consists of a ground plane and a central conductor made by a highly conductive material (e.g. copper) with a low loss dielectric material (e.g. PTFE, $\varepsilon \approx 2$) placed between them (Figure 23). The feeding point can be located either at one end of the element or it can be positioned in the middle allowing for central feeding [128, 129]. The open ends are terminated with a capacitor. The H-field and E-field lines are concentrated in the dielectric between the conductors. The generated H-field vector is parallel to the surface of the imaging object rather than perpendicular as compared to the RF loop coil (Figure 23). The E-field on the other hand, is parallel to the z-axis or the length of the stripline, whereas the E-fields of the loop follow the conductor in a circular fashion as illustrated in Figure 23. With regards to power deposition consideration, the loop design showed to be beneficial for UHF MRI versus the stripline elements, since local SAR can be spread over a wider area and peak local SAR values are reduced [122].

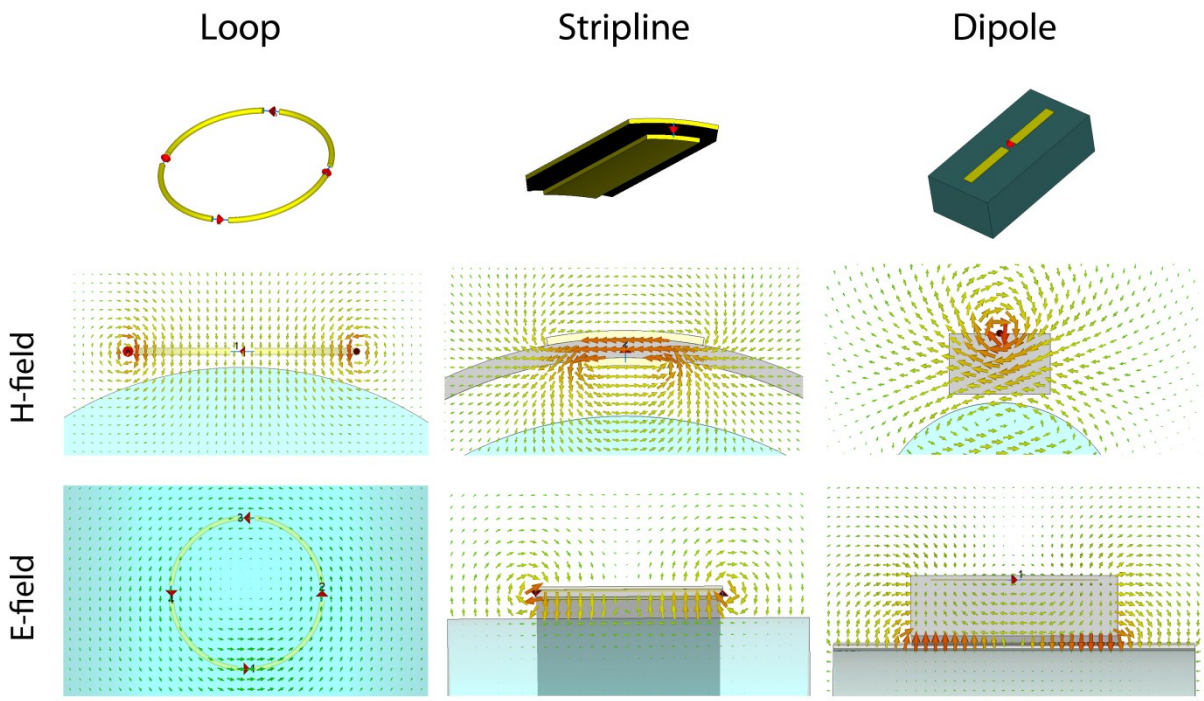

Figure 23: Three basic UHF MR antenna designs and their H- and E-field distribution as calculated in numerical EMF simulations. Logarithmically scaled vector plots are shown for the loop (left), the stripline (middle) and the dipole (right) structures.

More recently, dipole antennas together with a high permittivity dielectric were proposed as transmit/receive elements for UHF MRI [122]. The combination of high dielectric and a dipole antenna shows a more homogeneous B_1^+ profile and an increased depth penetration as compared to loop and stripline designs [122]. Furthermore these elements might benefit from ideal current pattern considerations for ultimate intrinsic SNR, which show electric dipole components for B_0 = 7.0 T rather than curled components [47, 48]. The H-field of a dipole is circulary shaped around the centrally fed strip and transmitted through the low loss dielectric which enables good coupling to the imaging object (Figure 23). The H- and E-field distribution shows similarities to a stripline array, with the E-field parallel to the length of the dipole and the H-field perpendicular to it and parallel to the surface. The dipole as shown in Figure 23 is more efficient in the transmission of RF energy to the object, enabling higher depth penetration, a more symmetric B_1^+ profile in the axial plane and lower peak SAR values as compared to the stripline element [122].

An extrapolation from a single element performance to a multi-channel transmit/receive structure is not a straightforward task since complex interference patterns and RF design specifications need to be considered. The following paragraphs introduce the design of an 8-channel and a 16-channel TX/RX cardiac RF coil array for UHF CMR [93, 94] as part of this work, discusses its specifications and evaluates the RF coil performance in *in vivo* clinical applications [57]. The RF coil performance was

benchmarked against a previously published 4-channel cardiac RF coil [80]. The insights gained were converted to implement a 32-channel transceive cardiac array, which completes this chapter [95] on route to the hybrid applicator tailored for targeted RF heating and diagnostic imaging.

4.3 One Dimensional 8-Channel Transceiver Cardiac Array

The number of RF channels presents an important design criterion for multi-channel transmit/receive RF coil arrays. On the reception site, a higher number of receive channels boosts SNR and parallel imaging performance [70, 130, 131]. Specifically for cardiac imaging fast imaging techniques are required, since cardiac motion and respiratory motion pose a challenge for high resolved image acquisition. On the transmission side, an increase in number of channels results in a higher degree of freedom, promising improved B_1^+ field homogeneity control. For all these reasons an 8-channel TX/RX cardiac RF coil array for 7.0 T was designed and built as part of this thesis project [93]. The array consisted of loop elements, which balance B_1^+ depth penetration and SAR [122]. It comprises a posterior and an anterior section as shown in Figure 24. The anterior section was curved to conform to an average chest. Five loop elements were laid out to cover the left side of the anterior torso. The posterior section comprises three elements, a planar shape and was integrated into the patient table cushions as illustrated in Figure 24d. The loop elements of the anterior section cover a surface area of 12 cm² using an element size of 6 cm x 20 cm. A surface area of 18 cm² was chosen for the posterior loop elements with an element size of 9 cm x 20 cm. The asymmetric design together with placing more and smaller elements at the chest versus the back is advantageous for cardiac imaging [53, 132]. Larger elements in the posterior section utilize the higher penetration depth to reach the cardiac target region. The extension of the loop elements along the head-feet direction was set to 20 cm to cover the entire heart. The left–right extension was set to 30 cm for the set of five anterior elements and 29 cm for the set of 3 posterior elements to achieve whole heart coverage. Decoupling of adjacent RF coil elements was accomplished with a common conductor and a shared decoupling capacitor. This approach is beneficial since it uses a simple conductor design and provides less loss due to the absence of destructive currents in neighboring loops. The conductor width was set to 20 mm. A RF shield made of slotted copper foil to minimize eddy currents was placed above the array to reduce radiation losses. A distance of 2 cm between the loop elements and the shielding was used to balance field distribution and geometric constraints. For each loop element a cable trap was placed in the feeding cable with its position being in a distance of 1/12 of the wave-length along each cable. The cable traps were designed as a tuned parallel resonant circuit, consisting of a single loop of the cable and a capacitor. This approach imposes large impedance to signals conducted on the shield of the coax cable for a resonance frequency of 298 MHz. The RF coil casing was designed with the

computer aided design (CAD) tool Autodesk Inventor 2011 (Autodesk Inc., San Rafael, CA, USA) and printed with a 3D rapid prototyping system BST 1200 es (Dimension Inc., Eden Prairie, MN, USA) using ABS+ material. The casing was tailored to provide a minimum distance of 15 mm from any part of the loop structure to the human tissue. This helps to reduce SAR hotspots in the vicinity of the RF coil. The posterior section was designed to accommodate the weight of a human, while the lightweight design of the anterior section (2.3 kg) offers patient comfort and ease of use.

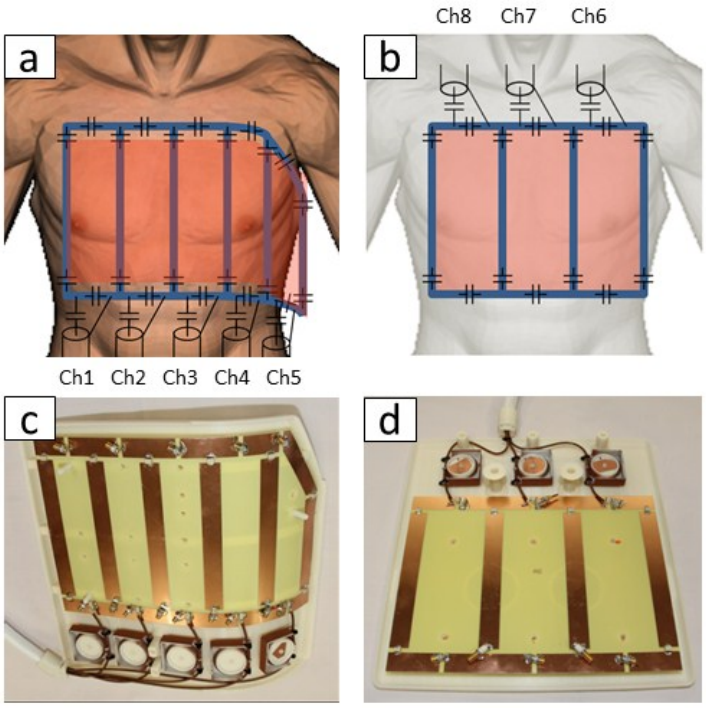

Figure 24: Tailored 8-channel transmit/receive cardiac RF coil array for cardiac MR at 7.0 T. a) Circuit diagram and positioning of the 5-channel anterior RF coil section with the RF shield shaded in red. b) Circuit diagram and positioning of the 3-channel posterior RF coil section with the RF shield shaded in red. Constructed loop structure of the anterior 5-channel RF coil (a) and the posterior 3-channel RF coil (d) with matching networks and cable traps in the 3D printed casing [93].

4.4 Two Dimensional Arrangement of a 16-Channel Transceiver Array

The 8-channel 1D array as well as other designs for 7.0 T TX/RX RF coil configurations have mainly laid out with the number of channels being placed along one dimension (left-right) [80, 93, 106, 122]. Modulating the transmission field by means of a 2D arrangement of a transceiver RF coil array affords the coverage of another (for example: head-feet versus left-right) dimension. This approach has been proven to enhance RF shim efficiency of a RF coil array curtomized for head imaging [133]. Consequently transceiver arrays with elements placed along the left-right direction and the head-feet

direction are natural candidates to further address RF-related obstacles ofcardiac imaging at ultrahigh fields .It has been furthermore predicted that ultrahigh field strengths can allow reduced noise amplification in parallel imaging, which can be used to offset some of the RF power deposition constraints [134, 135]. Here, the additional number of channels along the head-feet direction is benefitial for UHF CMR, due to the heart's position in the chest cavity and the double-oblique orientation of the standard cardiac views used in clinical CMR. For all these reasons, a 16-channel TX/RX RF coil based on loop elements was designed and constructed [94] as illustrated in Figure 25. For sufficient patient comfort and ease of use, the RF coil array was designed to consist of a modestly curved anterior section (Figure 25b) to fit an average torso and a planar posterior section (Figure 25d) integrated into the patient table cushions. The rectangular loop elements were arranged in two rows along the head-feet direction slightly shifted along the left-right direction to allow for decoupling capacitor placement between all neighboring elements (Figure 25b). A high number of channels provides increased control over the B_1^+ distribution and supports parallel imaging with modest to high acceleration factors [130]. The number of channels is related to the element size via the anatomy of the torso and the desired field of view. The size of the individual loop elements influences the ratio of unloaded to loaded Q-factors [136] and mutual coupling via the distance of next-neighboring elements. For both sections of the array an identical arrangement of eight elements in a 2x4 pattern with an element size of (6x13) cm² was found to meet the needs of whole-heart coverage while balancing element size and number of TX/RX channels. Based on EMF simulations, a conductor width of 2 cm was chosen to balance the competing constraints of B_1^+ uniformity, ohmic losses, and SAR. An RF shield made of slotted copper foil to minimize eddy currents was placed above the array to reduce radiation losses. Preliminary experiments showed that a gap of 2 cm between the RF shield and the RF coil array resulted in sufficient decoupling of neighboring and next-neighboring elements for the given layout. The structure depicted in Figure 25b was etched on a board of FR-4 material. Ceramic capacitors (American Technical Ceramics, Huntington Station, NY) and nonmagnetic trim capacitors (Voltronics, Denville, NJ) were placed at the positions indicated in Figure 25a. A solid casing was designed to meet the needs of patient comfort and ease of use using Autodesk Inventor 2010 (San Rafael, CA). The RF coil casing was constructed with the rapid prototyping system BST 1200es (Dimension, Eden Prairie, MN) using ABSplus material (acrylonitrile butadiene styrene). The casing assured a minimum distance of 1.5 cm between the RF coil conductors and the tissue in order to prevent excessive tissue heating due to the high electric fields in the close vicinity of the conductors and capacitors. Also, the casing provides safety and comfort since it prevents contact to any electrical conductor of the RF coil array. One custom-built cable trap per channel was mounted to the coaxial connectors at a distance of 10 cm to the feeding point. Cable traps were designed as single-turn solenoids of the coaxial cable itself with an appropriate capacitor soldered to the outer conductor at

the crossing of the cable to achieve an effective reduction of shield currents at 297 MHz. For the anterior section, the cable traps were placed behind the RF shield to avoid coupling with the RF coil elements. Additionally, all cable traps were shielded individually using copper varnish to further reduce coupling with the RF coil elements and mutual coupling between cable traps.

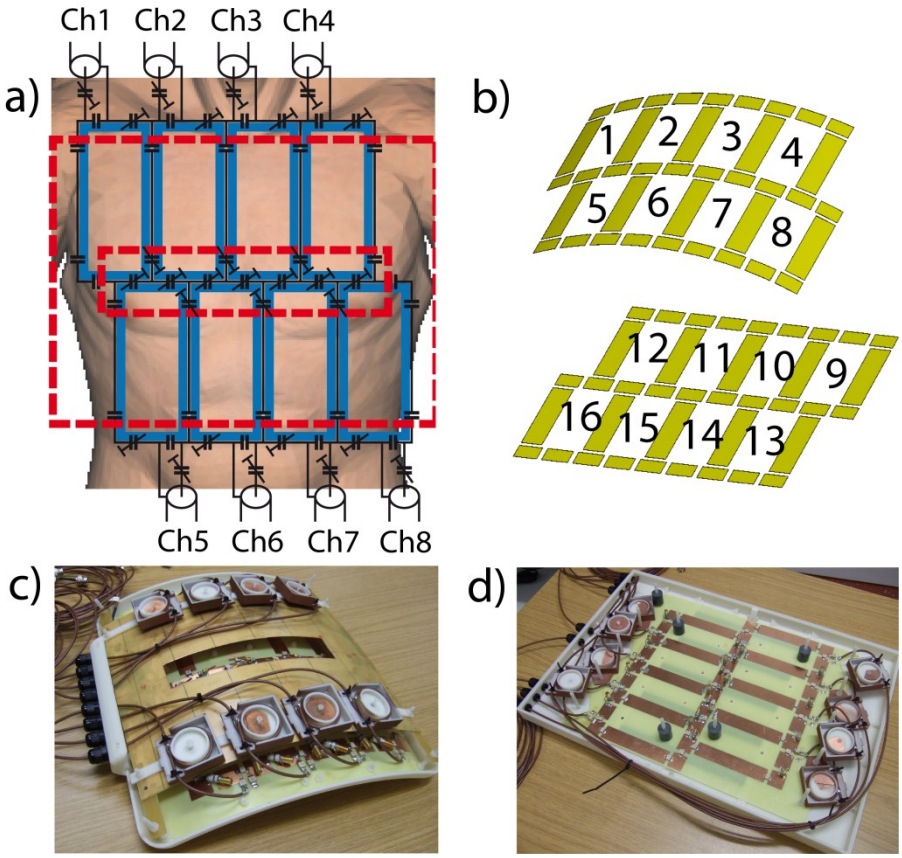

Figure 25: (a) Schematic of the circuit diagram of the anterior section of the 16-channel RF coil array superimposed to a virtual torso. Coil elements are depicted in blue and the RF shield contours are visualized as red dashed lines. A rectangular hole has been cut into the RF shield to enable access to the trim capacitors. **(b)** Schematic of the RF coil array identifying the individual elements. **(c)** Picture photograph of the anterior section showing the cable traps mounted on top of the RF shield. **(d)** Picture photograph of the posterior section without the RF shield [94].

4.5 In-vivo Evaluation of RF Coil Performance

To assess clinically relevant performance criteria for the aforementioned 8-channel [93] and 16-channel [94] RF coil designs, an *in vivo* evaluation study was performed and benchmarked against a 4-channel transceiver array [80] in a routine clinical setting. All three RF coils are illustrated in Figure 26 together with their positioning on a mannequin mimicking the human torso.

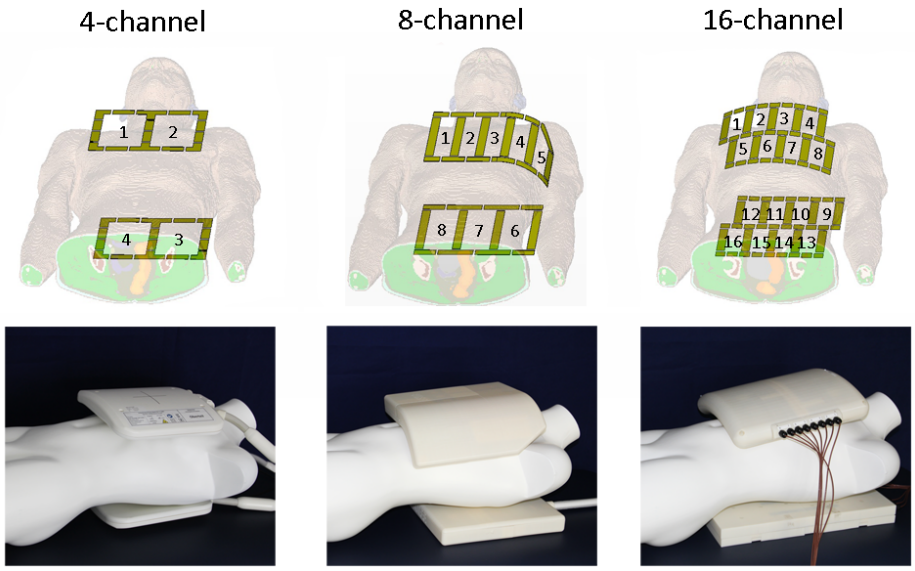

Figure 26: Basic schemes (top) and picture photographs (bottom) of the three TX/RX RF coil designs used in this study: *left* 4-channel TX/RX RF coil with two anterior and two posterior elements of 13x20 cm² (S-I dimensions: 20 cm, L-R dimension: 26 cm), *center* 8-channel TX/RX RF coil with five anterior elements each 6x19 cm² plus three posterior elements of 9x19 cm² (S-I dimension: 21 cm, L-R dimension: 31 cm), *right* 16-channel TX/RX RF coil with eight anterior and eight posterior elements of 6x13 cm² (S-I dimension: 28 cm, L-R dimension: 29 cm) [57].

The RF coil comparison comprises safety evaluation, image quality assessment, SNR and contrast to noise ratio (CNR) analysis, examination of parallel imaging performance, and cardiac chamber quantification. Additional constraints were the use of a single RF shim phase setting and no patient specific matching of the RF coils. This approach allows for volunteer scanning times similar to those used in a clinical scenario lower field strengths. The reflection coefficients were below -13 dB and the transmission coefficients were below -12 dB for all RF coils and volunteers, demonstrating sufficient matching and decoupling conditions. Ten volunteers [seven males; mean ± standard deviation age 27.5 ± 4.1 years, range 24–38 years; mean ± SD body mass index 21.4 ± 2.8 kg/m2, range 18.4–26.8 kg/m², normofrequent sinus rhythm 67 ± 7 bpm] underwent CMR at 7.0 T.

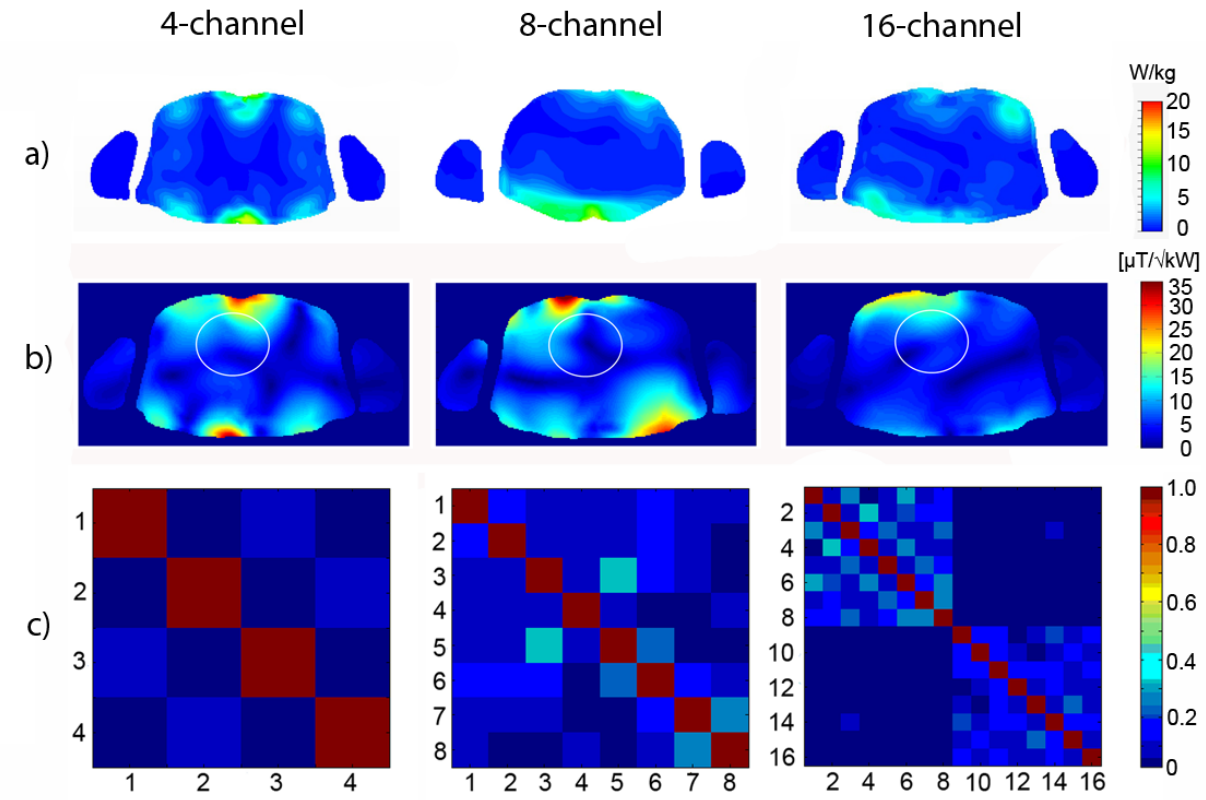

Figure 27: a) SAR distribution (local SAR, 10g average) derived from EMF simulations for an axial slice where the maximal local SAR value was found. b) Simulations of the transmit field efficiency in a mid-axial view. The white ROI indicates the position of the heart. c) Normalized noise correlation matrices averaged over 10 subjects [57].

RF Safety assessment using numerical simulations revealed that all three RF coils stay well within the limits of first level controlled mode for maximum local SAR of 20 W/kg as given by the IEC [91] guidelines and illustrated in Figure 27a. For a total input power of 30 W maximum local SAR (10 g average) was found to be 17 W/kg for the 4-channel, 13 W/kg for the 8-channel and 11 W/kg for the 16-channel RF coil. Increasing the number of channels and spreading out the conductive pathway over a wider area is beneficial to decrease local SAR_{10g}, as the local SAR_{10g} values for all three RF loop coil arrays were found to be superficial. Consequently the 16-channel RF coil shows the lowest local SAR_{10g} values for the same power input. Regarding the simulated B_1^+ distribution, depicted in Figure 27b, the 4-channel RF coil showed the highest transmit efficiency with 7.4 ± 3.6 µT/$\sqrt{}$kW over an ROI encompassing a mid-axial view of the heart. In comparison, the 8-channel RF coil showed a transmit efficiency of 5.4 ± 3.1 µT/$\sqrt{}$kW and the 16-channel RF coil revealed 6.5 ± 3.1 µT/$\sqrt{}$kW. The lowest relative change in B_1^+ (highest B_1^+ homogeneity) was found for the 16-channel RF coil with ±48% standard deviation versus ±49% for the 4-channel RF coil and ±57% for the 8-channel RF coil. The measured and averaged noise correlation matrix is illustrated in Figure 27c yielding maximum values of 0.11 ± 0.04 for the 4-channel RF coil, 0.25 ± 0.05 for the 8-channel RF coil and 0.19 ± 0.02 for the 16-channel and indicating decent noise decoupling for all three RF coil arrays.

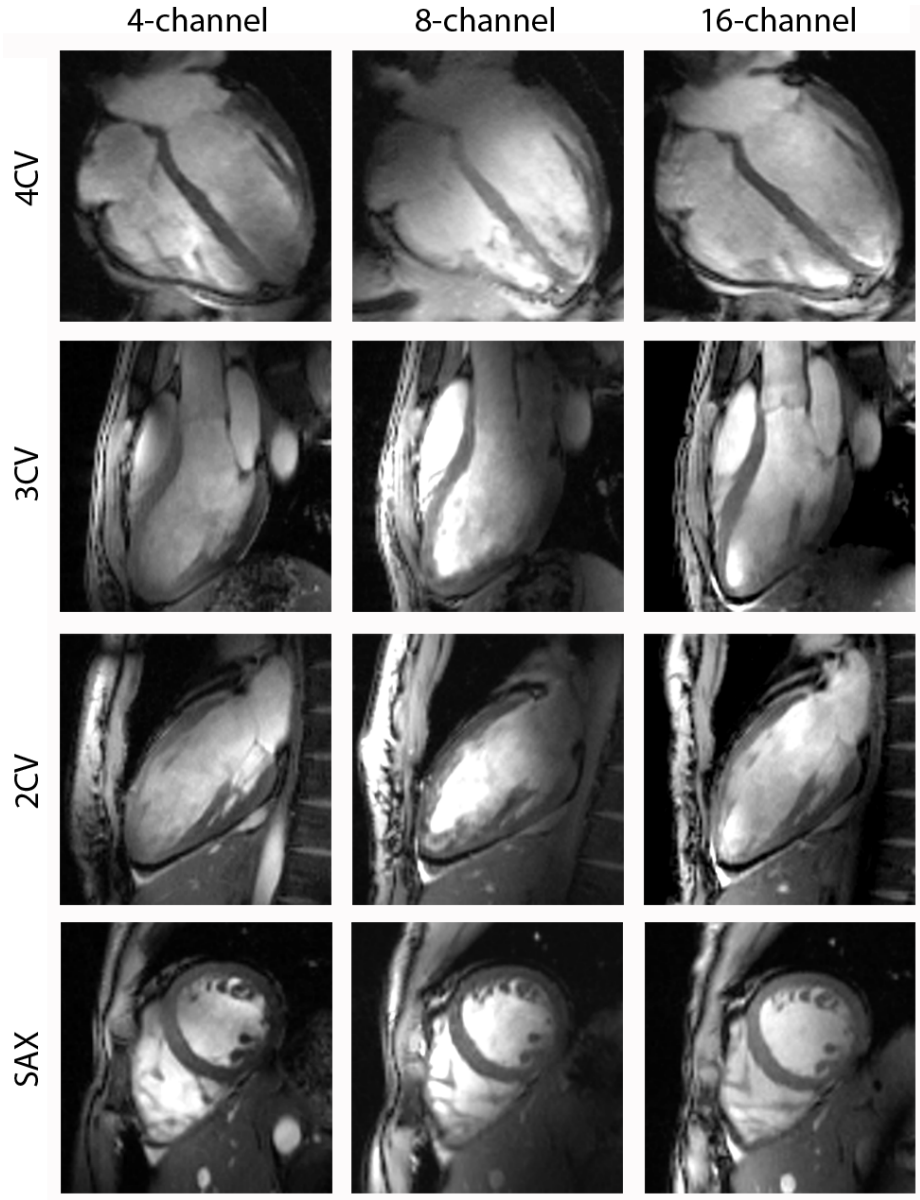

Figure 28: 2D Cine FLASH images of a healthy subject's heart obtained with the the 4-channel (left), 8-channel (middle) and 16-channel (right) TX/RX RF coil array. A four-chamber view (4CV), three-chamber view (3CV), two-chamber view (2CV), short-axis view (SAX) obtained at end-diastole are displayed [57].

For the *in vivo* evaluation a single B_1^+ shimmed phase setting was used for each RF coil, which was precalculated based on EMF simulated data derived from the human voxel model Duke from the virtual family [109]. These phase settings were realized as follows: For the 4-channel RF coil the input power was split with a 1:4 power splitter with additional phase cables (Ch1=225°, Ch2=45°, Ch3=180°, Ch4=0°) and connected over a transmit/receive switchbox to the RF coil. The 8-channel RF coil used a 1:2 power splitter connected to two 1:4 power splitters to generate eight individual power transmit paths, where each path was equipped with phase delay cables (Ch1=315°, Ch2=0°, Ch3=135°, Ch4=130°, Ch5=245°, Ch6=0°, Ch7=30°, Ch8=60°). The 16-channel RF coil was operated over the 1L mode of a 16x16 channel Butler matrix shown in Figure 17b. This approach resulted in a

phase increment of 22.5° between the RF output channels. For the posterior section of the 16-channel RF coil additional 78° phase delay cables were incorporated to accomplish the final RF shim phase setting (Ch1=0°, Ch2=45°, Ch3=90°, Ch4=135°, Ch5=22.5°, Ch6=67.5°, Ch7=112.5°, Ch8=157.5°, Ch9=102°, Ch10=147°, Ch11=192°, Ch12=237°, Ch13=124.5°, Ch14=169.5°, Ch15=214.5°, Ch16=259.5°) which was estimated empirically. For each subject a two-chamber view (2CV), three-chamber view (3CV), four-chamber view (4CV) of the left ventricle (LV) was acquired together with a set of short-axis views ranging from the atrioventricular ring to the apex of the heart (Figure 28). The imaging protocol was as follows: Images were acquired using a 2D CINE FLASH technique [34] with the following parameters: field of view (FOV) (360x326) mm^2, TE = 2.7 ms, TR = 5.6 ms, receiver bandwidth 444 Hz/px, volume selective B_0 shimming, 30 cardiac phases, temporal resolution 33 ms (average heart rate of 60 bpm), 8 views per segment, retrospective gating using an MR stethoscope (EasyACT, MRI.Tools, Berlin, Germany) [137, 138], slice thickness of 4 mm [99], slice gap of 2 mm, spatial resolution (1.4x1.4x4) mm^3. Image acquisition was confined to a single slice per end expiratory breath-hold. Parallel imaging was performed for short-axis views using GRAPPA (32 calibration lines) [45, 68] with reduction factors R_p=1-4.

For SNR/CNR assessment, basal, midventricular and apical short-axis views were scaled in SNR units [64, 67]. For this purpose the 2D CINE FLASH technique included a preliminary noise sequence to measure the noise-correlation matrix. Standardized segmentation of the heart [139] was applied to the end-systolic and end-diastolic cardiac phases using commercial software (QMass MR, Medis Medical Imaging Systems, Leiden, Netherlands). The results are surveyed in Figure 29, here a signal drop from the septum towards the lateral wall is visible for all RF coils, which is an indicator for B_1^+ inhomogeneity. Quantitatively a higher mean SNR could be found in the septum (segments 1-2 of the American Heart Association convention [139]) using an 8-channel and 16-channel array versus the 4-channel RF coil. For comparison, the SNR of the lateral wall provided similar values for each RF coil array. An additional image quality assessment (blood/myocardium contrast, epicardial and endocardial border sharpness, visualization of subtle anatomical features of the heart such as ventricular trabeculae) based on scores given in a blinded consensus reading by two experienced CMR readers (>3000 CMR examinations) was performed [99]. Image quality scoring revealed that all data sets derived from the 8- and 16-channel RF coils were found to be diagnostic. One dataset acquired with the 4-channel array was rated to be nondiagnostic, due to insufficient blood/myocardium contrast in one apical short-axis view. As can be seen in Figure 30, the 16-channel RF coil produced the best image quality, which was significantly improved versus the 8-channel RF coil (p-values: end-diastole: $p = 0.01$, end-systole: $p = 0.05$) and versus the 4-channel RF coil (P-values: end-diastole: $p = 0.04$, end-systole: $p < 0.01$). The data was analyzed using a Wilcoxon signed rank test and a P-value of $p < 0.05$ was regarded as significant.

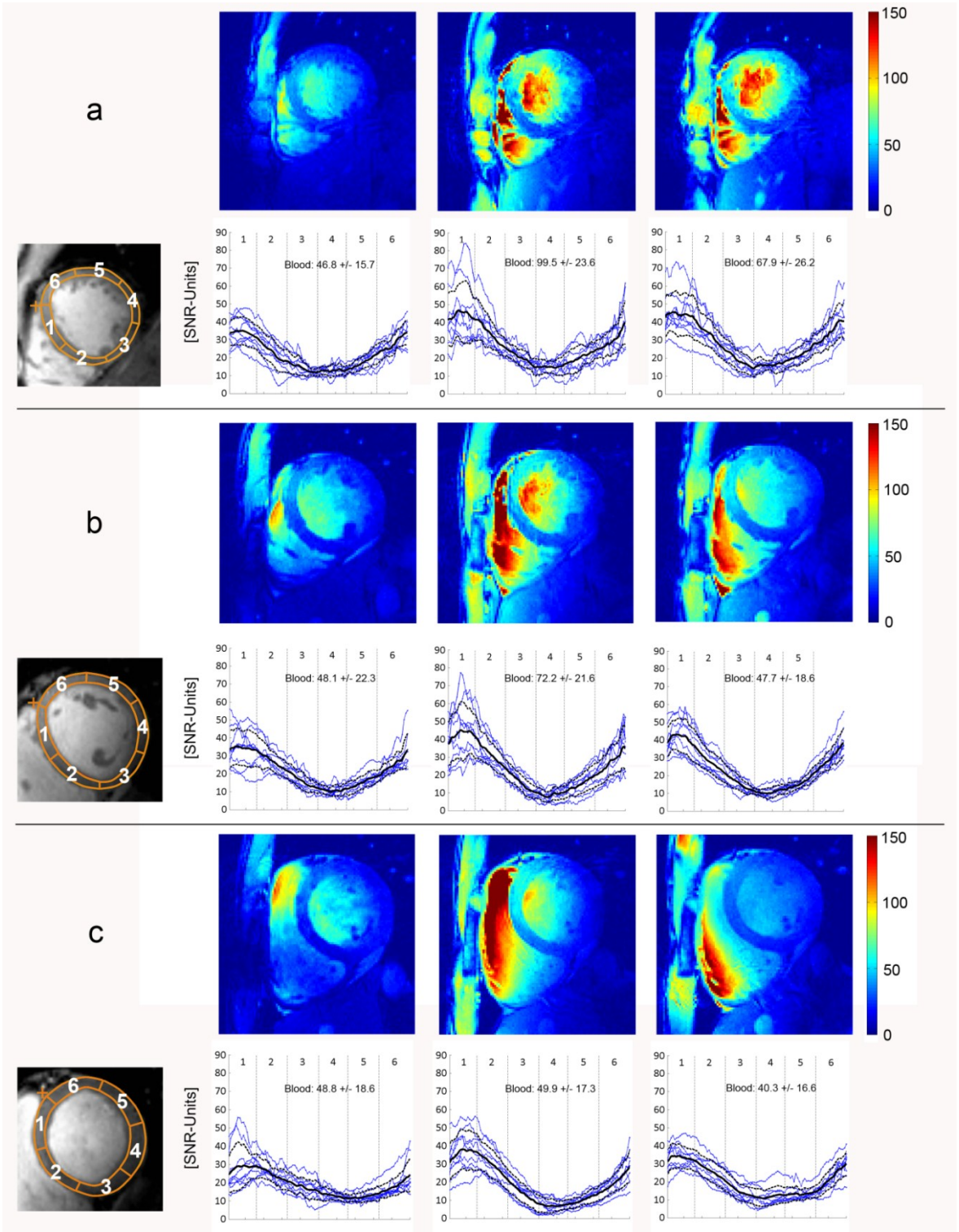

Figure 29: Quantitative SNR maps (parallel imaging acceleration of R_p=2 was used) of short axis views of the human heart and mean SNR value graphs observed at end-diastole for the 4-channel RF coil (left), 8-channel RF coil (middle) and 16-channel RF coil (right) for a) an apical short-axis view, b) a midventricular short-axis view, and c) a basal short-axis view of the heart. The blue lines indicate the SNR distribution across the six segments (defined by the AHA convention) of the myocardium for all subjects. The black line represents the mean SNR value over all subjects. Mean and standard deviation of SNR of the left ventricular blood pool are annotated in the graphs of all three slice positions [57].

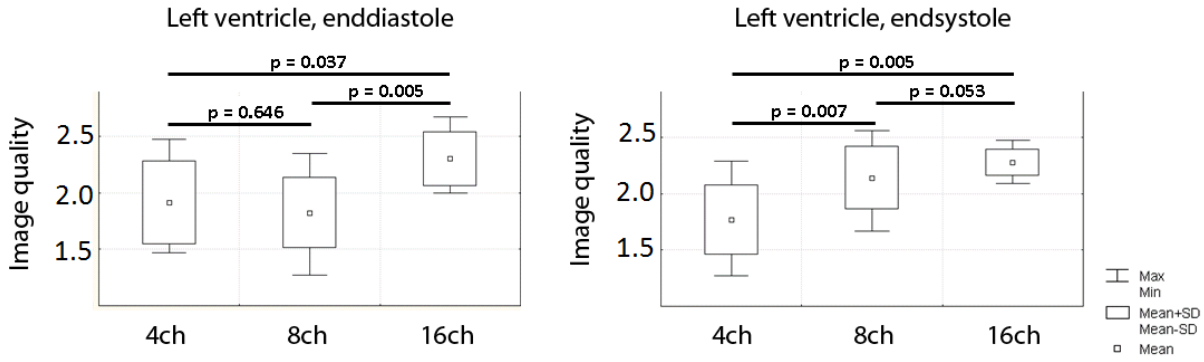

Figure 30: Left ventricular image quality scores derived from a blinded consensus reading including two experienced clinicians. For image quality scoring, a scale [99] ranging from 0 to 3 (0=nondiagnostic; 1=impaired image quality that lead to misdiagnosis; 2=good; 3=excellent) was used [57]. The 16-channel RF coil shows improved image quality in endsystole and enddiastole as compared to the 4- and 8-channel RF coils, with lower standard deviations.

The overall image quality rating was 2.3 ± 0.4 / 2.28 ± 0.12 (end-diastolic/end-systolic) for the 16-channel RF coil, 1.82 ± 0.31 / 2.14 ± 0.28 for the 8-channel RF coil and 1.91 ± 0.37 / 1.77 ± 0.31 for the 4-channel RF coil (Figure 30). For LV cardiac chamber quantification, end-diastolic and end-systolic volume (EDV, ESV), LV ejection fraction (EF) and left ventricular mass (LVM) were obtained by manually contouring the endocardial and epicardial borders in end-diastole and end-systole (CMR42®, Circle Cardiovascular Imaging, Calgary, Canada) using images derived from two-fold accelerated acquisitions. The results of a t-test are surveyed in Figure 31 in Bland-Altman plots.

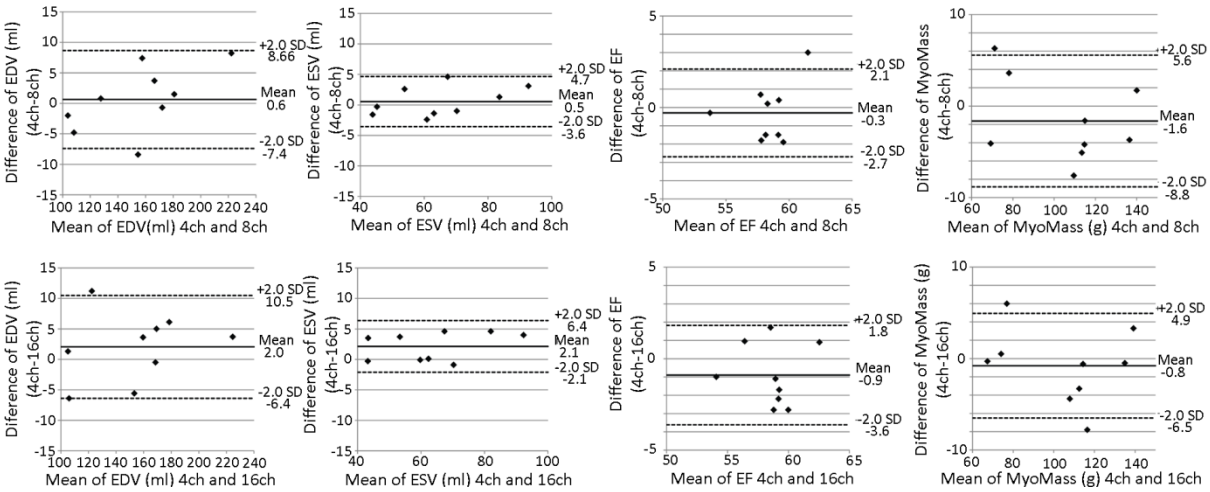

Figure 31: Bland-Altman plots of the results derived from cardiac chamber quantification including EDV, ESV, EF and LVM evaluations. The 4-channel RF coil was used as a reference [57].

Here, no significant difference was found for EF/LVM (1) between the 8-channel (p = 0.59 / P = 0.31) and 16-channel (p = 0.15 / P = 0.58) versus the 4-channel RF coil and (2) between the 8-channel

(p = 0.16 / P = 0.35) versus the 16-channel RF coil. Parallel imaging performance was evaluated for reduction factors up to $R_p = 4$ using quantitative SNR maps and GRAPPA reconstruction [64, 67]. For this purpose g-factor maps were evaluated for a basal, midventricular and apical short-axis slice of the heart for all subjects. The results are illustrated in Figure 32. For midventricular short-axis views derived from the 16-channel array, mean g-factors of 1.10 ± 0.07 ($R_p = 2$), 1.57 ± 0.24 ($R_p = 3$), and 2.33 ± 0.5 ($R_p = 4$) were obtained. For comparison the 8-channel RF coil showed mean g-factors of 1.19 ± 0.13 ($R_p = 2$), 2.08 ± 0.39 ($R_p = 3$), and 3.41 ± 0.35 ($R_p = 4$). The 4-channel RF coil yielded g-factors of 1.35 ± 0.20 ($R_p = 2$), 2.92 ± 0.79 ($R_p = 3$), and 3.85 ± 0.85 ($R_p = 4$).

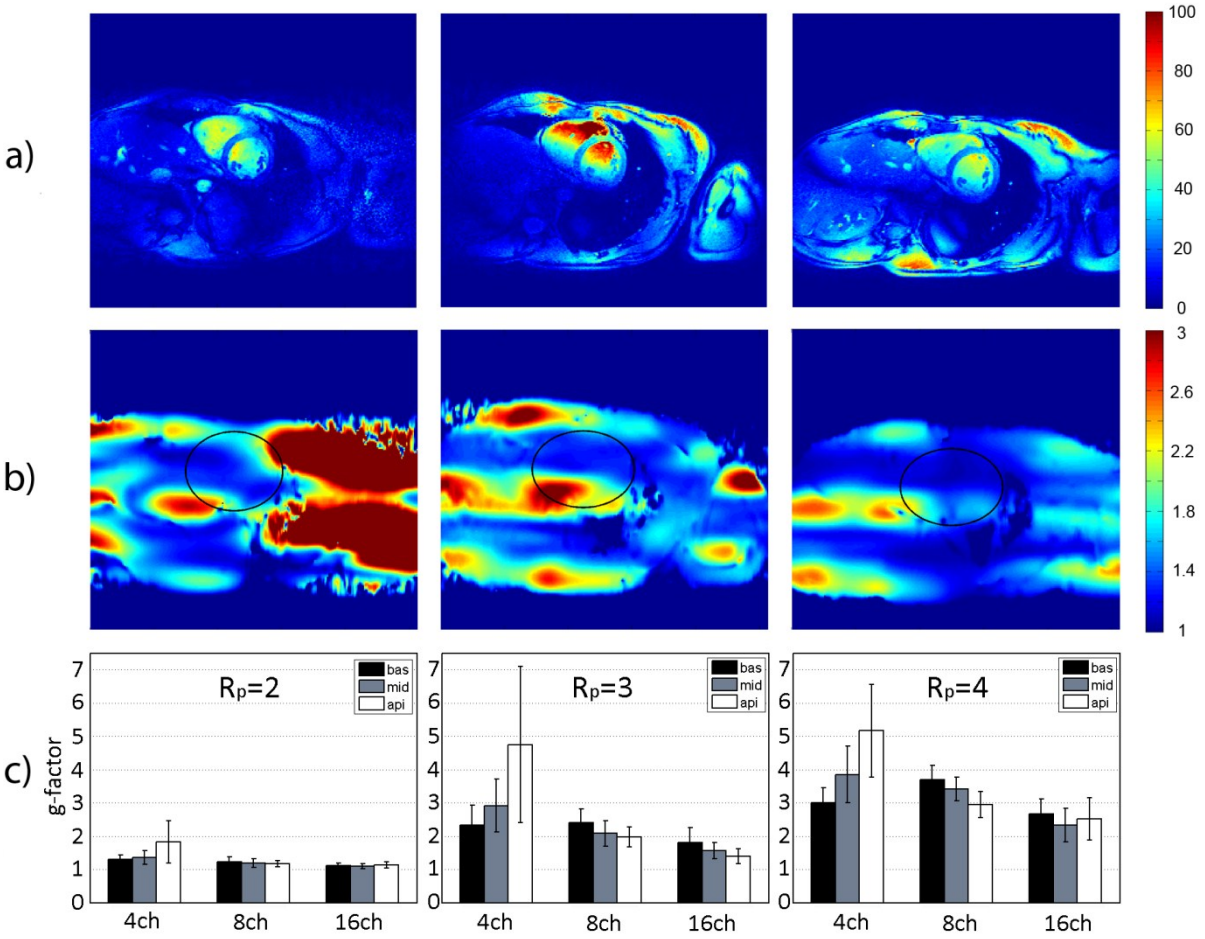

Figure 32: Survey of the parallel imaging performance of the 4-channel, 8-channel and 16-channel TX/RX RF coil. a) Quantitative SNR maps observed for GRAPPA reconstruction using a reduction factor $R_p = 4$ for the 4-channel (left), the 8-channel (middle) and the 16-channel (right) RF coil. b) g-factor maps derived from GRAPPA reconstruction for a reduction factor of $R_p = 4$ for the 4-channel (left), the 8-channel (middle) and the 16-channel (right) RF coil with a ROI indicating the position of the heart. c) Comparison of g-factor (mean ± SD) for the 4-, 8-, and 16-channel RF coils for basal (bas), midventricular (mid) and apical (api) short-axis views and reduction factors R_p = 2-4 [57].

Noise amplification due to the use of parallel imaging decreases as the number of TX/RX channels increases. The 16-channel TX/RX showed less parallel imaging-induced noise amplification than the 8-channel and the 4-channel TX/RX RF coils. The noise amplification performance of the 4-channel TX/RX RF coil renders it unsuitable for reduction factors larger than $R_p = 2$.

The *in vivo* application and evaluation of the three RF loop coil arrays revealed that a larger number of loop elements in conjunction with a two-dimensional array design can improve image quality as well as parallel imaging performance for CMR at 7.0 T. The proposed RF coil designs were suitable to acquire diagnostic image quality with no extra scan time penalties due to dynamic RF shim settings or RF coil adjustments demonstrating applicability. Our findings suggest further development of an even higher number of two-dimensional transceiver channels. To this end we further increased the number of transmit/receive channels to 32 in a two dimensional building block design to push the limits of SNR and parallel imaging performance [95].

4.6 Two Dimensional 32-Channel Transceiver Array Configuration

The 32-channel transceiver array customized for cardiac MR at 7.0 T is in a class of its own since it is the 1st one in the world. This array was implemented, as depicted in Figure 33a, with a building block design of 8x4 elements. Such setup enables a close fit of the eight building blocks to the human body affording stable loading conditions of the array of -21 ± 7 dB averaged over eight volunteers (five male; body mass index (BMI) = 23 ±2 kg/m²). Each loop has a rectangular size of (6x6) cm², resulting in a left-right and head-feet coverage of (35 x 29) cm² and a 4x4 matrix for the anterior as well as posterior part. A two dimensional arrangement of the building blocks facilitates parallel imaging along oblique imaging planes, which is beneficial for clinical investigations of the long and short axis views of the heart. Decoupling of adjacent elements was performed by common decoupling capacitors as already suggested for the 16-channel array [94], whereas all other elements were decoupled by a distance yielding decoupling values below -10 dB for all elements and volunteers, while the noise correlation was found to be below 0.46. RF shimming was based on EMF simulations of the 4-chamber view of the heart, while a Levenberg-Marquardt algorithm optimized the phase contributions to minimize the cost function for B_1^+ homogeneity [140, 141]. The resulting phase settings (Ch1=0°, Ch2=-10°, Ch3=-24°, Ch4=-54°, Ch5=-48°, Ch6=-351°, Ch7=-347°, Ch8=-308°, Ch9=-225°, Ch10=-12°, Ch11=-344°, Ch12=-300°, Ch13=22°, Ch14=-351°, Ch15=-350°, Ch16=-14°, Ch17=-62°, Ch18=-192°, Ch19=-214°, Ch20=-21°, Ch21=-109°, Ch22=-127°, Ch23=-315°, Ch24=-27°, Ch25=-40°, Ch26=-154°, Ch27=-98°, Ch28=-186°, Ch29=-185°, Ch30=-94°, Ch31=-314°, Ch32=-105°) were realized with phase shifting cables incorporated into a three stage power splitting cascade.

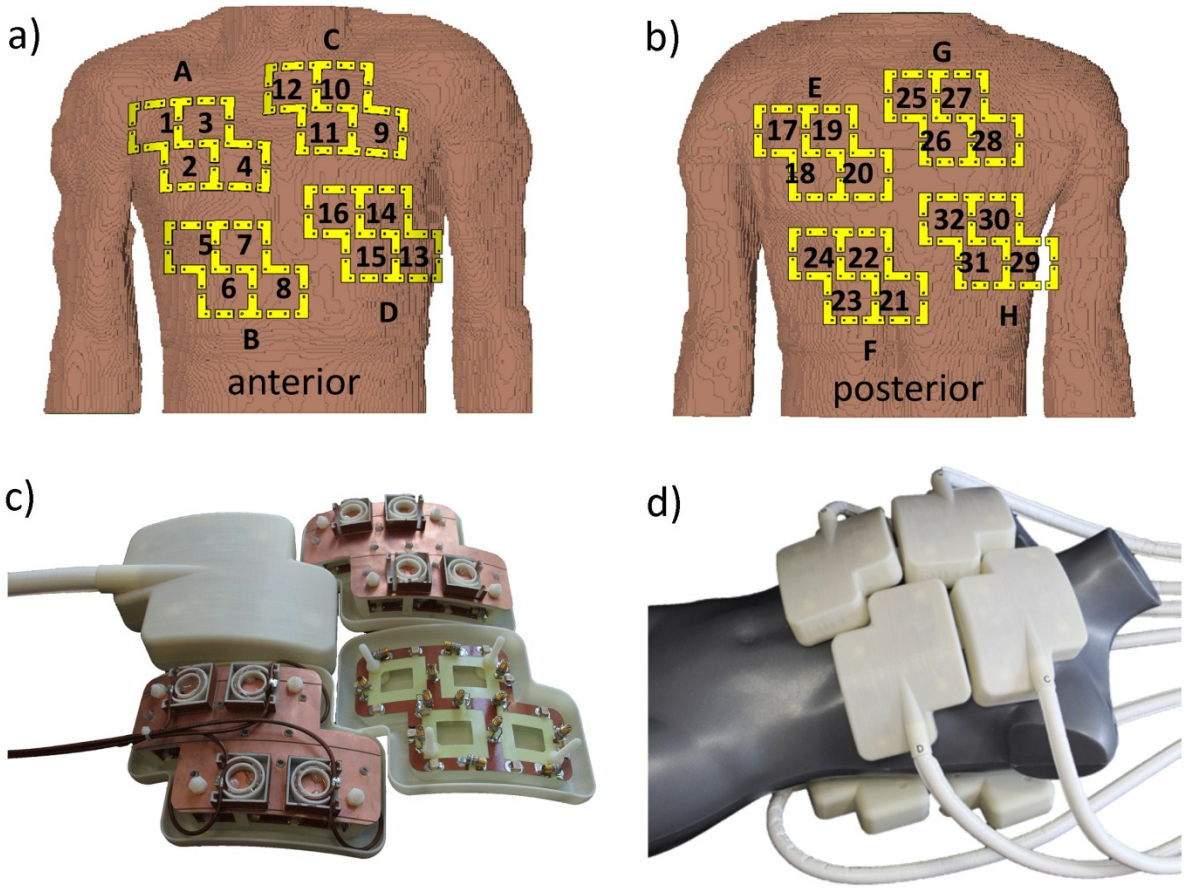

Figure 33: (a-b) Schematic representation of the anterior and posterior RF coil channels of the 32-channel transceiver array. (c) Picture photograph of various construction stages of the individual building blocks with the conductor path, fixed and variable capacitors, RF shield, cable traps and ABS casing. (d) Placement of the cardiac array on a mannequin representing human body geometry [95].

First stage: One 1:2 Wilkinson power splitter, Second stage: Two 1:4 Wilkinson power splitters and Third stage: Eight 1:4 Wilkinson power splitters. The high density transceiver element array allows for high acceleration factors for parallel imaging along multiple directions as illustrated in Figure 34. For reduction factors of up to $R_p = 5$ the mean g-factor in the region of the heart remained below 2 for the two-chamber and short axis view, which affords a clinically acceptable image quality even for this degree of acceleration.

To summarize, the expertise, know-how gathered and lessons learned during the design, evaluation and application of the many-channel transceiver arrays tailored for cardiac MR at 7.0 T provided the best foundation for entering into the development of RF antennas customized for simultaneous RF hyperthermia and MR imaging.

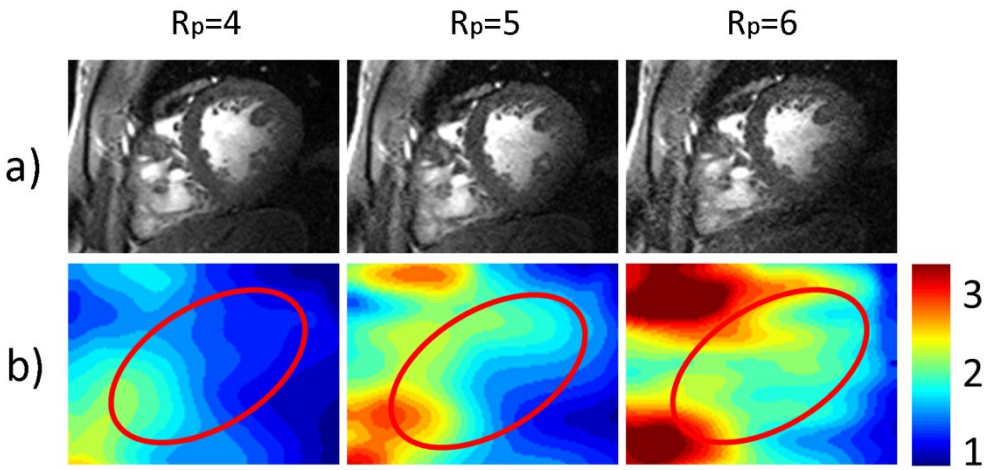

Figure 34: GRAPPA-reconstructed short axis (a) view of the heart with associated g-factor maps (b) for one dimensional parallel imaging reduction factors of R_p = 4-6 derived from 2D FLASH CINE imaging. The position of the heart is indicated by the red circular ROI [95].

5. RF Antennas for Simultaneous RF Hyperthermia and MRI

Previous approaches to combine MR RF coils and hyperthermic applicators are mainly constrained to whole-body (with a primarily focus on the liver/abdomen) or surface hyperthermia [142, 143]. This chapter outlines the electromagnetic requirements for MR imaging and RF heating applications with the goal to develop an RF coil design that combines both domains in an integrated device. To meet this goal a novel hybrid eight channel RF applicator is presented, which is capable of being utilized for targeted RF hyperthermia and MR imaging in the human brain at 7.0 T and higher.

Fractions of the content presented in this chapter are published in [65].

5.1 Biological Rationale of RF Hyperthermia

Radio frequency induced heating has been presented as one of the major drawbacks of magnetic resonance imaging so far. To prevent harm to healthy tissue, power deposition limits have to be set in order to comply with the current safety guidelines [91]. However RF induced heating can also have beneficial roles in medicine; when properly controlled, RF hyperthermia (40-47°C) can be implemented in some clinical applications. Throughout this chapter, the clinical benefits of RF induced thermal therapies are presented and the appealing use of MR RF system hardware for combined MR imaging and targeted RF hyperthermia is investigated.

5.1.1 Thermal Dose and Cell Death

When tissue undergoes temperature increase due to a given thermal dose, three basic parameters critically determine the biological outcome:

1) Applied temperature
2) Duration of the applied temperature
3) Tissue type

Fever is defined as a core body temperature higher than 38.3°C. It induces various physiological changes, including increased tissue metabolism and blood flow to accelerate tissue repair [144, 145]. These physiological effects are considered to be well tolerated below a temperature of ~39°C and do not pose threats on the integrity of tissue on the short term [146]. A cytotoxic effect is induced by a combination of a high temperature dose ($T > 39°C$) and exposure time to this temperature [147]. A thermal dose that defines this cytotoxic effect can be expressed in cumulative equivalent number of

minutes at 43°C ($CEM_{43}°C$), introduced by Sapareto and Dewey [148] and updated by Yarmolenko et al. [112]:

$$CEM_{43}°C = \sum_{i=1}^{n} \mathrm{t_i} \cdot R_c^{\,(43-T_i)} \tag{58}$$

with t_i being the i-th time interval, T_i the average temperature during the i-th time interval and an empirical factor R_C corresponding to the temperature dependence of the rate of cell death in a given tissue:

$$R_c = \begin{cases} 0 & T < 39°C \\ 0.25 & 39 < T < 43°C \\ 0.5 & T > 43°C \end{cases} \tag{59}$$

The concept of $CEM_{43}°C$, was originally introduced in studies evaluating clinical hyperthermia as cancer therapy [112, 148], but recently it has also been suggested as a possible parameter to determine safe RF exposure limits for diagnostic MR imaging applications [113, 114]. Employing a thermal dose to biological tissue in the human body triggers a complex cascade of physiological reactions, both on a cellular as well as biochemical level. Thermal dosing is a major ongoing research topic and in the following section, the impact of hyperthermia on the cell cycle and the immune system as well as its implications for the tumor microenvironment will be described.

Temperature changes above 48°C invoke severe protein denaturation leading to largely irreversible changes and predominantly necrotic cell death [149, 150]. In contrast, RF hyperthermia operates in the temperature range of 39-47°C that causes protein unfolding, a reversible process that can be modulated by molecular chaperones like the heat shock protein (HSP) HSP70 [151]. Temperatures above 43°C result in a time-dependent exponential increase in cell death, while hyperthermia up to 43°C induces thermal tolerance that results in a plateau in clonogenic survival [147, 149, 152]. The thermal energy that is needed to reach exponential cell death, is in the energy range needed for protein denaturation (~140 kcal/mol), suggesting that intracellular and membrane proteins are the main targets for cell death [147, 153]. Cells in the DNA replication/synthesis phase (S-phase) are hypersensitive to hyperthermia [147]. Hyperthermia induces cell death as a result of chromosome aberrations; accumulation of cells in the S-phase induces mechanisms that prohibit transition of cells into the mitosis (M) -phase to undergo cell division [149, 154]. Especially within the nuclear matrix heat shock induced aberrant protein binding might alter nuclear functionality and disturb the cell cycle prior to, during and after DNA replication (corresponding to G1, S, G2 phases), which leads to abrogation of the G2-M cell cycle checkpoint [149, 155, 156]. These effects within the nucleus that

prohibit cell cycling are not independent of other cellular effects. Heat stress also modifies plasma membrane permeability leading to Ca++ inflow and invokes a redox status change by disruption of the membrane potential of mitochondria [149, 157, 158].

Tumor hyperthermia holds the promise for cancer therapy, where a given thermal dose is applied to eradicate tumorous tissue. Apart from the direct cytotoxic effect on cell or tissue, hyperthermia can precipitate other indirect beneficial effects. At much lower thermal doses (39-42°C, 1-2h) favorable immunological and physiological reactions are brought about that can be exploited in cancer treatment strategies [159]. Malignant tumors have a specific microenvironment, distinguishing them from healthy tissue. In particular a chaotic vasculature leads to regions of hypoxia, acidosis or stasis within tumorous tissue [160]. These areas in solid tumors of a characteristic low perfusion render decreased heat sink capabilities and consequently an increased sensitivity to cell death based on temperature exposures [161]. Fever-range hyperthermia may evoke immunological mechanisms with potential antitumor effects. Under elevated temperatures tumor cells express higher levels of HSP [162]; release of HSPs boosts the immune response by maturing dendritic cells (DCs) and activating natural killer (NK) cells [163]. Following uptake of these HSPs by antigen presenting cells such as DCs, MHC class II molecule expression is enhanced and recognition of antigen (e.g. tumor antigen) by these cells is facilitated [163, 164]. Tumor cells own unique proteins (tumor antigens) which can be employed as bait for a specific immune response against the tumor [165]. Advantage can be taken from the priming of the immune system by HSPs; tumor HSP expression, together with application of local hyperthermia at tumor location can be implemented as a strategy for personalized cancer therapy to directly target the tumor as well as trigger the immune system (via release of HSPs) to eradicate any residual left of tumorous tissue [156, 163]. Whole body hyperthermia in the fever-range has also been shown to improve migration of epidermal DCs to the draining lymph nodes [166], enhance cross-priming of lymphocytes [163] as well as an increase infiltration of NK-cells at tumor site [163, 167].

5.1.2 Multimodal Cancer Therapy – Hyperthermia, Radiation Therapy and Chemotherapy

Hyperthermia can be utilized as an adjuvant therapy along standard cancer therapies such as radiotherapy and/or chemotherapy in the treatment of various cancers [9]. Radiation therapy is a medical treatment that targets tumors with electromagnetic radiation in the wavelength regime below 10 nm (X-rays). These high energy particles are absorbed in biological tissue and lead to cell death predominantly by direct DNA double strand breaks (DSB) or indirect DSBs by the creation of free radicals [168]. Oxygen (O_2) plays a crucial role to increase radiosensitization [169, 170] and diffusion or perfusion limited hypoxic regions of a tumor microenvironment lead to a relative

resistance (factor 2-3) to ionizing radiation [169]. Here, hyperthermia is able to increase vascularization and vessel permeability, leading to enhanced oxygen pressure levels in the hypoxic regions and to improved radiosensitivity [161]. On the other end, S-phase cells, which show a relative radioresistance, are sensitive to heat which enhances the synergistic effect of radiotherapy plus hyperthermia [147, 153].

Another strategy in current cancer treatment is the use of cytotoxic chemotherapeutic agents, like alkylating agents, platinum compounds, topoisomerase inhibitors or antimetabolites, which invoke cell death by preceding DNA damage [161]. Adjuvant hyperthermia has been shown to increase the cytotoxic effect of many of these drugs in vitro and *in vivo* [171, 172]. A linear temperature dependent enhancement in their cytotoxicity was observed for most of the alkylating agents, platinum drugs and nitrosources [171, 172]. This may be a result of an increased alkylation, improved drug uptake by means of enhanced vessel permeability and inhibited drug induced damage repair [156, 161, 172]. Specifically in characteristic hypoxic regions a temperature induced increased permeability of the vasculature might be advantageous [160, 173]. Other synergistic effects of hyperthermia administered together with chemotherapy are based on an increased blood flow at elevated temperatures [174].

5.1.3 Targeted Drug Delivery

The administration of chemotherapy is accompanied by several detrimental side effects. Undesired complications include decreased blood cell counts, hair loss, nausea, leukopenia, mucositis, impaired fertility up to organ damage and central nervous system toxicity to name a few [175]. The reason for these side effects is that anticancer pharmacological agents are commonly poorly selective with respect to their cellular target and may induce cytotoxic effects both on tumor cells and normal cells. To reduce the harmful adverse reactions of chemotherapeutic agents towards non-cancerous tissue and/or to increase the fraction of delivered drugs to the tumor, targeted drug delivery systems are being investigated [176, 177]. While triggering of drug release at the tumor site by internal factors that are specific to the tumor microenvironment (e.g. pH or distinct enzymes), external triggering with physical stimuli such as electromagnetic fields, ultrasound or temperature may be more target-based for drug delivery and perhaps more effective at boosting the anticancer drug activity [176, 178]. Controlled RF hyperthermia is a promising approach for selective drug delivery. Release of anti-cancer pharmacological compounds from macromolecular drug carriers composed of thermally responsive polymers can be controlled by RF induced hyperthermia; these thermally-controlled drug carriers show high accumulations in tumors, low system toxicity and high plasma half-life [179]. Other drug carriers are liposomes, which consist of a phospholipid bilayer and an aqueous core containing

the therapeutic drug [178, 180]. The permeability of the phospholipid bilayer can be altered with an increase in temperature, so that these so-called temperature sensitive liposomes (TSL) release its encapsulated drug content at defined thermic conditions [181, 182]. TSLs can be engineered for triggered drug release within the RF hyperthermia range of 39-47°C [183-185]. The attractive features of thermo-sensitive drug carriers are not only limited to therapeutic use. TSLs can be combined with MR imaging contrasts such as gadolinium chelates to provide valuable diagnostic information at a targeted location [186, 187]. Multiple contrasts that exploit X-nuclei like ^{19}F MR and chemical exchange saturation transfer (CEST) are an attractive solution to follow these drug carriers and to monitor and quantify the drug release into the tumor environment [188].

5.2 Clinical Studies

Hyperthermia has been successfully applied in clinical studies [1, 7, 9, 189]. In combination with other treatment modalities such as radiotherapy and chemotherapy the clinical value of RF hyperthermia was examined in clinical randomized trials [9, 189, 190]. The treatment efficacy of radiotherapy has been significantly improved for recurrent or metastatic malignant melanoma [2], metastatic lymph nodes of head and neck tumors [3, 4], superficially localized breast cancer [5, 6], pelvic tumors [7] and glioblastoma multiforme [8]. The use of chemotherapy applied together with a hyperthermic treatment showed positive outcome for localized high risk soft tissue sarcoma [1], bladder cancer [191] and colorectal cancer [192, 193].

5.3 RF Hyperthermia Systems Hardware

To generate a temperature increase inside the human body at a defined location, multi-channel radiofrequency heating systems have been used [9, 194]. Unlike interstitial heating devices this approach of reaching the target region is non-invasive since only the electromagnetic waves penetrate the body/tissue and not the heating device. Moreover the electromagnetic field vector superposition in the human tissue may be altered by changing the RF pulse shape of each individual element [13, 195]. Various antenna designs have been evaluated to radiate RF energy into the human body including waveguide radiators [196, 197], microstrip arrays [198], patch antennas [199], wide band antennas [200] or dipole antennas [201-205]. The frequency used is typically around 100 MHz for clinical applications in the abdomen and liver [9]. For head and neck regions the use of even higher RF frequencies was reported [194, 200]. Technological limitations of state-of-the-art clinical RF hyperthermia systems are RF power constraints which limit the desired thermal dose at the target

location (<43°C) and temperature inhomogeneity in the desired three dimensional target structure [159, 161]. Other challenges include: coupling between antennas, inefficient coupling of the antennas to the human body, antenna sensitivity to modifications of the matching conditions either by movement or temperature dependent permittivity/conductivity changes, insufficient temperature monitoring systems, excessive thermal doses in healthy tissue, inability to react to transient thermal conditions in the human body, incapability or ineffectiveness of controlled temperature hotspot steering capabilities, patient discomfort and system costs.

5.4 Combining RF Hyperthermia and MR Imaging

To address many of the before mentioned challenges, in this work a concept was developed to use high permittivity dielectrics for efficient coupling to the body, efficient decoupling between the antennas and steady matching conditions. Operating these elements with pulsed power amplifiers of UHF MR systems, sufficient energy can be deposited at a targeted location, the energy deposition is more spatially selective due to an increase in frequency, MRTh allows fast high temporal- and spatial resolution for control and adaptation of the RF power deposition via readily available multi-channel transmit systems, additional diagnostic information (e.g. tumor perfusion changes) can be acquired using the SNR advantages of these elements for MRI and no additional RF hardware (e.g. RF power amplifiers) are needed which decreases cost and complexity.

In particular accurate 2D/3D temperature monitoring is a prerequisite to obtain the actual generated temperature distributions which is mandatory to evaluate the treatment outcome and the efficiency of any RF hyperthermia system appropriately. Notwithstanding that numerical electromagnetic and temperature simulations provide a valuable tool for realistic energy profile estimations [65, 206], an RF pulse adaption may further increase the efficiency of the desired thermal dose in malignant tissue, while protecting healthy tissue from thermal damage [12]. Here MRI plays a key role for many thermal therapies including an ever growing number of applications/indications [207, 208]. Consequently first implementations combined (i) RF hyperthermia hardware for therapy with (ii) anatomical/diagnostic MR imaging for spatiotemporal treatment planning and with (iii) MR thermometry for treatment monitoring [10, 11, 201], as illustrated in Figure 35.

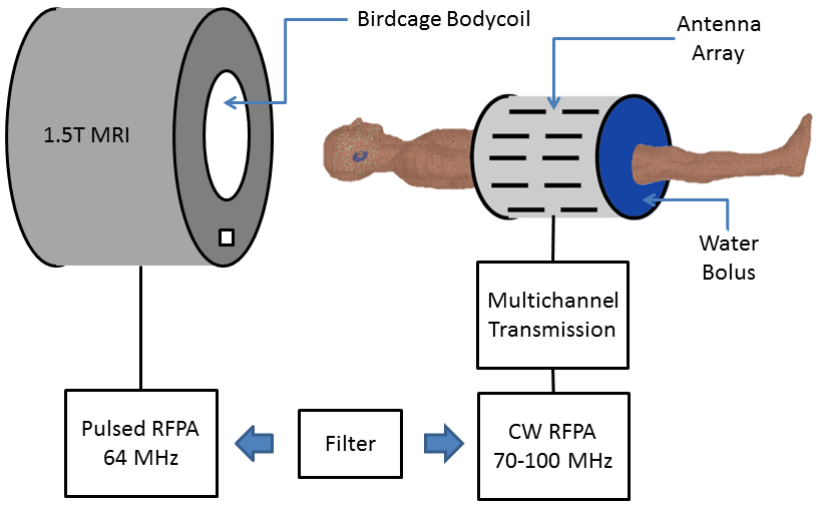

Figure 35: Schematic representation of a clinical RF hyperthermia system with an antenna array positioned around the body usually driven with a frequency of 70-100 MHz and a continuous wave (CW) power amplifier. A water bolus is positioned around the body of the patient, which is connected to a cooling control circuit to reduce surface temperature elevations in the human body. Additional hardware filters (e.g. notch filters) are used and integrated on both the MR and the RF hyperthermia system to reduce interferences in a dual frequency operational mode (64 MHz for MRI and typically 100 MHz for RF hyperthermia).

While the RF coils used for MR imaging are commonly operated at a frequency of 64 MHz (1.5 T), RF transmission induced heating interventions are achieved with an applicator commonly driven at a frequency of 70-100 MHz [209]. Current clinical implementations require extra hardware retrofitted into the MR suite – notably antennas, amplifiers and frequency filters – which have the trait of driving costs, limiting patient comfort and ease of use and which bear the potential to induce imaging artifacts [14].

5.5 Benefits and Challenges of Higher Radio Frequencies

A limitation of current MR guided RF hyperthermia therapies is the RF wavelength used for RF hyperthermia. Based on Equation (53) at 1.5 T the ^{1}H spin excitation frequency of 64 MHz results in λ_t of approximately 40 cm in muscle tissue. An RF frequency of f = 100 MHz, which is commonly used for hyperthermic treatment, results in λ_t of approximately 30 cm while at 3.0 T (f = 128 MHz) λ_t is approximately 24 cm. These wavelengths are relatively long compared to the geometry of a human torso let alone the geometry of the human brain. This constraint limits the spectrum of interventions and therapies using MR guided RF hyperthermia [1] and asks for innovation. Head and neck RF hyperthermia applicators make use of higher RF frequencies (434 MHz) already [194, 204]. Other approaches use wideband antenna designs to utilize various accessible RF wavelength to reach a

desired heating pattern for variable tumor sizes, while at higher frequencies hotspot dimensions are reduced [200]. An increase in RF frequency may thus potentially increase RF hyperthermia treatment efficiency and tumor selectivity. Both systems however, rely strongly on *a priori* calculations, lacking a real-time control via 3D temperature measurements (e.g. MR thermometry) [194, 210, 211]. Here the combination of high frequency hyperthermia at UHF MR frequencies hold the promise to connect the domains of localized RF power distribution and MR thermometry controlled dynamic thermal dose adaptation, with the ultimate goal to increase overall treatment efficiency.

5.6 Single Frequency RF Hyperthermia and MR Imaging

The advantages of using MRI capable and MR compatible antennas for targeted RF heating are multi-faceted. First it reduces costs and complexity, as only one antenna array and a single power amplifier is needed for therapeutic and diagnostic purposes. Most importantly the MR imaging capabilities can be exploited to the fullest. Local transmit RF coils provide MR imaging advantages over volume resonators used in current clinical RF hyperthermia treatment [9]. Higher SNR, reduction of image acquisition time and increased transmit power efficiency can boost spatial and temporal resolution of MR thermometry [44-46, 212]. UHF MRI ($B_0 \geq 7.0$ T) shows an additional intrinsic SNR gain based on an increase in magnetic field strength that potentially further enhances the aforementioned MRTh spatial and temporal accuracy [31]. For the application of targeted RF heating, effective wavelengths of approximately 13 cm at 7.0 T (298 MHz) or as small as approximately 6 cm at 14.0 T (600 MHz), hold the promise to further reduce the size of the generated temperature hotspot. Admittedly, the wavelength shortening at UHF constitutes a major challenge for imaging due to highly complex interference patterns and non-uniform RF transmission field (B_1^+) distributions [102]. This challenge can be addressed by using B_1^+ shimming techniques and multi-channel transmit RF technology [57, 85, 106]. Multi-channel transmit technology (8-16channel) is becoming readily available for UHF MR systems, enabling the use of dynamic B_1^+ shimming techniques by feeding individual pulse shapes to each channel [213, 214]. Realizing the opportunities together with the limitations of current MR guided RF heating procedures this work focuses on the synergy of diagnostic MR imaging, MR thermometry and targeted RF heating in a single device at ultrahigh fields.

5.7 Targeted RF Heating Considerations

To investigate the targeted RF heating and MR imaging capabilities of various antenna designs at discrete MR frequencies, EMF simulations were performed. Based on electro-dynamic conditioning a

pre-selection of possible single feeding RF channel design criteria was made before multichannel RF arrays were investigated over a wide frequency range (f = 64-600 MHz). Main focus was set to the targeted RF heating capabilities while maintaining sufficiently high B_1^+ transmit efficiency.

The presented cardiac RF coil designs using loop structures provided decent MR imaging performance in terms of image quality [57]. For the purpose of targeted RF heating, however, such designs are suboptimal. The E-field vector (Figure 23 & Figure 36a) follows the conductive path of the copper, changing its orientation spatially at a single time point by 360°. The spatial distribution of the E-field has the advantage of reduced surface SAR values while maintaining high H-field components at the center of the RF coil and the surface. To focus the energy or power absorption towards the center of the object, a constructive interference of multiple E-field vectors by means of multiple channels is required, [195]. For this purpose the E-field distribution of a RF loop coil is disadvantageous, as the E-field vector of a single loop (Figure 36a-b) at depth is oriented in opposite directions. A controlled E-field focusing while using multiple RF loop coils in a heterogeneous medium is consequently challenging if not elusive.

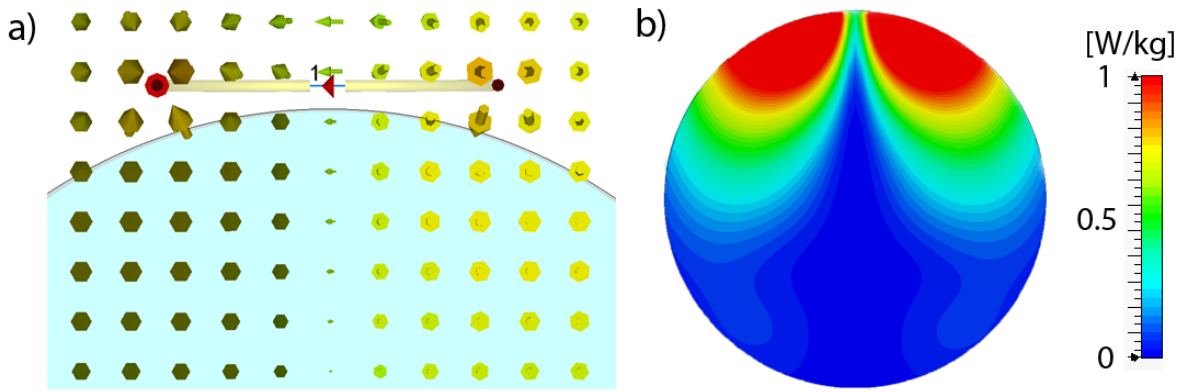

Figure 36: (a) Axial view (xy) of the E-field distribution (logarithmic scale) of a RF loop coil inside the phantom. (b) Point SAR distribution in an axial view (xy) of a RF loop coil inside the phantom for 1W input power.

The stripline element [106] shows a more favorable E-field distribution (Figure 23) with the E-field vector in parallel to the main magnetic field B_0. However this design shows some coupling and surface waves between the individual channels leading to a low transmit energy efficiency. To improve decoupling and focus RF energy into the object, electrically conductive walls between each element were installed in parallel to the electric field component, Figure 37. To improve energy coupling to the object a low loss high permittivity dielectric (ε = 80) was used, which in practice can be realized with deionized water, D_20 or ceramics. Transmit efficiency and SAR distribution before and after the modifications are displayed in Figure 37. With these modifications in place, the H- and E-

field shows improved depth penetration, which not only suits targeted RF heating but also increases B_1^+ for MR imaging applications (Figure 37). The RF heating efficiency:

$$RF\ heating\ efficiency = \frac{\max(SAR_{center})}{\max(SAR_{surface})} \tag{60}$$

with the SAR distribution found in the targeted central region SAR_{center} and the surface region $SAR_{surface}$ of the phantom, increases for an 8-channel modified stripline array by >70%, rendering this design suitable for targeted RF heating applications.

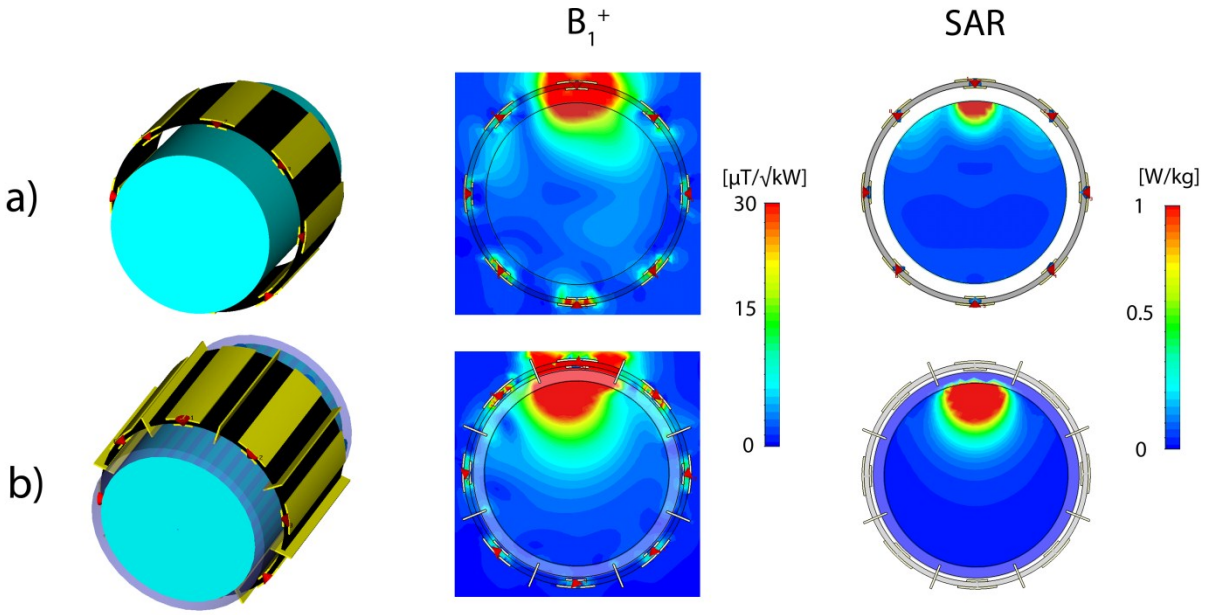

Figure 37: Comparison of the B_1^+ profile and SAR of a single element of a (a) 8-channel stripline array based on Adriany et al. [106] and (b) a modified version which includes electrically conductive walls between each element and which was examined in this study [215]. The modified stripline configuration shows significant improvements in transmit efficiency and RF heating efficiency.

The electric dipole is another candidate for targeted RF heating applications since the Poynting vector is perpendicular to the dipole and hence directed towards the target if placed around the head. It offers a deep penetration of the E-field components (Figure 23). Dipole elements were used already successfully at lower frequencies for RF Hyperthermia treatment [202]. To enable efficient power transmission from these elements, the length of the antenna needs to be adjusted to the transmission frequency which at 64MHz can be as long as 2.3m for a λ/2-dipole. In this work we used a combination of a bow tie shaped electric dipole antenna and a high permittivity dielectric as illustrated in Figure 38. The RF feeding port of the antenna is located in the center of the bow tie in between the two conductive triangles, as depicted in red in Figure 38b-c. The bow tie antennas were

immersed in distilled water, which is a low loss dielectric with a high relative permittivity constant of ε≈81 to shorten the effective length of the antennas and to enable efficient energy transfer into the object. This configuration offers significant advantages. In particular a bow tie design has a higher bandwidth versus a traditional a rectangular strip [122, 216], allowing for improved patient-to-patient matching conditions. Using a liquid dielectric as compared to a high permittivity solid ceramic block [122] enables lighter building block elements, which is beneficial for all applications asking for lightweight RF coil design. At the same time a liquid dielectric can be exploited for superficial cooling in targeted RF heating applications. While the electromagnetic properties of the RF antenna are not hampered, detrimental increase of surface temperature can be offset [11].

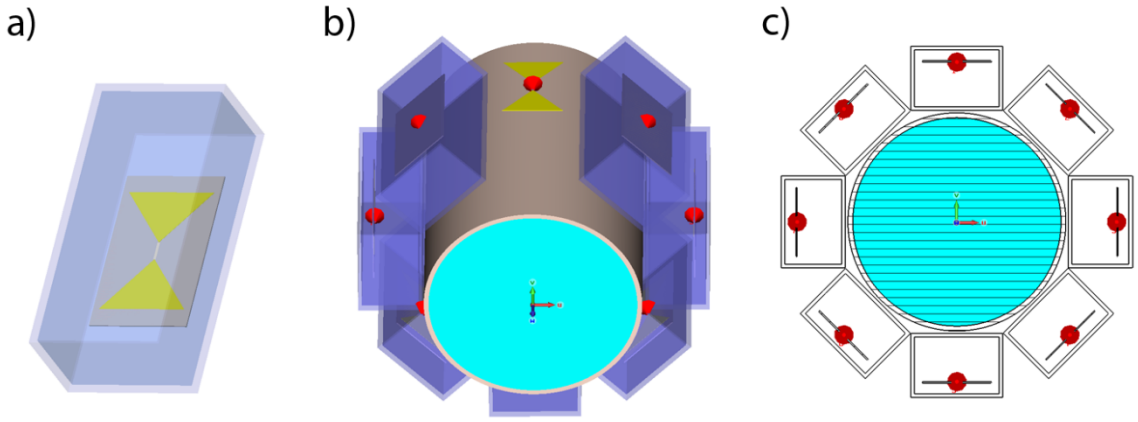

Figure 38: Basic design of the virtual electric dipole antenna configuration used for electromagnetic field simulations. a) Basic design of the proposed bow tie dipole antenna building block used in numerical EMF simulations. b) Eight bow tie dipole antennas placed radially around a cylindrical phantom. c) Transversal view of the virtual phantom setup together with the bow tie dipole antennas [65].

To compare the performance of the suitable preselected antenna designs for targeted RF heating, including the modified stripline and the bow tie dipole antenna, the simulation study integrated a multi-channel setup with a uniform virtual cylindrical phantom (diameter = 172 mm, length = 250mm) with brain tissue properties ($\sigma_1 = 0.657$ S/m, $\varepsilon_1 = 50.5$). For the numerical simulations discrete MR frequencies ($f_1 = 64$ MHz, $f_2 = 128$ MHz, $f_3 = 298$ MHz, $f_4 = 400$ MHz, $f_5 = 500$ MHz, $f_6 = 600$ MHz) were used. Eight antenna elements were positioned equidistantly around the phantom as depicted in Figure 38b-c. Matching and tuning was performed with a match and tune network at the antenna's feeding point calculated in an S-Parameter analysis in RF circuit co-simulations using CST Design Studio (CST GmbH, Darmstadt, Germany) [217]. To create a SAR focus due to constructive interferences of E-fields in the center of the phantom all ports were excited with no phase delay between elements using an accepted input power of $P_{in} = 1$ W at the RF feeding port of each of the eight elements. The effective dimensions of the deep lying hotspots were analyzed

using iso-contour calculations of the SAR distribution. For this purpose iso-SAR 25%, iso-SAR 50%, iso-SAR 75% and iso-SAR 90% thresholds were derived based on the maximum point SAR value. The results of the simulation study obtained for the bow tie antenna are summarized in Figure 39. For comparison the results of the modified stripline array are shown in Figure 40. The determined iso-SAR hotspot dimensions are surveyed in Table 2 for a central transversal slice through the phantom as illustrated in Figure 38c. Table 3 summarizes the surface SAR values found for the modified stripline as well as the bow tie dipole array for all investigated frequencies. At 64MHz a rather uniform SAR distribution over the cylindrical phantom was observed for both antenna designs. At 128 MHz focal regions of SAR increase were found which confirms results obtained for RF hyperthermia frequencies ($f < 140$ MHz) used in a clinical setting [9]. Also, the power deposition inside the phantom per input power (SAR_{center}/P_{in}) increased (Figure 39a) which makes targeted RF heating more efficient. At 7.0 T (298 MHz) the E-field focusing abilities of the dipole antenna array yielded an iso-SAR 50% hotspot with a size of (43 x 43 x 54) mm^3. The SAR hotspot was even further reduced at 14.0 T (600 MHz). Here the iso-SAR 90% contour covered an area as small as (10 x 10 x 37) mm^3 for an axial slice through the center of the long axis of the phantom. In comparison the iso-SAR 75% contour included an area of (17 x 17 x 63) mm^3, while the iso-SAR 50% and iso-SAR 25% areas revealed a size of (26 x 26 x 101) mm^3 and (35 x 35 x145) mm^3 for a central axial slice through the phantom. The modified stripline design revealed an iso-SAR 25% hotspot of (57 x 57 x 94) mm^3 at 7.0 T (298 MHz). At 14.0 T the modified stripline configuration produced a hotspot size of (10 x 10 x 25) mm^3 iso-SAR 90%, (17 x 17 x 40) mm^3 iso-SAR 75%, (27 x 27 x 62) mm^3 iso-SAR 50% and (37 x 37 x 93) mm^3 iso-SAR 25%.

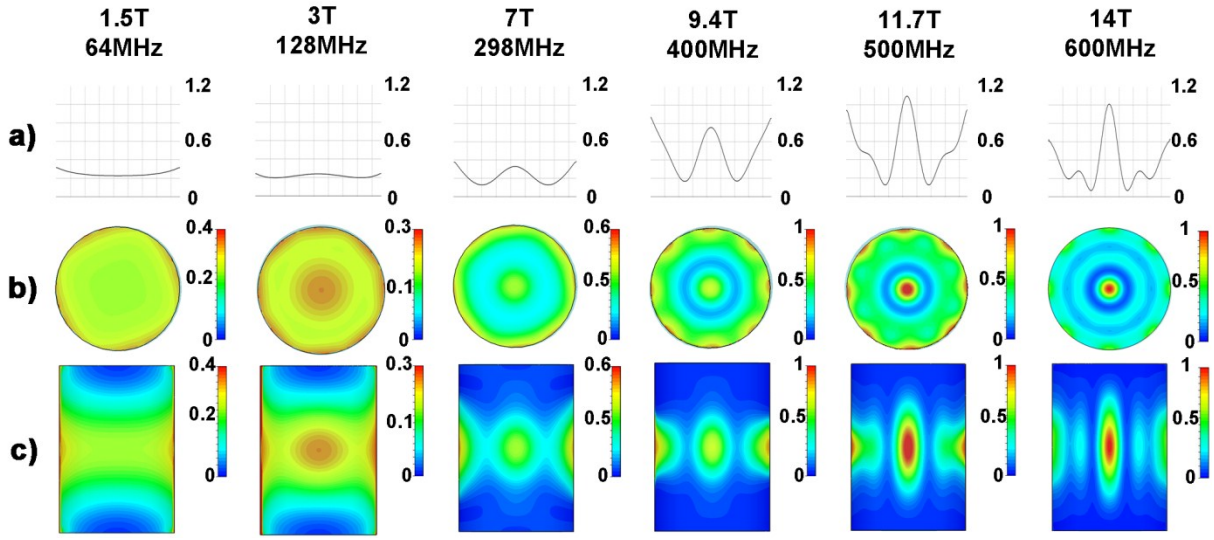

Figure 39: Synopsis of SAR simulations for frequencies ranging from 64 MHz (1.5 T) to 600 MHz (14.0 T) Point SAR [W/kg] distributions derived from numerical EMF simulations of an 8-channel bow tie antenna applicator. a) Point SAR profile along a middle line through the central axial slice of the cylindrical phantom. b) Point SAR distribution of the central axial slice of the cylindrical phantom. c) Point SAR distribution of the mid-coronal slice through the cylindrical phantom. Please note that different color scales (in the units [W/kg]) has been used to improve visualization of the central hotspot. A decrease in the size of the SAR hotspot was found for the axial and coronal view when moving to higher field strengths [65].

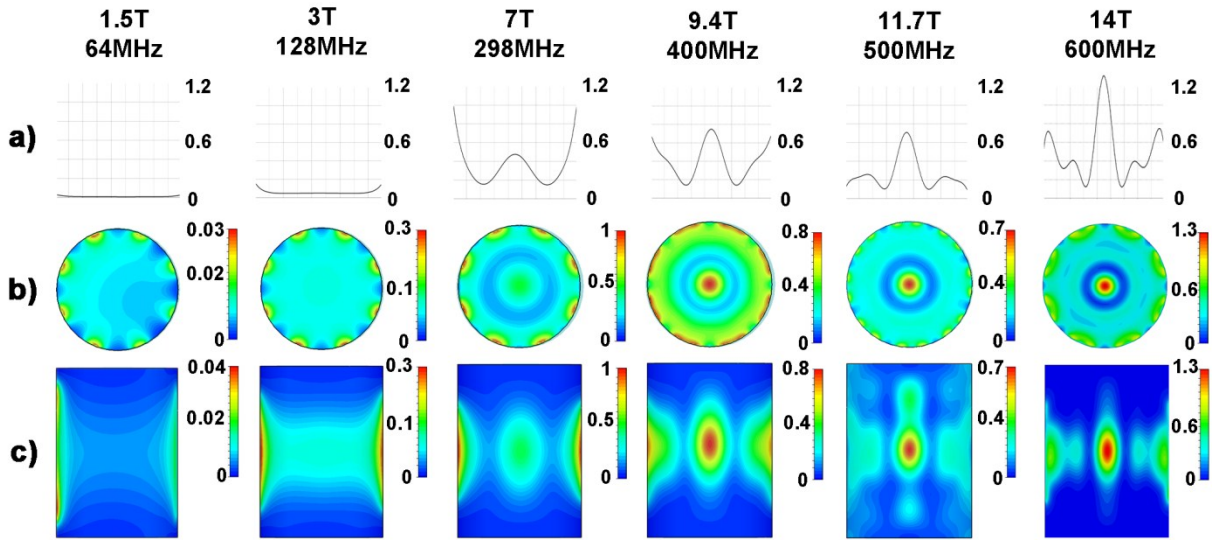

Figure 40: Synopsis of SAR simulations for frequencies ranging from 64 MHz (1.5 T) to 600 MHz (14.0 T) Point SAR [W/kg] distributions derived from numerical EMF simulations of an 8-channel modified stripline applicator. a) Point SAR profile along a middle line through the central axial slice of the cylindrical phantom. b) Point SAR distribution of the central axial slice of the cylindrical phantom. c) Point SAR distribution of the mid-coronal slice through the cylindrical phantom. Please note that different color scales (in the units [W/kg]) has been used to improve visualization of the central hotspot. A decrease in the size of the SAR hotspot was found for the axial and coronal view when moving to higher field strengths [215].

	Frequency	iso-SAR 90% [mm³]	iso-SAR 75% [mm³]	iso-SAR 50% [mm³]	iso-SAR 25% [mm³]
Modified Stripline	64MHz	O	O	O	172x172x27
	128MHz	O	O	O	172x172x88
	298MHz	O	O	O	57x57x94
	400MHz	16x16x36	27x27x55	42x42x84	60x60x121
	500MHz	13x13x23	22x22x37	34x34x60	48x48x139
	600MHz	10x10x25	17x17x40	27x27x62	37x37x93
Dipole Bowtie	64MHz	O	O	172x172x98	172x172x157
	128MHz	59x59x50	172x172x84	172x172x129	172x172x171
	298MHz	O	O	43x43x54	172x172x93
	400MHz	O	20x20x33	38x38x64	59x59x95
	500MHz	12x12x35	20x20x59	32x32x91	44x44x139
	600MHz	10x10x37	17x17x63	26x26x101	35x35x145

Table 2: iso-SAR central hotspot dimensions of the point SAR distributions of the modified stripline (top) and the bow tie dipole antenna (bottom) along lines in x-y-z direction crossing the center of the phantom. The calculations are based on the total maximum SAR value found in the phantom. “O” indicates that no iso-SAR hotspot was found in the center of the phantom, since e.g. the surface SAR values exceeded the central hotspot SAR values by far [65].

	Frequency	iso-SAR 90% [mm]	iso-SAR 75% [mm]	iso-SAR 50% [mm]	iso-SAR 25% [mm]
Modified Stripline	64MHz	2	5	13	86
	128MHz	1	4	14	86
	298MHz	2	5	12	28
	400MHz	-	3	24	40
	500MHz	-	-	-	42
	600MHz	-	-	-	19
Dipole Bowtie	64MHz	10	40	86	86
	128MHz	8	86	86	86
	298MHz	1	5	17	86
	400MHz	5	13	27	41
	500MHz	1	6	16	44
	600MHz	-	-	5	18

Table 3: iso-SAR surface hotspot depth of the point SAR distributions of the modified stripline (top) and the bow tie dipole antenna (bottom). The calculations are based on the total maximum SAR value found in the phantom. “-” indicates that no iso-SAR hotspot was found on the surface of the phantom, since e.g. the central hotspot SAR values exceeded the surface SAR values by far [215].

5.8 RF Antenna Design

The numerical EMF simulations yielded suitable targeted RF heating performance for the modified stripline and the bow tie dipole antennas. At 298 MHz (7.0 T) an iso-SAR 50% central power absorption was determined for the bow tie dipole array. For the same frequency the stripline array revealed only an iso-SAR 25% central region as highlighted in Table 2. This difference in performance render the bow tie dipole building block suitable for a proof-of-principle study at 7.0 T MR frequency due to an increased RF heating efficiency (Equ.(60)). To meet this goal an 8-channel applicator consisting of bow tie dipole antenna building blocks was constructed and evaluated for MR imaging and RF heating applications.

5.8.1 Bow Tie Electric Dipole Building Block

A single bow tie antenna building block with the dimensions of (156 x 70 x 68) mm^3 was built and adjusted to the 7.0 T MR frequency (298 MHz). Figure 41a-b show detailed views of the final design. The presented bow tie was chosen over a rectangular strip due to an increased 3dB bandwidth of 143 MHz versus 78 MHz of a 10 mm rectangular strip dipole as demonstrated by the simulations. This offers the advantage of an improved object specific tuning and matching. For the substrate the high permittivity medium Deuteriumoxide (D_2O, isotopic purity 99.9 atom % D, Sigma Aldrich GmbH, Munich, Germany) was employed. This affords smaller antenna dimensions, since the wavelength is shortened as described in Equ.(53). The gyromagnetic ratio of deuterium deviates from hydrogen and hence produces no signal at the ^1H TX/RX frequency and the limited excitation bandwidth used. This approach helps to acquire images free of artifacts caused by signal contributions from ^2H deuteron substrate. A soluble substrate provides the benefit of an increased flexibility to change the permittivity versus solid configurations. It also offers means for surface cooling, a feature beneficial for targeted RF heating interventions. The bow tie antenna was immersed in D_2O substrate inside a polymethylmethacrylat (PMMA) cover with the dimensions of (40 x 150 x 70) mm^3. From the antenna tip a parallel transmission line was connected to the matching and tuning network, which is located outside of the PMMA box (Figure 41b). To cope with a high power and voltage, highly voltage-proof nonmagnetic trimmers (Voltronics, Salisbury, USA) were used. The antennas were realized on a printed circuit board (PCB) to improve reproducibility of the antenna losses between elements. For each element a cable trap – each consisting of a single loop cable, a fixed capacitor and a variable capacitor - was placed in the feeding cable creating a tuned parallel resonant circuit (Figure 41c). Coaxial semi rigid cables were used to guarantee 50 Ohm impedance conditions of the cable trap and to avoid excessive heating with the given power throughput. The basic scheme of the circuit used for

a bow tie dipole element together with the matching and tuning network and the cable trap is depicted in Figure 41d.

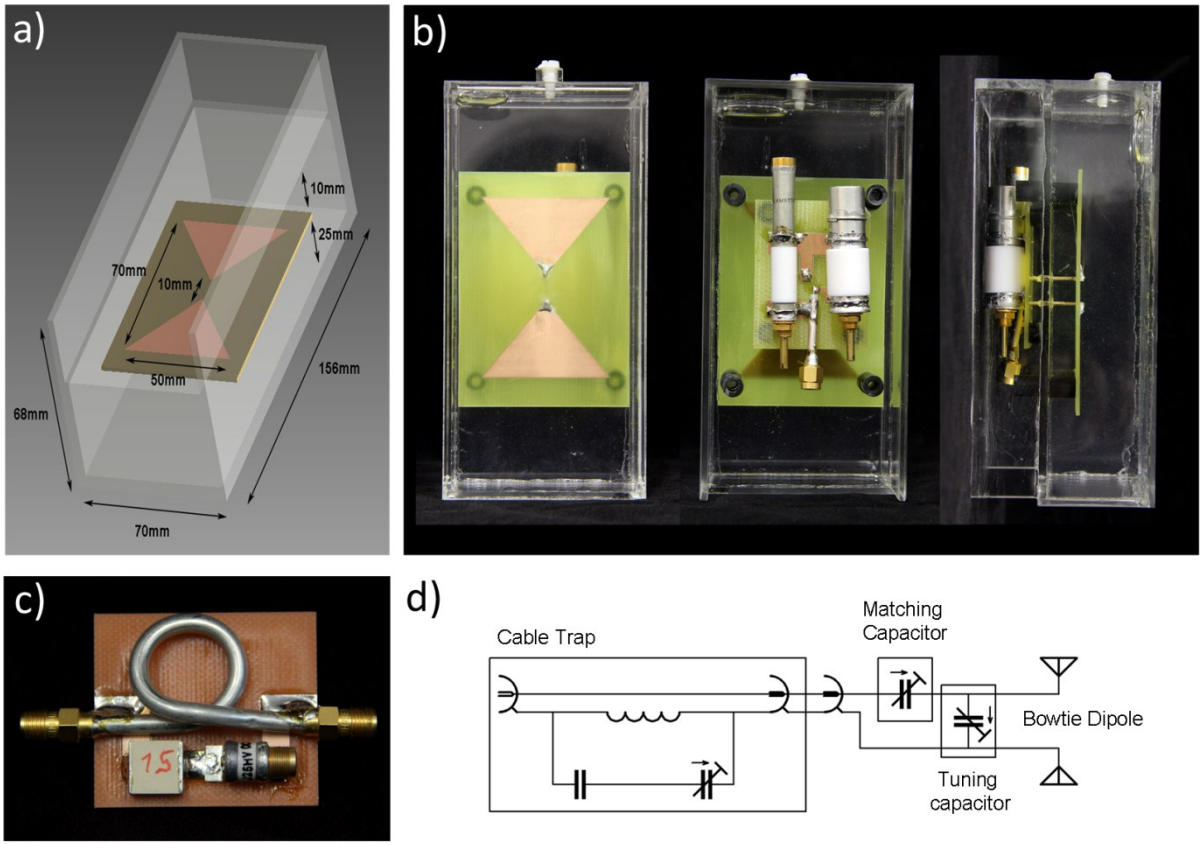

Figure 41: a) Basic design and dimensions of the bow tie dipole antenna building block developed in this work for MR imaging, MR thermometry and RF heating experiments at 7.0 T. b) Picture photographs taken from the front, back and side of the bow tie antenna building block. c) Picture photograph of the cable trap design using semi rigid cable. d) Schematic diagram of the matching and tuning network connected to the antenna [65].

5.8.2 MR Imaging Evaluation – Single Element

Matching and tuning parameters were below -25dB. Decoupling between elements was found to be below -21dB in the phantom setup. For imaging, the transmit field efficiency $B_{1+}/\sqrt{P_{Delivered}}$ was evaluated and validated with EMF simulations. For this purpose B_1^+ maps were acquired in the phantom using the Bloch Siegert method [218] in conjunction with a slice selective 2D gradient echo technique [219]. A comparison of the acquired B_1^+ maps with the B_1^+ maps deduced from the numerical EMF simulations is shown in Figure 42. B_1^+ mapping yielded a B_1^+ of 8.2 µT/√kW in the center of the phantom and a B_1^+ of 42 µT/√kW at the phantoms surface. In comparison, EMF simulations revealed a B_1^+ of 8.2 µT/√kW in the center and a B_1^+ of 59 µT/√kW at the surface of the phantom.

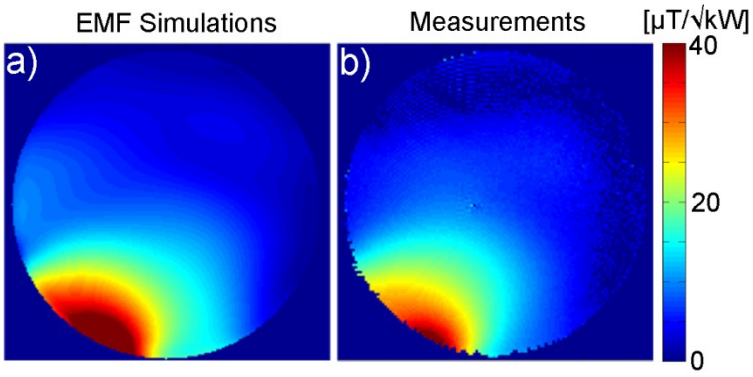

Figure 42: Simulated (left) and measured (right) B_1^+ maps in [µT/√kW] derived from a single element. For this purpose a transversal slice through the center of the phantom was used [65].

5.8.3 Assessment of RF Heating with a Single Bow Tie Antenna Element

The RF heating performance of a single bow tie dipole building block was examined in simulations and experiments. For this purpose a phantom was designed and built to allow a setup that meets the needs for reproducible evaluations. The phantom is illustrated in Figure 43.

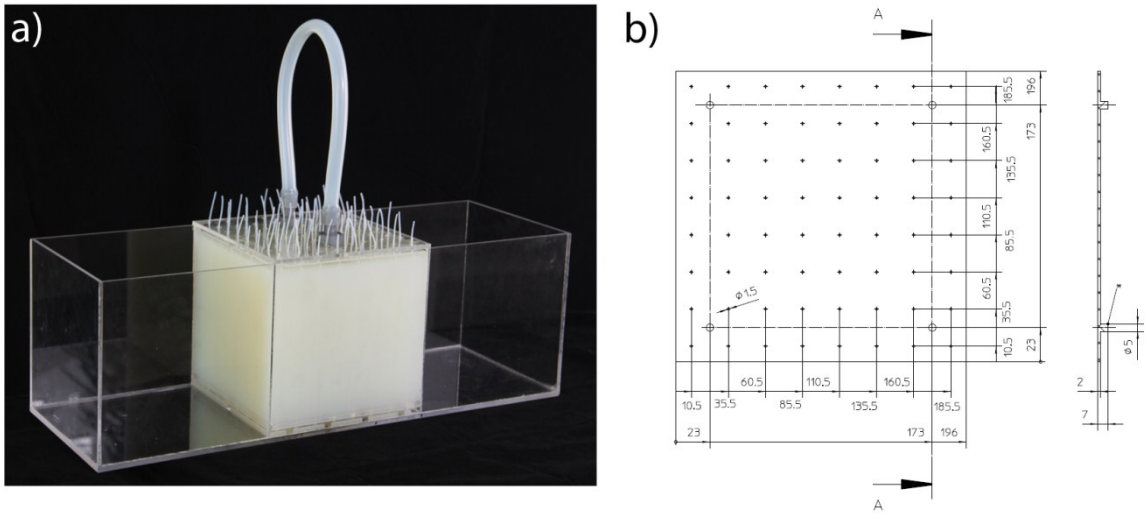

Figure 43: a) Picture photograph of rectangular phantom consisting of three compartments with the middle compartment filled with brain tissue mimicking material. 64 PTFE tubes were incorporated into the phantom to accommodate fiber optic probes (OmniFlex, Neoptix, Quebec, Canada) used for temperature measurements. b) Positioning of the PTFE tubes in a horizontal plane through the phantom.

The phantom has overall dimensions of (510 x 200 x 200) mm³ and consists of three compartments. The middle compartment was filled with tissue mimicking material following three requirements:

1. The use of a solid material to avoid convection during RF heating experiments.

2. The electromagnetic properties should yield comparable power absorption distributions as compared to brain tissue ($\varepsilon = 52, \sigma = 0.55$) [103].

3. MR imaging capabilities of the material used should allow fast MR thermometry evaluations.

These requirements were met by using a mixture of deionized water, 20g/l agarose, 3.3g/l NaCl and 0.72g/l $CuSO_4$. Agarose was used to bind deionized water which resulted in a permittivity of ($\varepsilon = 75$) to form a relative temperature resistant solid that offers sufficient MR signal due to a high water content. To shorten the T_1 relaxation time of the deionized water which is in the range of ~3000ms at 7.0 T and to allow for fast magnetization recovery for MRTh, $CuSO_4$ was added to the mixture. $CuSO_4$ additionally acts as a preservative and inhibits the decaying process of the phantom substance. Since $CuSO_4$ has only minor impact on the phantom conductivity, NaCl was added. NaCl doesn't affect T_1 significantly but increases the conductivity to its desired values. Adjusting the phantom to the right permittivity value of brain tissue is slightly more challenging since the chemical binding of agarose and deionized water take effect at high temperature and additives like sugar to lower the permittivity can't be used. However wave propagation depends both on permittivity and conductivity. Hence a slight increase of the conductivity may improve the SAR distribution towards a more realistic scenario leading to the final permittivity and conductivity ($\varepsilon = 75, \sigma = 0.75$) values of the phantom [220].

RF heating simulations and experiments were performed with a single bow tie antenna building block mounted in one of the empty compartments of the phantom and matched to the phantom's medium. A total power of 100 W was applied at the antenna for 10 minutes, which was monitored constantly during the experiments with a power reflection meter (Rhode & Schwarz, München, Germany). MR thermometry was performed using a volume excitation RF coil (Siemens, Erlangen, Germany), while a vegetable oil reference was used to compensate for a B_0 drift. To validate the fidelity of MRTh four fiber optic temperature probes (OmniFlex, Neoptix, Quebec, Canada) were positioned inside the phantom at different depths. The results of the temperature simulations and RF heating experiments are shown in Figure 44. A good qualitative and quantitative match between simulations and experiments was achieved as demonstrated in Figure 44c. Fiber optic temperature probe measurements resemble MR thermometry values. The simulations revealed a minor overestimation of the temperature distribution across the phantom derived from MR thermometry and from the fiber optic probes. This minor discrepancy is due to losses of the antenna that were not accounted for in the simulated model. In total the single bow tie antenna was able to heat up the phantom to ~49°C at the surface, while at a depth of 40mm, a temperature increase of 7°C was observed. These results demonstrated reasonable RF heating performance and provided encouragement to move forward in the development of a multi-channel RF heating setup.

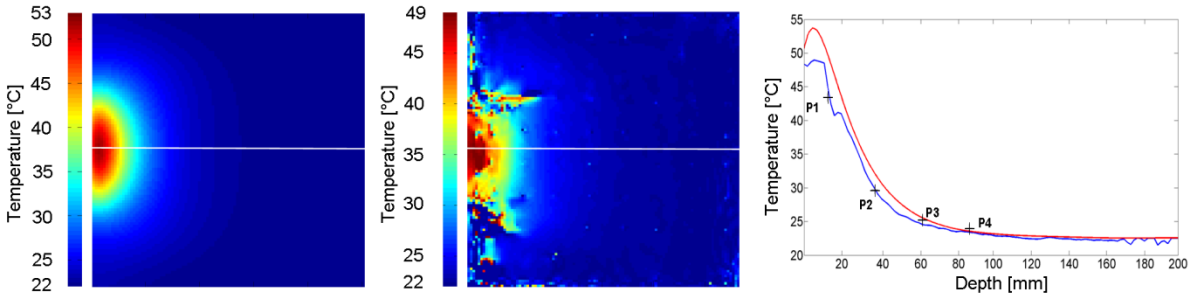

Figure 44: Validation of the temperature simulation results (left) of a single bow tie antenna and experimental results derived from MR thermometry (center). Right) Temperature profile along the center of the temperature distribution obtained from the numerical simulations(red line) and derived from MR thermometry (blue line). P1 to P4 indicate the position and temperature observed with fibre optical MR thermometry probes (OmniFlex, Neoptix, Quebec, Canada) integrated in the phantom.

5.9 8-channel RF Heating/MR imaging/MR thermometry Hybrid Applicator

After demonstrating MR imaging and RF heating capabilities a hybrid multichannel applicator consisting of eight bow tie dipole building blocks was developed. The number of transmit elements was set to eight to use the full capabilities of our multi-channel transmit system (TX-Array, Siemens, Erlangen, Germany) available at the 7.0 T MR scanner. The eight elements were placed in an equidistant radial order in a stereotactic holder. For accurate placement of the eight antennas the holder was created using a 3D computer aided design (CAD) model developed with Autodesk Inventor 2011 (Autodesk Inc., San Rafael, CA, USA). The holder was plotted with a 3D rapid prototyping system (BST 1200 es, Dimension Inc., Eden Prairie, MN, USA) using ABS+ material. Figure 45 illustrates the final setup of the 8-channel hybrid TX/RX applicator tailored for MR imaging, MR thermometry and targeted RF heating in a 7.0 T environment.

For targeted RF heating an input RF power that exceeds the clinical standards given by the IEC guidelines was applied. For *in vivo* MR imaging however, the energy deposition in tissue was limited to the values proposed by the IEC 60601-2-33 Ed.3. guidelines [91] to guarantee a safe application of the transmitted electromagnetic fields. Numerical SAR (10g average) calculations were performed together with the human voxel models "Duke" and “Ella” from the virtual family [109]. Whole body SAR, partial body SAR and local SAR values were evaluated and the power limits were set accordingly.

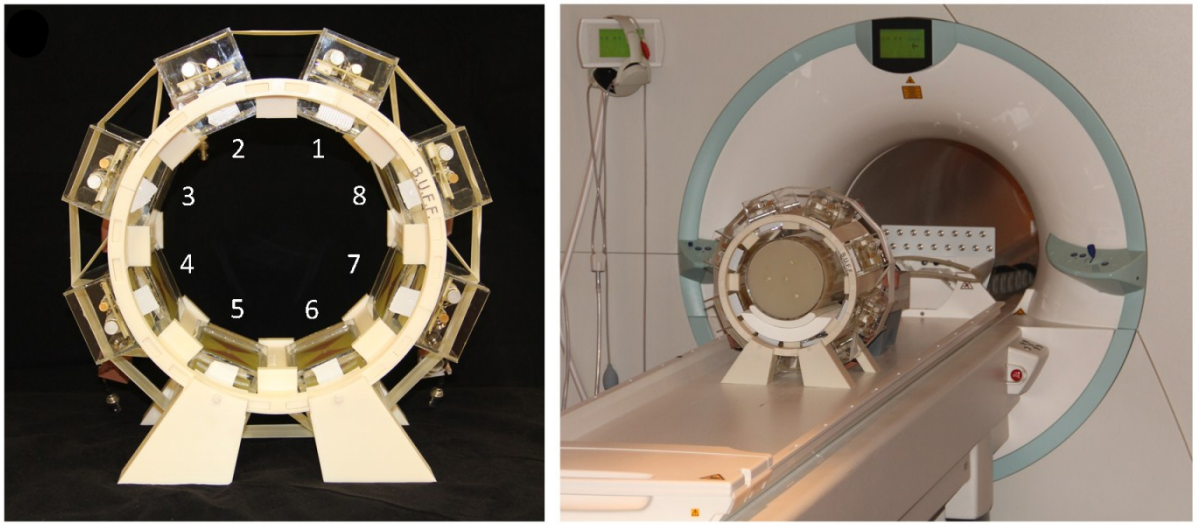

Figure 45: Experimental setup of the hybrid applicator used at a magnetic field strength of 7.0 T.(Left) Picture photograph of the eight channel TX/RX hybrid applicator implemented at 7.0 T together with annotations that induce the transmission channel number. (Right) Picture photograph of the experimental setup which uses the hybrid applicator together with a cylindrical phantom at 7.0 T [65].

All measurements were performed on a 7.0 T whole body MR system (Magnetom, Siemens Healthcare, Erlangen, Germany). For MR imaging, MRTh and targeted RF heating a set of eight power amplifiers (Stolberg HF Technik AG, Stolberg-Vicht, Germany) – each offering 1kW maximum peak power together with independent control of phase and amplitudes - were connected with the eight channel dipole antenna elements of the hybrid applicator. For this purpose the applicator was connected to the MR system via a RF coil interface comprising 8 TX/RX switches and low-noise preamplifiers (Stark Contrasts, Erlangen, Germany).

5.9.1 Assessment of the Hybrid's Applicability for *In Vivo* MR Imaging

For human brain imaging B_1^+ maps were acquired for each channel to gain a better insight into the transmit fields inside a heterogeneous object. This set of B_1^+ maps was used for slice selective B_1^+ shimming using the parallel TX PulseDesign Suite (Siemens Healthcare, Erlangen, Germany) with the goal of improving B_1^+ uniformity across an axial slice of a volunteer's brain. In vivo B_1^+ maps derived from B_1^+ mapping of each element are depicted in Figure 46 for a mid-axial slice of the brain.

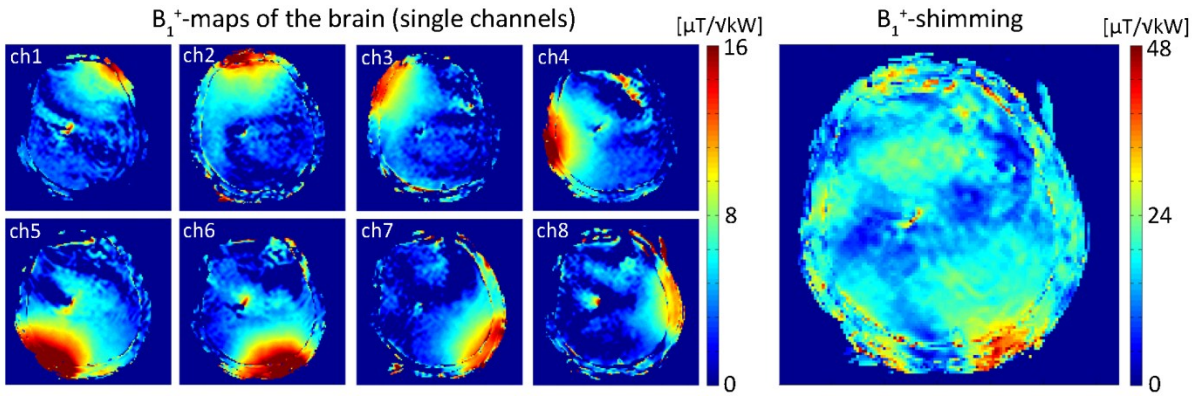

Figure 46: Transmission fields (B_1^+) of the hybrid applicator at 7.0 T in the human brain. left) In vivo brain B_1^+ maps were obtained from Bloch Siegert mapping of the eight independent channels of the applicator. For B_1^+ mapping an axial slice through the subject's brain was used. right) B_1^+ map of the volunteers brain after B_1^+ shimming. The B_1^+ map shows rather uniform B_1^+ distribution [65].

A phase only B_1^+ shim optimization using Newton's method with the goal function on B_1^+ homogeneity over the whole brain slice revealed transmitter phases of 69° (Ch1), 156° (Ch2), 74° (Ch3), 129° (Ch4), 92° (Ch5), 0° (Ch6), 276° (Ch7) and 147° (Ch8). This phase setting yielded an average B_1^+ of 17.2 µT/√kW over the whole mid-axial slice of the human brain with a standard deviation of 6.2 µT/√kW. This subject specific B_1^+ shim was used for gradient echo imaging of the brain at 7.0 T as shown in Figure 47.

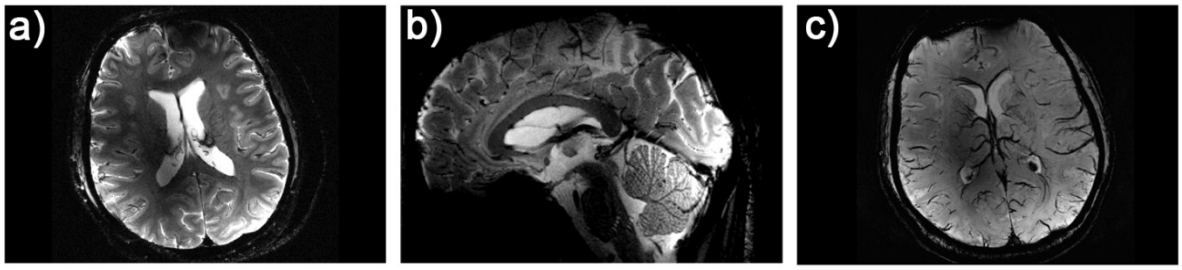

Figure 47: Illustration of the *in vivo* imaging capabilities of the hybrid TX/RX applicator driven by bow tie dipole antennas. a,b) High spatial resolution MR images of the human brain. A gradient echo technique was used with a spatial resolution of: (0.5 x 0.5 x 2.0) mm³, FOV:(200 x 175) mm², TR = 989 ms, TE = 25 ms, reference transmitter voltage U_{ref} = 170 V, nominal flip angle = 35°, receiver bandwidth = 30 Hz/pixel. c) Minimum intensity projection derived from susceptibility weighted 3D gradient echo imaging of the human brain. Imaging parameters: spatial resolution: (0.5 x 0.4 x 1.2) mm³, FOV=(184 x 184) mm², TR = 25 ms, TE = 14 ms, reference transmitter voltage U_{ref} = 170 V, nominal flip angle = 24°, 16 slices per slab, receiver bandwidth=120 Hz/pixel, flow compensation [65].

To examine the parallel imaging performance of the hybrid applicator, geometry factor (g-factor) maps were determined using acceleration factors of R=2, R=3 and R=4 together with GRAPPA

reconstruction using 32 calibration lines [221]. For this purpose the noise of every element was measured *in vivo* using a noise prescan [64]. The assessment of the hybrid applicators parallel imaging performance revealed mean g-factors of 1.2±0.1 for R=2, 1.7±0.4 for R=3 and 2.7±0.7 R=4 for an axial slice through the brain. Noise correlation (*in vivo*) was 0.16 ± 0.09 (mean ± std) for all elements with a maximum measured value of 0.36 between element 6 and element 8.

Due to its building block design the antenna elements can be arranged arbitrarily. The advantages of a combination of dipole antenna and dielectric resonator (D_20 substrate) enables very good decoupling (<-15dB) between adjacent elements; even if the elements are positioned directly next to each other. The electric boundary conditions at the D_20 – air interface direct the energy into the object instead of the neighboring elements. Consequently MR imaging applications are not limited to the brain, but can also be performed in other regions of the body like the abdomen. With this in mind the proposed bow tie dipoles were applied to cardiac imaging at 7.0 T. Here an 8-channel bow tie transmit/receive array tailored for cardiac MR was used successfully to achieve first real time cardiac images at 7.0 T, as illustrated in Figure 48, in collaboration with Prof. Jens Frahms group [222]. The proposed design yielded furthermore sufficient B_1^+ magnitude and homogeneity for high spatial resolution black blood imaging of the human heart (Figure 48b) and T_2^* mapping (Figure 48b) of the human heart in collaboration with Katharina Fuchs and Fabian Hezel from the B.U.F.F. [117, 223, 224].

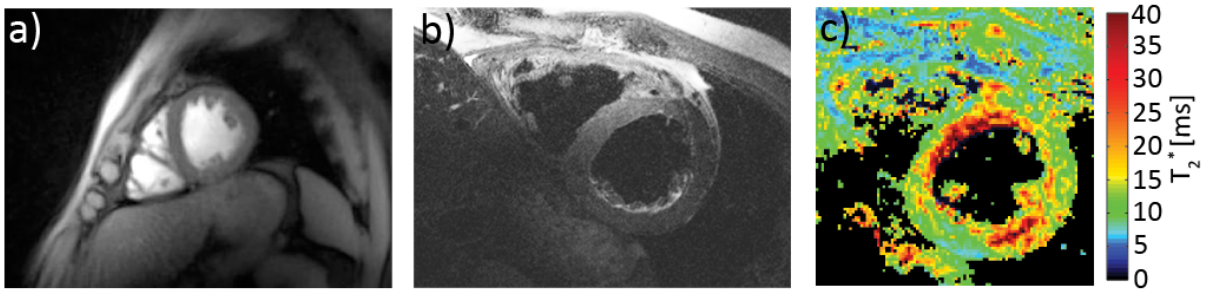

Figure 48: Advanced MR imaging examples acquired with an 8-channel transmit/receive array tailored for cardiac MR at 7T. a) Single cardiac phase derived from real time imaging of a short axis view of the heart in collaboration with Prof. Jens Frahm (Max-Planck Institute, Goettingen, Germany) and his team. b) Black blood imaging of a short axis view of the heart at 7.0 T with an exquisite spatial resolution of (0.8 x 0.8 x 3) mm^3 [223]. c) Calculated T_2^* map of the myocardium derived from a series of high spatial resolution split-echo RARE images of a short axis view of the heart [224].

The concept to increase the number of transceiver elements to achieve improved image quality [57] can be translated to bow tie dipoles as well. Figure 49 shows a transmit/receive cardiac RF coil prototype consisting of 16 bow tie dipole antennas. Such setup promises an increased degree of freedom to alter the B_1^+ distribution and improve B_1^+ homogeneity with the goal of increasing SNR

and to improve parallel imaging performance. For transmission and reception the output of the RF amplifier was split into 8 equal-intensity signals using power splitters and connected to 16 transmit/receive switches (Stark Contrasts, Erlangen, Germany). Phase shifting cables were used to homogenize the B_1^+ field distribution inside the torso. The phase setting optimization was performed based on simulated data with the voxel model "Duke" (Virtual Family, IT IS Foundation, Switzerland), using a Levenberg-Marquardt algorithm with 1000 starting points on a four chamber view of the heart. Cardiac standard views (four chamber view, three chamber view, two chamber view, midventricular short axis view) were acquired and are depicted in Figure 49. Please note that all displayed images were acquired from the same volunteer and a single phase setting not changing the phases between cardiac standard views.

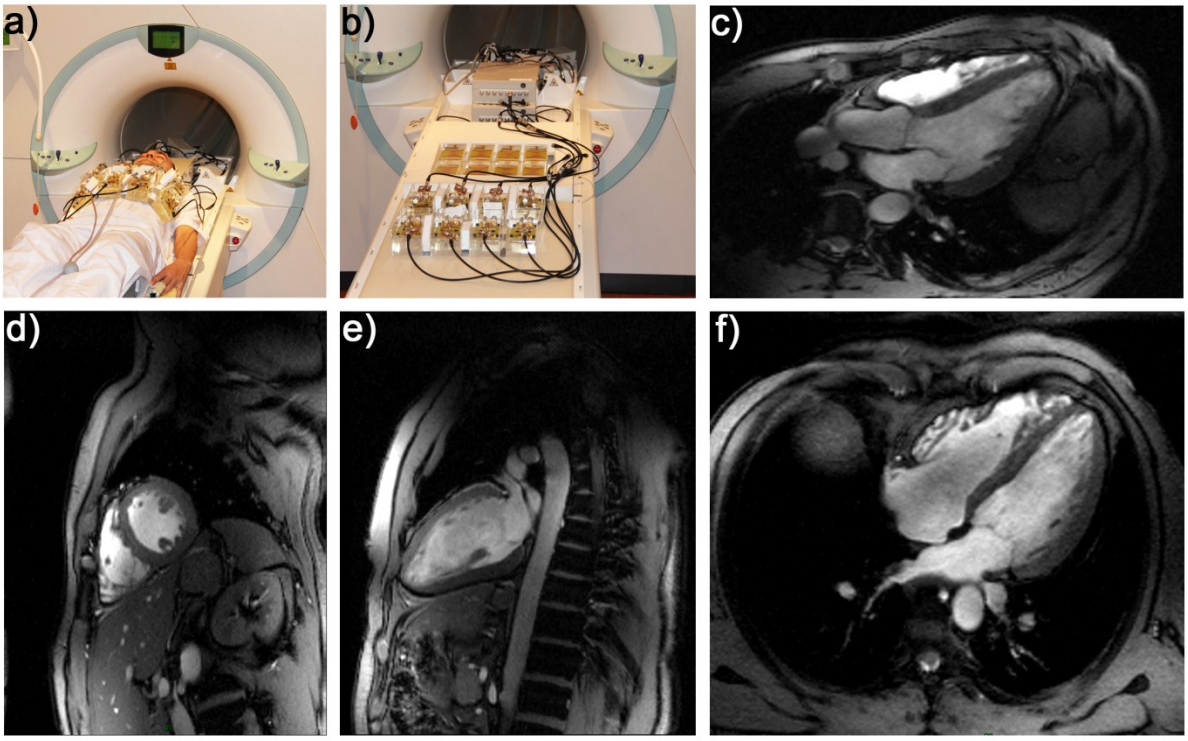

Figure 49: (a) The proposed 16-channel bow tie dipole TX/RX RF coil array positioned on a volunteer. (b) Anterior (2x8) and posterior (2x8) part of the bow tie dipole cardiac array together with the hardware setup and fixed RF shim phase setting using phase delay cables at a 7.0 T MR scanner. 2D CINE gradient echo images of a three chamber view (c), short axis view (d), two chamber view (e) and four chamber view (f) of the human heart acquired for a single volunteer and fixed phase setting [225].

A 2D CINE gradient echo technique was used with the parameters: spatial resolution (1.4 x1.4 x 4) mm^3, TE = 2.7 ms, TR =5.6 ms, 30 cardiac phases, 8 views per segment, receiver bandwidth = 444 Hz/Px. As demonstrated high resolution imaging is feasible and allows for the visibility of subtle anatomical details. What is more intriguing is the homogeneous B_1^+ over the given

field of view and across the cardiac standard views with no visible strong B_1^+ destructive interference manifesting as “black holes” in the images. Admittedly, further works needs to be invested in a subject dependent evaluation of homogeneity and transmit efficiency using B_1^+ mapping techniques [219]. With a poynting vector directing to the imaging region and a localized entry point for the electromagnetic wave through the high permittivity dielectric, the proposed bow tie dipole array has potential advantages for improvements in B_1^+ homogeneity and B_1^+ shimming techniques [226].

5.9.2 Assessment of the Hybrid’s Applicability for Targeted RF Heating

To evaluate targeted RF heating phantom experiments with high RF power transmission were performed. For RF heating application an additional continuous wave amplifier is usually utilized yielding sufficient averaged RF power [11]. In contrast to this conventional approach in this work an RFPA of the MR system (Stolberg HF Technik AG, Stolberg-Vicht, Germany) was used for the targeted RF heating application of the hybrid applicator. The MR scanners RFPA is a narrow band amplifier adjusted for pulsed power operation with a maximum peak power of 8 kW. To generate sufficient RF power a rectangular pulse with a pulse duration of 4 ms was used together with a TR of 32 ms and an amplitude of U = 170V. This setup affords a duty cycle of 13% and an average power of approximately 72 W per transmission channel. Cable losses of around 30% lead to an average power of 50 W at one antenna. Antenna losses were not taken into account. Two phase settings were used for the assessment of the applicator:

PS 1: All elements with 0° phase shift between channels to induce a SAR and temperature hotspot in the center of a cylindrical phantom, which was constructed for these experiments (diameter = 172 mm, length = 250 mm, $\sigma_2 = 0.72$ S/m, $\varepsilon_2 = 75$).

PS 2: A phase setting to demonstrate the feasibility of 2D steering of the SAR and temperature hotspot.

The phase settings used for RF heating were derived from numerical E-field simulations. For PS 1 the heating period was 180 s followed by the acquisition of the temperature maps using the hybrid applicator. For PS2 (Ch1:0°, Ch2:45°, Ch3:180°, Ch4:225°, Ch5:0°, Ch6:225°, Ch7:135°, Ch8:45°) the heating period was 120s followed by the acquisition of the temperature maps using the hybrid applicator. The results are depicted in Figure 50 and Figure 51. For PS 1 the EMF simulations showed higher SAR values in the center of the phantom compared to the surface regions (Figure 50). The surface SAR in the agarose phantom didn’t exceed a value of 0.52 W/kg for 1 W input power. In

comparison, the center of the phantom showed a value of 0.79 W/kg. The simulated SAR hotspot in the phantom yielded dimensions of (19 x 19 x 28) mm³ for iso-SAR 90%, (31 x 31 x 47) mm³ for iso-SAR 75%, (48 x 48 x 71) mm³ for iso-SAR 50% and (70 x 70 x 99) mm³ for iso-SAR 25%. For the temperature co-simulations the resulting temperature increase due to the calculated power loss distribution was ΔT = 11.6°C in the center and ΔT = 7.4 °C at the surface of the phantom.

The RF heating experiments confirmed the predictions of the EMF simulations. MR temperature maps are shown in Figure 50. After a heating period of 180 s with approximately 50 W average power per channel a maximum temperature increase of $\Delta T = 10.7$ °C (averaged value over 9 pixel) was obtained for the center of the phantom. The maximum temperature increase found for a surface region of the phantom was $\Delta T = 6.7$ °C (averaged over 9 pixel). For absolute temperature measurements and for validation of the MR thermometry maps, four optical thermo sensors were employed (OmniFlex, Neoptix, Quebec, Canada) with their location depicted by P1-P4 in Figure 50a. Temperature calibration measurements were performed to scrutinize the accuracy of the MRTh method, yielding an experimental absolute error of ±1°C and a relative error of ±0.2°C for the fiber optic approach and ±2°C for MRTh. The thermo fiber optical probes confirmed the findings derived from MRTh in the targeted RF heating experiments. After the heating period a temperature increase of $\Delta T = 9.6$ °C was observed at position P2 (Figure 50) in the center of the phantom. The three fiber optic sensors positioned 4.3 cm off-center yielded a temperature increase of $\Delta T = 3$ °C at position P1 versus a temperature increase of $\Delta T = 1.7$ °C at position P3 and $\Delta T = 2$ °C at position P4.

By changing the phase setting to phase PS 2 the SAR and temperature hotspot was deliberately moved from the center of the phantom to a region close to the surface of the phantom. This phase setting configuration induced a temperature increase in a region close to the phantoms surface as demonstrated in Figure 51. The simulations revealed a SAR value of 1.01 W/kg in the center of the SAR hotspot versus SAR = 0.96 W/kg at the surface of the phantom. This SAR behavior translated into a temperature increase of $\Delta T = 11.5$ °C in the center of the hotspot. The MRTh measurements revealed a max temperature increase of $\Delta T = 8.1$ °C in the hotspot after a heating period of 120 s as shown in the temperature maps in Figure 51.

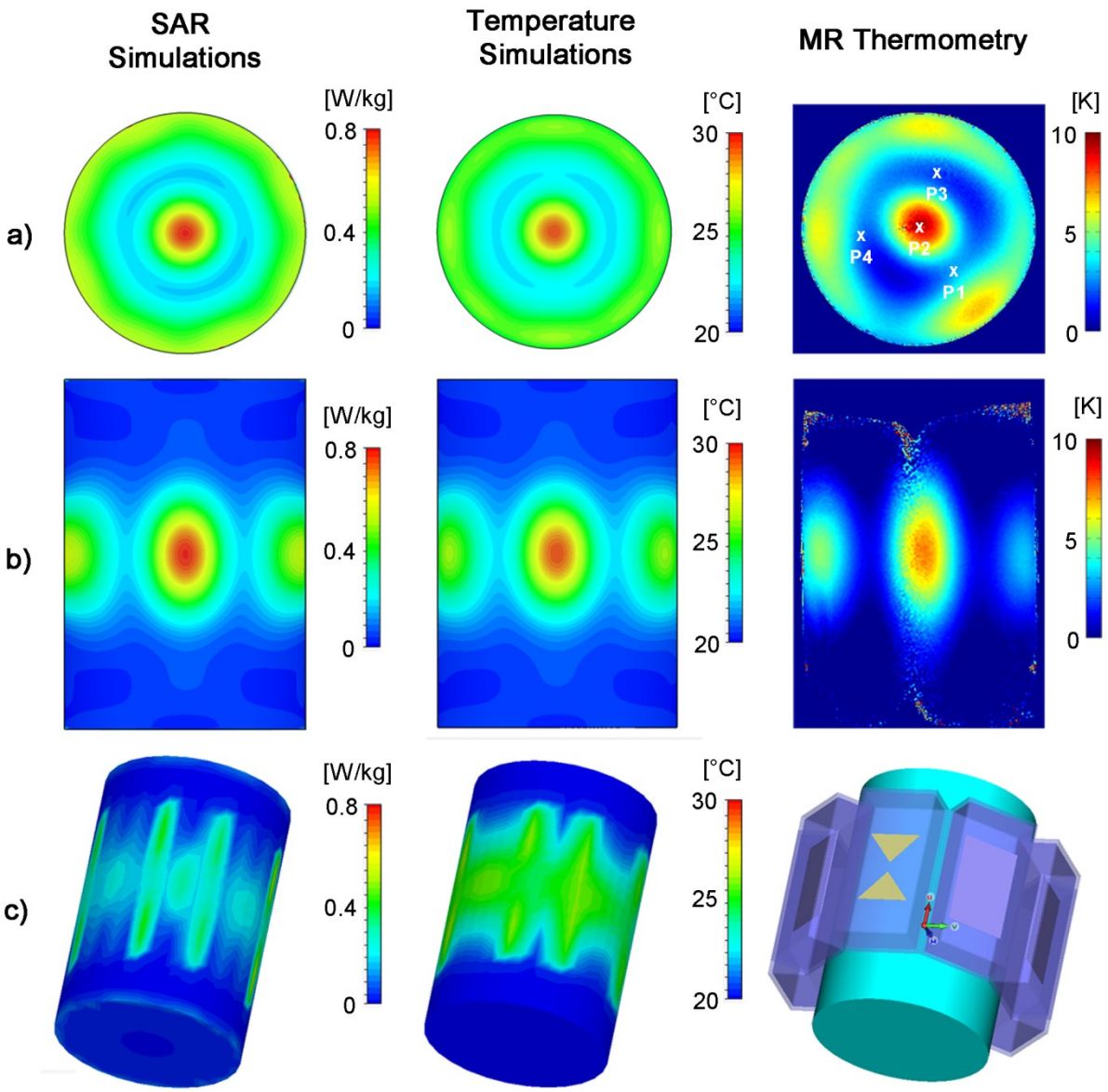

Figure 50: Targeted RF heating in a phantom: simulation and experiment. Axial (a) and coronal (b) views of the specific absorption rate (left) and temperature distribution (middle) derived from EMF and temperature simulations using the 8-channel applicator together with a cylindrical phantom and a ^{1}H spin excitation frequency of 298 MHz. For comparison, a temperature map derived from MR thermometry of the same slice at 7 T using the TX/RX applicator is shown (right). For the experimental setup a heating period of 3 min was used with an input power of 50 W per channel. SAR and temperature hotspots were induced in the center of the phantom by using no phase delay between the bow tie antennas. P1-P4 indicate the location of the fiber optic temperature probes. c) SAR (left) and temperature (middle) simulation results in a 3D view of the phantom together with the positioning of the antennas (right) [65].

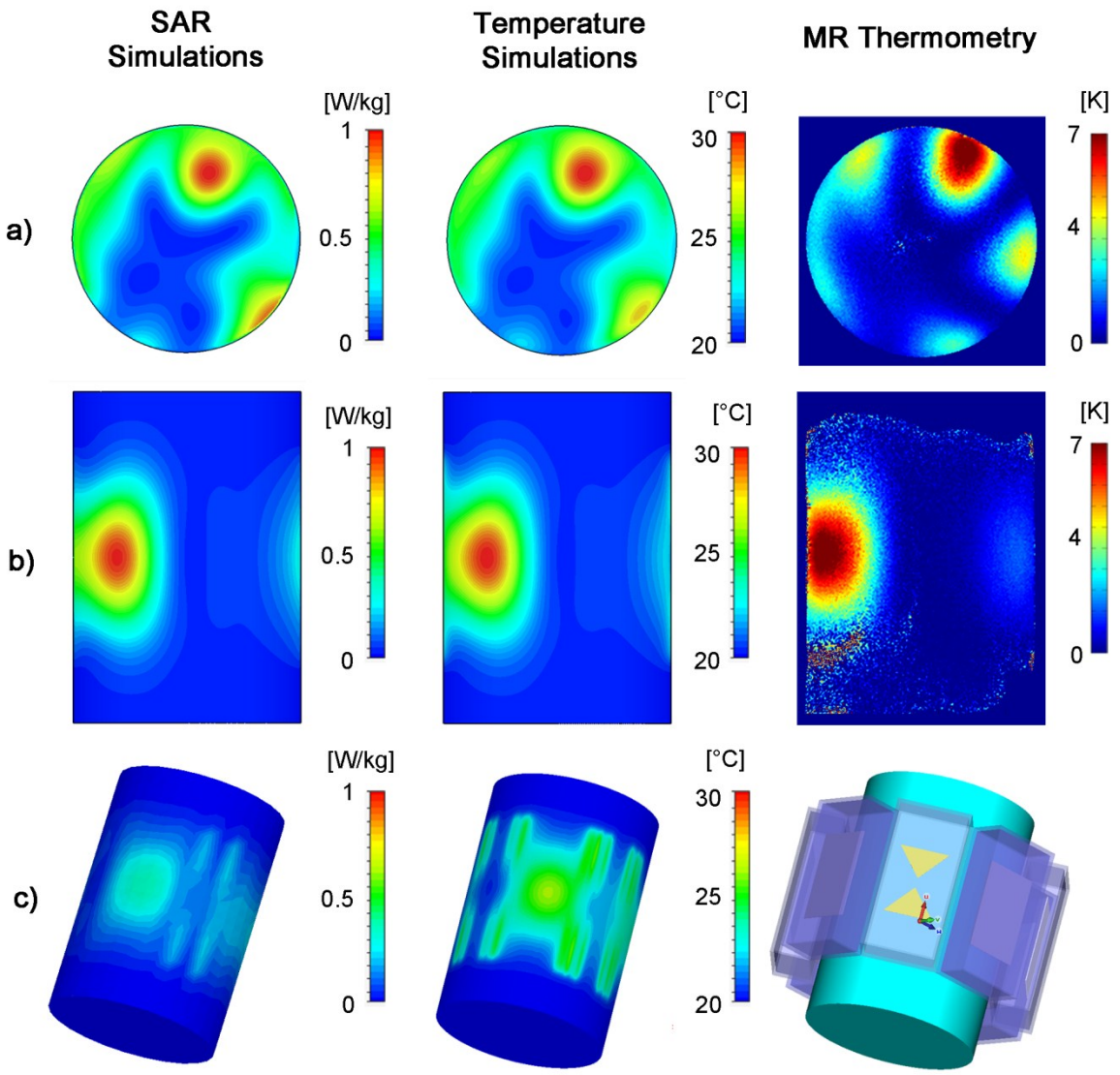

Figure 51: 2D steering of targeted RF heating in a phantom: simulation and experiment. Axial (a) and coronal (b) views of specific absorption rate (left) and temperature (middle) distribution derived from EMF and temperature simulations using the 8-channel applicator a cylindrical phantom and a ^{1}H spin excitation frequency of 298 MHz. For comparison, a temperature map derived from MRTh acquisitions at 7T using the TX/RX applicator is shown (right). For the experimental setup a heating period of 120 s was used with an input power of 50 W per channel. A set of phase shifts (Ch1:0°, Ch2:45°, Ch3:180°, Ch4:225°, Ch5:0°, Ch6:225°, Ch7:135°, Ch8:45°) between the bow tie antennas was used to steer the SAR and temperature hotspot towards the surface of the phantom. c) SAR (left) and temperature (middle) simulation results in a 3D view of the phantom together with the positioning of the antennas (right) [65].

To demonstrate the feasibility of targeted RF heating in the human brain, numerical electromagnetic simulations were coupled with temperature simulations (CST MPhysics Studio, CST GmbH, Darmstadt, Germany) in the human voxel model “Ella” derived from a healthy volunteer [109]. A water bolus with tissue equivalent properties (ε=50, σ=0.6S/m) was used i) to improve coupling of the electromagnetic waves for each RF transmission channel to the head and ii) to cool down the surface

of the head using a cooling temperature of 20°C. For this setup the input power was adjusted to 8 x 50W with an in-phase (0° phase delay between channels) phase setting that was customized to focus the E-fields in the center of the brain. The temperature simulations were performed solving Pennes bioheat transfer equation:

$$c_t \rho_t \frac{\partial T}{\partial t} = \nabla k \nabla T + \rho_t (SAR) + A - W_b c_b (T - T_b) \tag{61}$$

with the specific heat of tissue c_t, tissue density ρ_t, tissue temperature T, thermal conductivity of tissue k, basal metabolic heat rate A, the blood perfusion rate W_b, the specific heat of blood c_b and the blood temperature T_b. The duration of the temperature simulations was set to 5 minutes. The results are depicted in Figure 52a-e). After a heating period of 5min with an input power of 8 x 50W, the temperature in the central hotspot was found to be 48.6°C. For comparison the surface did not exceed a temperature of 43.3°C. The iso-temperature 90% hotspot in the axial plane showed a size of (38x47) mm².

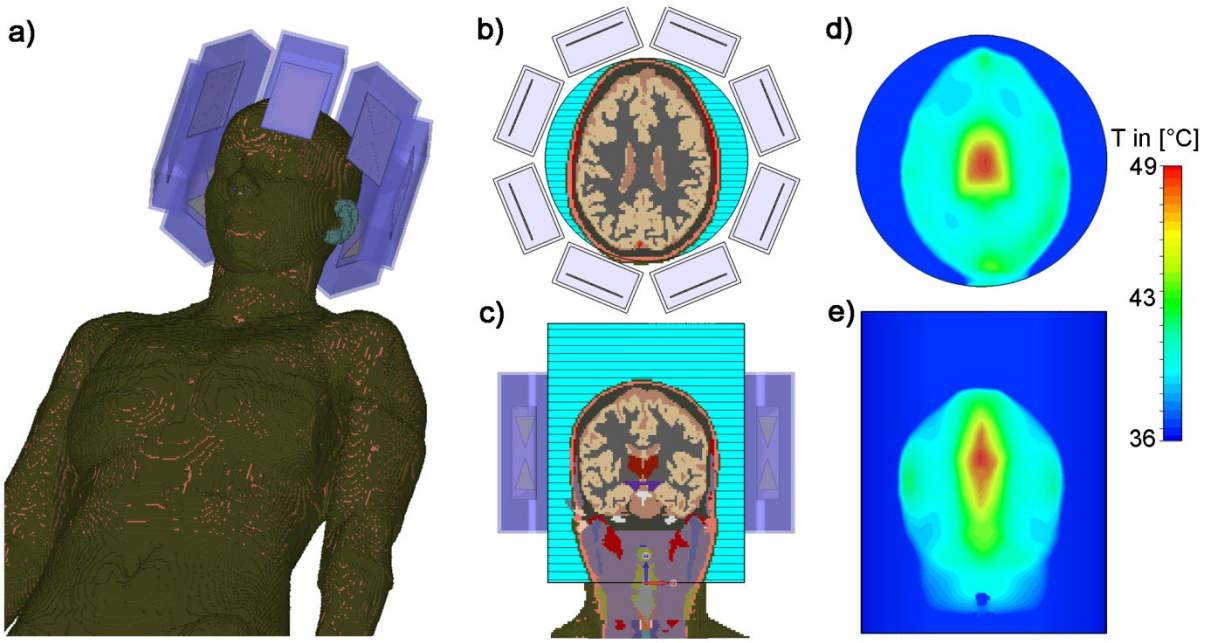

Figure 52: Simulation of RF heating in a human voxel model. Temperature simulations were performed using the *in vivo* human voxel model "Ella" [35] in conjunction with the proposed hybrid applicator. Positioning of the voxel model and eight bow tie dipole antennas are shown in (a). Axial and coronal slices through the human brain together with the water bolus (adjusted to T=20°C) are illustrated in(b-c). Simulated temperature maps for an axial and coronal slice of the human brain depicted in (d-e). For this purpose RF heating was conducted over 5 min using an average RF power of 50 W per channel at 298 MHz. For the center of the brain the maximum temperature was 48.6°C upon completion of the RF heating paradigm (d). In comparison the surface did not exceed a temperature of 43.3°C for the same heating paradigm [65].

In summary, a bow tie antenna building block was presented and evaluated for MR imaging and RF heating applications at 298 MHz. The presented design is capable of being deployed in multi-channel transmit/receive arrays for high spatial resolution brain MRI as well as body MRI applications including cardiac imaging at 7.0 T. Using the proposed 8-channel setup this work demonstrated that high power RF transmission can be accomplished that supports sufficient energy absorption in the center of a phantom to create a temperature hotspot. By the application of dynamic pulse forms this energy absorption hotspot could be steered by the MR system inside the phantom used to another deliberately chosen location. While the expected temperature hotspots based on simulations were very well reproduced throughout the experiments shown in this work, a more realistic EM simulation setup using human voxel models was employed to demonstrate that the proposed application might be feasible in the human brain *in vivo*.

6. Explorations into Frequency Ranges Exceeding the 300 MHz Regime

To this point basic feasibility of a 298 MHz hybrid RF hyperthermia and MR imaging setup was outlined in this work. The proposed setup is capable of providing enough energy while operated on a 7.0 T MR scanner (Magnetom, Siemens Healthcare, Erlangen, Germany) to heat up an elliptical area as small as (25 x 22 x 41) mm³ (simulated value: (31 x 31 x 47) mm³ for an iso-temperature of 75% inside a uniform phantom with a maximum temperature increase of ΔT=11°C [65]. EMF simulations performed in this work suggest, however that the hotspot size can be reduced even further by increasing the RF frequency [215]. This would imply an increased spatial selectivity for targeted RF hyperthermia and/or targeted drug delivery applications [9, 184]. Another major advantage of increasing the RF frequency is the reduction in antenna size. For 298 MHz the total bow tie antenna length is 7 cm while at 500 MHz the antenna length can be reduced to 2.5 cm. This has various implications. First, smaller sized antennas may increase the number of elements accommodated by a unit area or volume. This improvement is beneficial for MR imaging and holds the promise to enhance the capabilities of targeted RF heating by increasing the degree of freedom of RF distribution modifications inside the object. For all these reasons this chapter investigates the benefits of frequencies larger than f ≥ 298 MHz for targeted RF heating applications together with an evaluation of MR imaging capabilities. Electro-dynamic considerations supplement this chapter.

Antenna design and experimental validation is performed at 500 MHz which corresponds to magnetic field strength of B_0 = 11.7 T. A combined system is presented, where targeted RF heating is being performed at 500 MHz and MR imaging at 298 MHz. Investigations into dual frequency heating, electromagnetic considerations for targeted RF heating and electrodynamic constraints on MRI and EPR using frequencies above up to 1.44 GHz complete this chapter and provide the transition to the discussion section.

6.1 Towards Targeted RF Heating at f > 298 MHz

Up to date the highest one and only available UHF MR system for human *in vivo* imaging is able to generate a B_0-field of 11.7 T. To investigate the intrinsic hybrid MRI and targeted RF heating application at 11.7 T, a discrete frequency of 500 MHz has been chosen to evaluate efficiency and demonstrate feasibility. This paragraph focusses on the use of 500 MHz for targeted RF heating and MRI versus 298 MHz. These efforts include assessment of the RF antenna design, EM simulations, temperature simulations and RF heating experiments.

6.1.1 Performance Comparison: 298 MHz vs. 500 MHz

The RF antenna design at 500 MHz was based on a combination of a high permittivity low loss dielectric (D_20) and an RF bow tie antenna [65]. By increasing the RF frequency both dielectric and RF antenna can be shortened significantly. Various electric dipole antenna configurations have been simulated and evaluated. Here we focus on two 500 MHz designs (Figure 53) which are compared to the 298 MHz bow tie antenna building blocks.

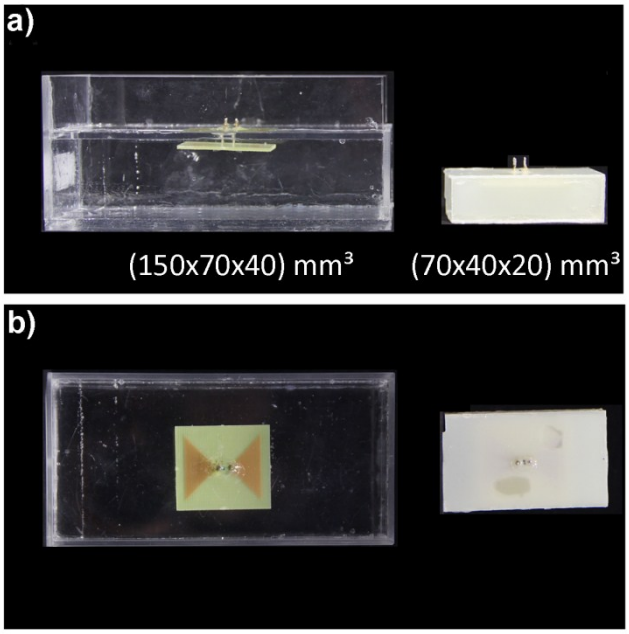

Figure 53: (A) Side view and (B) top view of two constructed RF antenna building blocks for 500 MHz using two sizes. Please note that for the smaller RF antenna building block FR-4 has been used for the casing due to reduced RF losses as compared to PMMA.

The first design adapts the dimensions of the 298 MHz dielectric with (150 x 70 x40) mm³. The second dielectric configuration was reduced to a size of (70 x 40 x 20) mm³, which demonstrates reduction in volume by a factor of more than 7 of the high permittivity dielectric. The bow tie antenna size itself is reduced from 7 cm to 2.5 cm as shown in Figure 53. SAR simulation results obtained for the two 500 MHz bow tie antenna configurations are depicted in Figure 54 and benchmarked against the 298 MHz building blocks. Here, the focusing abilities of 8-element transceiver arrays are compared, evaluating the iso-SAR 25-90% values. The results are presented in Table 4.

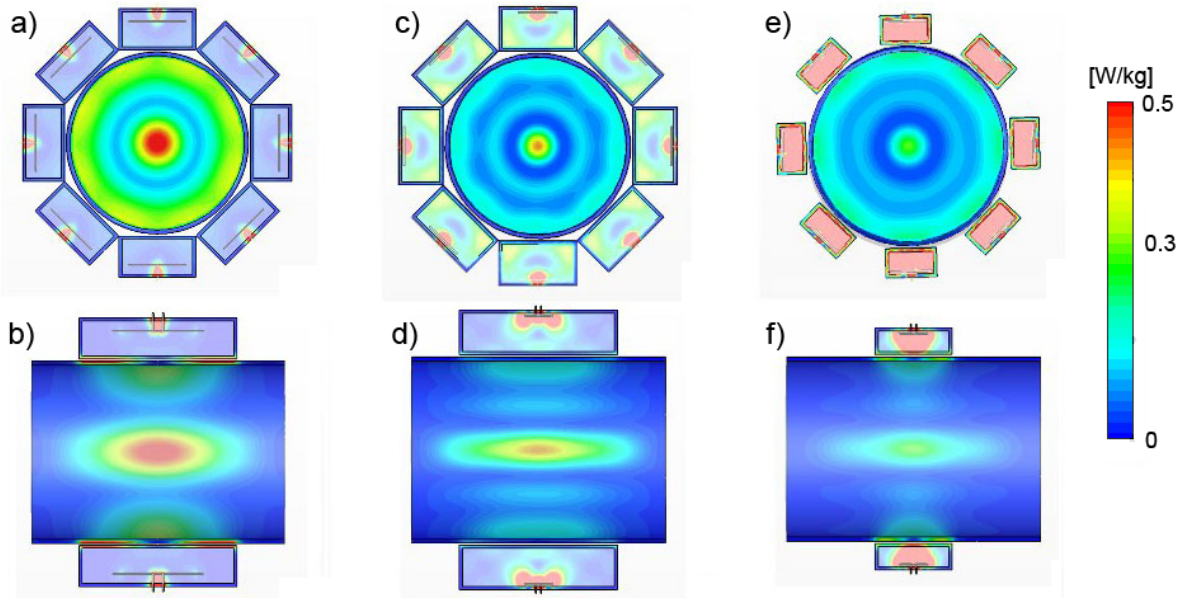

Figure 54: Comparison of the simulated SAR distributions for three 8-channel bow tie dipole antenna configurations. (a-b) Bow tie building block at 298 MHz with dimensions (150 x 70 x 40) mm³, (c-d) Bow tie building block at 500 MHz with dimensions (150 x 70 x 40) mm³ and (e-f) a smaller sized (70 x 40 x 20) mm³ building block at 500 MHz. The local SAR hotspot size in the center of the phantom can be reduced significantly at 500 MHz. A reduction in the length of the dielectric at 500 MHz (e-f) furthermore benefits smaller hotspot dimensions along this axis.

Frequency	Dimensions [mm³]	Max-SAR [W/kg]	iso-SAR 90% [mm³]	iso-SAR 75% [mm³]	iso-SAR 50% [mm³]	iso-SAR 25% [mm³]
300MHz	(150x70x40)	0.54	18x18x41	29x29x70	45x45x111	65x65x157
500MHz	(150x70x40)	0.44	10x10x40	17x17x73	27x27x138	35x35x182
500MHz	(70x40x20)	0.29	10x10x28	17x17x48	26x26x83	25x25x155

Table 4: Comparison of the maximum SAR values and 90%, 75%, 50% and iso-SAR 25% values of the central SAR hotspot in a cylindrical phantom for three 8-element transceiver array configurations at 298 MHz and 500 MHz holding different high permittivity dielectric dimensions.

The 500 MHz antenna building blocks showed reduced hotspot dimensions at 500 MHz vs. 298 MHz. In the axial plane (Figure 54a,c,e) the iso-SAR 90% values are reduced at 500 MHz by 45%, the iso-SAR 75% values by 41%, the iso-SAR 50% values by 40% and the iso-SAR 25% values by 46%. Along the z-dimension in the coronal plane (Figure 54b,d,f) same sized dielectrics (Figure 54a-d) doesn't provide major change in hotspot z-dimension at 500 MHz as expected. The smaller bow tie antenna building blocks (Figure 54e-f) however are able to further reduce the iso-SAR 90% z-component by 30% from 40 mm to 28 mm, the iso-SAR 75% by 34% from 73 mm to 48 mm, the iso-SAR 50% by 40% from

138 mm to 83mm and the iso-SAR 25% by 15% from 182 mm to 155 mm. In total the volume of a cube placed around the max iso-SAR hotspot dimensions can be reduced by 79% for iso-SAR 90%, by 76% for iso-SAR 75%, by 75% for iso-SAR 50% and by 85% for iso-SAR 25% at 500MHz as compared to the 298 MHz setup. On the downside, the max-SAR value of the smaller RF antenna building blocks at 500 MHz decreases by 34%. This result implies that a higher RF power input of the RFPA system needs to be produced to achieve similar absolute temperatures. Furthermore the surface SAR value of the smaller elements increases by a factor of ~2 compared to the bigger dielectrics as demonstrated in Figure 55. This is plausible since the RF antenna is closer to the surface of the phantom and the energy stored per unit volume of the dielectric medium is higher. The surface SAR, which poses an unwanted effect, should be kept to a minimum to avoid undesired heating paradigms. Even though the surface SAR values increase, smaller elements bear the potential to use more elements per unit area which helps to propagate the energy absorption more uniformly over the surface. Smaller elements also help to gain additional degrees of freedom for RF shimming and hotspot steering. However, to demonstrate feasibility and to achieve a fair comparison between 298 MHz and 500 MHz RF heating efficiency, the investigations shown in the remainder of this work make good use of two building blocks with identical dimensions of (150 x 70 x 40) mm³ for the 298 MHz and 500 MHz configurations.

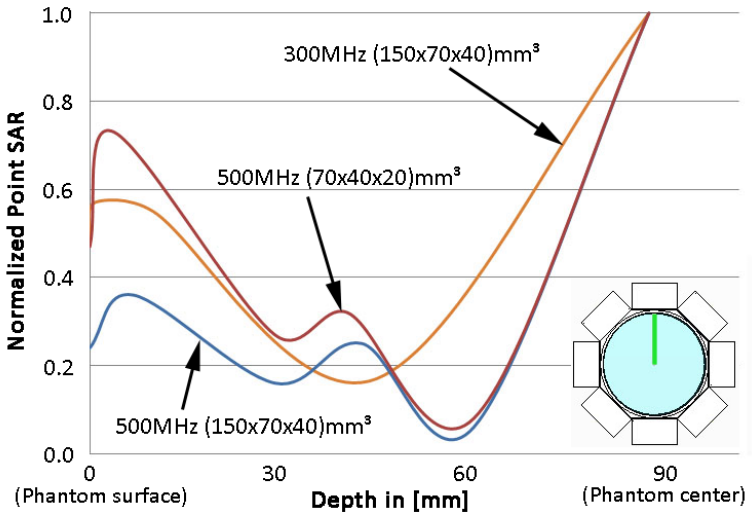

Figure 55: Comparison of the normalized point SAR distribution along a central line (marked in green in the inlay showing the setup) through the phantom of an 8-channel bow tie applicator at 298 MHz (orange line) with a dielectric size of (150 x 70 x 40) mm³ vs. an 8-channel applicator at 500 MHz with the same sized dielectric (blue line) and an 8-channel applicator at 500 MHz with a dielectric size of (70 x 40 x 20) mm³ (red line) [227].

To gain insight into the RF distribution in a model closer to the *in vivo* scenario than the uniform phantom setup presented in Figure 54, the human head of the voxel model “Ella” from the virtual family [109] was chosen. This head model, derived from a healthy volunteer, offers heterogeneous

electromagnetic tissue properties, which allow for the modeling of complex EM behavior and wave propagation. Furthermore the tissue dependent blood perfusion and metabolic heat rate can be specified according to Equ. (61). Electromagnetic and temperature simulations were performed with a spatial mesh resolution below (2 x 2 x 2) mm^3. Electromagnetic parameters (permittivity, conductivity) of tissue were adjusted to the investigated frequency [103-105]. Thermal parameters (heat capacity, thermal conductivity, density, blood perfusion) were specified as recommended by [228]. A blood flow coefficient of 10 $kW/(Km^3)$ and a basal metabolic rate of 127 W/m^3 was chosen for the carotid and cerebral arteries. Thermal conductivity, permittivity and perfusion changes during the time course of RF heating were not modelled. To allow i) a comparison with the phantom simulations, ii) to improve electromagnetic coupling to the head and iii) to cool down the surface of the head a cylindrically shaped object with tissue equivalent properties ($\varepsilon = 50, \sigma = 0.55\ S/m$) was placed around the head as shown in Figure 56. The cooling temperature of the cylinder was set to a constant 20°C for the simulation period. An RF pulse to induce heating was applied after the initial steady state blood temperature of 37°C was homogeneously distributed over the entire head. The input power for the eight antennas was 50 W per channel for 5 minutes, resulting in a total of 400 W accepted input power at the antenna ports. A 0° phase difference between channels was employed to generate a hotspot in the center of the brain. The results are illustrated in Figure 56 which shows an axial (Figure 56a), a sagittal (Figure 56b) and a coronal (Figure 56c) slice positioned in the brain layer of the maximum temperature increase.

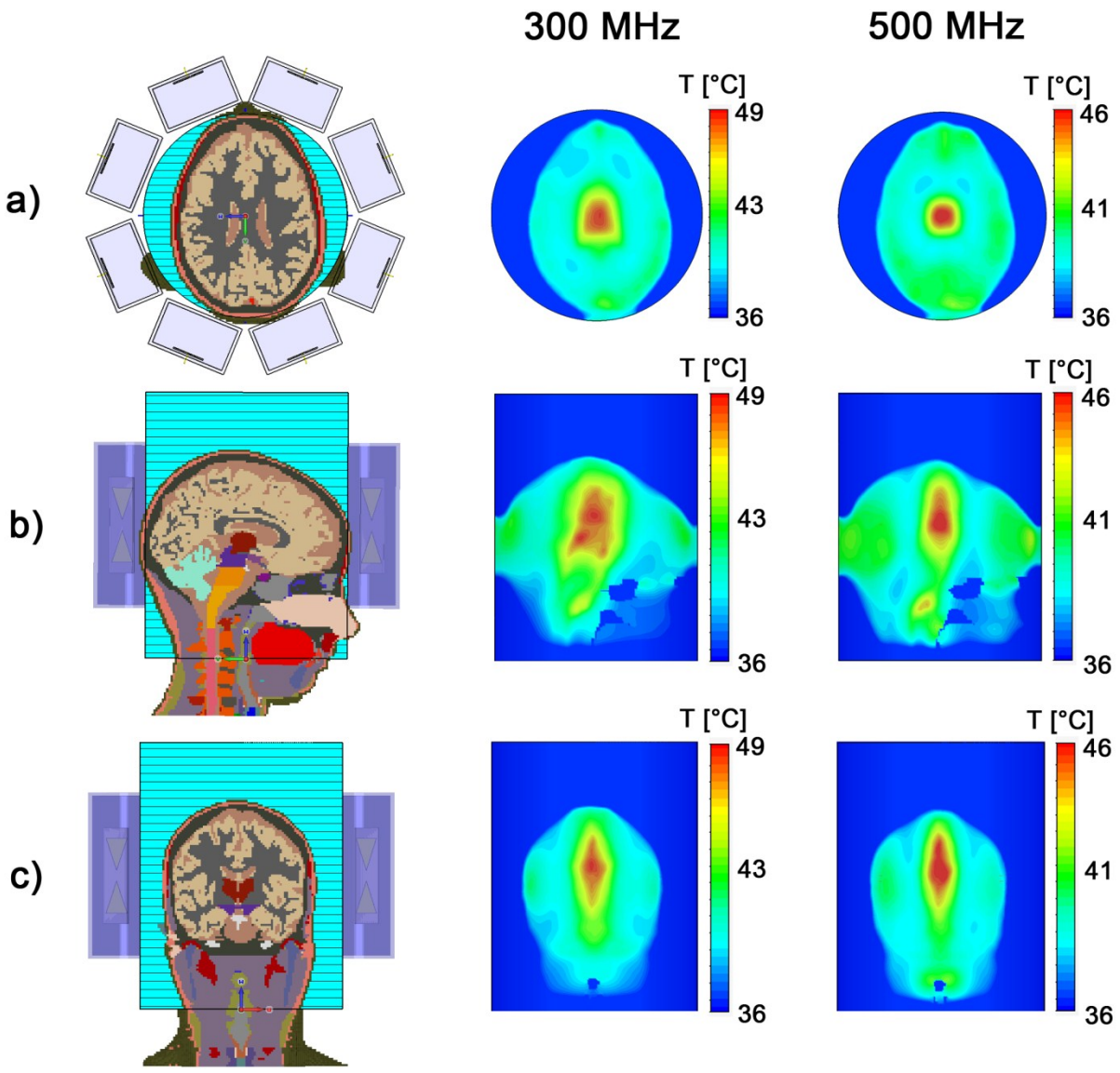

Figure 56: Results from temperature simulations in an (a) axial, (b) sagittal and (c) coronal view of an 8-channel bow tie dipole targeted RF heating applicator at 298 MHz (middle) and 500 MHz (right). The phase setting was adjusted (no phase delay between channels) to generate a temperature hotspot in the center of the brain of voxel model "Ella" from the virtual family. RF heating was performed for 5 minutes with an input power of 50W per antenna, resulting in a total of 400W [109].

For the 298 MHz antennas a temperature of more than 49°C in the center of the hotspot was reached. For the 500 MHz setup, the maximum temperature increase was in the range of 46°C. These experimental results are in agreement with the simulations performed in the phantom configuration, where the absolute power inside the phantom was reduced by ~20% for the 500 MHz setup versus the 298 MHz setup as depicted in Figure 54. On the other hand the hotspot size and specificity of the hotspot area is decreased – as expected when designing the experiment – in the 500 MHz setup. The iso 90% temperature area of the 500 MHz is as small as (13x16x37) mm^3, whereas for the 298 MHz case the iso 90% temperature area is (19 x 23 x 32) mm^3. Placing a bounding box around the iso-SAR

curves would consequently result in a reduction in iso-Temperature 90% hotspot volume of 45%. Decreasing the size of the antennas along the z-direction may further reduce the hotspot volume as highlighted by the results obtained from the simulations using the phantom setup. For the 298 MHz and 500 MHz configurations, the surface temperature was below 43°C. This result indicates that a selective RF heating is feasible with the proposed approach; even for an *in vivo* situation. The results also showed that higher RF frequencies might enhance the temperature hotspot selectivity.

Further to the assessment of the RF heating performance of the 8-channel bow tie antenna configurations, an assessment of the MRI capabilities at 11.7 T versus 7.0 T were performed. The results are summarized in Figure 57. For an in-phase phase setting, simulations of two antenna configurations at 298 MHz and 500 MHz together with the voxel model "Ella" from the virtual family [109] show an expected drop in transmit efficiency when moving to 500 MHz. At 7.0 T B_1^+ was found to be 13.9 ± 2.2 µT/√kW (avg ± std). In comparison at 11.7 T B_1^+ was reduced by 31% to 9.6 ± 2.1 µT/√kW. Nevertheless the simulated B_1^+ at 11.7 T showed intriguing transmission field levels per RF power even versus current state-of-the-art RF hardware used at lower frequencies (f = 400 MHz, B_0 = 9.4 T) [125]. These results render the proposed bow tie antenna building blocks a suitable candidate for transmit/receive arrays tailored for B_0=11.7 T.

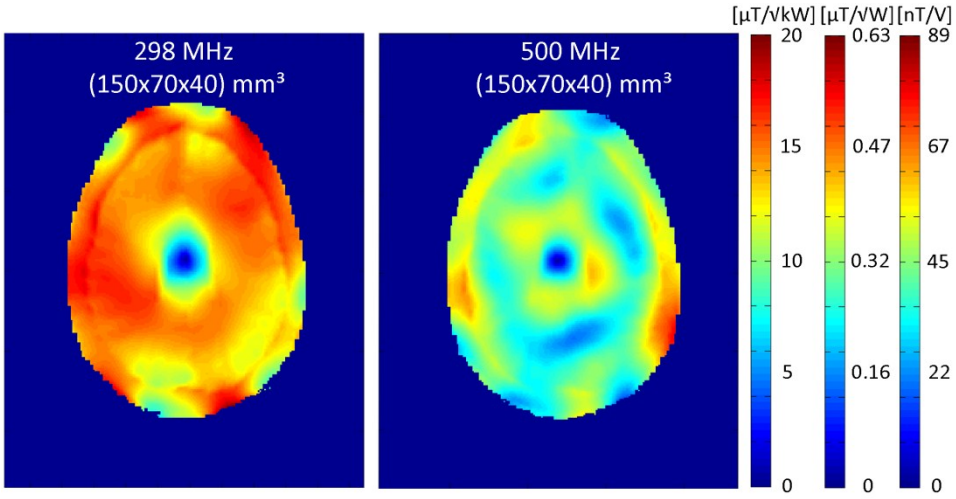

Figure 57: Comparison of the simulated B_1^+ distribution of an 8-channel bow tie applicator at 298 MHz (left) and at 500 MHz (right). For convenience the three most common used transmit efficiency units ([µT/√kW],[µT/√W],[nT/V]) are plotted with their corresponding color scale. An axial slice of the brain of voxel model "Ella" is depicted together with an in-phase (0° phase delay between channels) RF shim setting. B_1^+ decreases at 500 MHz when compared to 298 MHz for the same input power.

6.1.2 External RF Power Transmission Unit

To validate the results derived from the numerical simulations, RF heating experiments were performed using an RF frequency of 500 MHz. Since B.U.F.F. is not equipped with a 11.7 T MR system, MR imaging experiments were constrained to 7.0 T. Targeted RF heating experiments at 500 MHz were conducted using a custom built external power source (PTB, Berlin, Germany). The measurement setup, shown in Figure 58, consisted of a signal generator with a frequency bandwidth of 9 kHz-1 GHz (1020.2005.52, Rhode & Schwarz, München, Germany), two power reflection meters (Rhode & Schwarz, München, Germany) and two broadband (100 MHz-500 MHz) class A linear RF power amplifiers modules (LZY-1, Mini-Circuits, New York, USA). The power monitoring is essential to track systemic changes indicated by RF reflection losses in the RF heating setup which could lead to excessive uncontrolled heating in any of the components in the RF-chain. Since the external RF power transmission module consists of magnetic components, it was located in the operator room outside of the magnet room. Long coaxial cables were used to connect the power source to the RF antennas. A schematic diagram (Figure 58) outlines the experimental setup with the power of each RFPA feeding channel being divided by two 1-by-4 power splitters (D5400-10, Werlatone Inc., New York, USA) to equally split the input signal to eight individual RF antennas at 500 MHz. Simultaneously, an MR imaging RF coil was connected to the 7.0 T MR system for MR thermometry acquisitions at 298 MHz. The RF power amplifier features a built in blanking circuit to prevent the 500 MHz signal being played out during MR acquisitions. At 500 MHz RF losses are becoming considerably high. The loss tangent scales proportional to the frequency, while metal losses due to the skin effect scale only with the square root of frequency [229]. For coaxial cables however, the skin effect on inner and outer conductor is the predominant source in our investigated frequency range leading to an increase in loss by ~0.5 the power of frequency [229]. On the other hand for dielectric materials as used in our RF antennas, power losses due to an increased loss tangent need to be considered. In our measurement setup long distance cables were needed to bridge the external transmission unit, which is not compatible to be operated close to the MR magnet, and the RF antennas. For a single channel the losses at 500 MHz from the RFPA to the RF antennas mounted to -2.2dB (cable 5 m = -0.7dB, cable 6 m = -0.9dB, 1-by-4 power splitter = -0.6dB per channel), which is equivalent to a loss of ~40% in power.

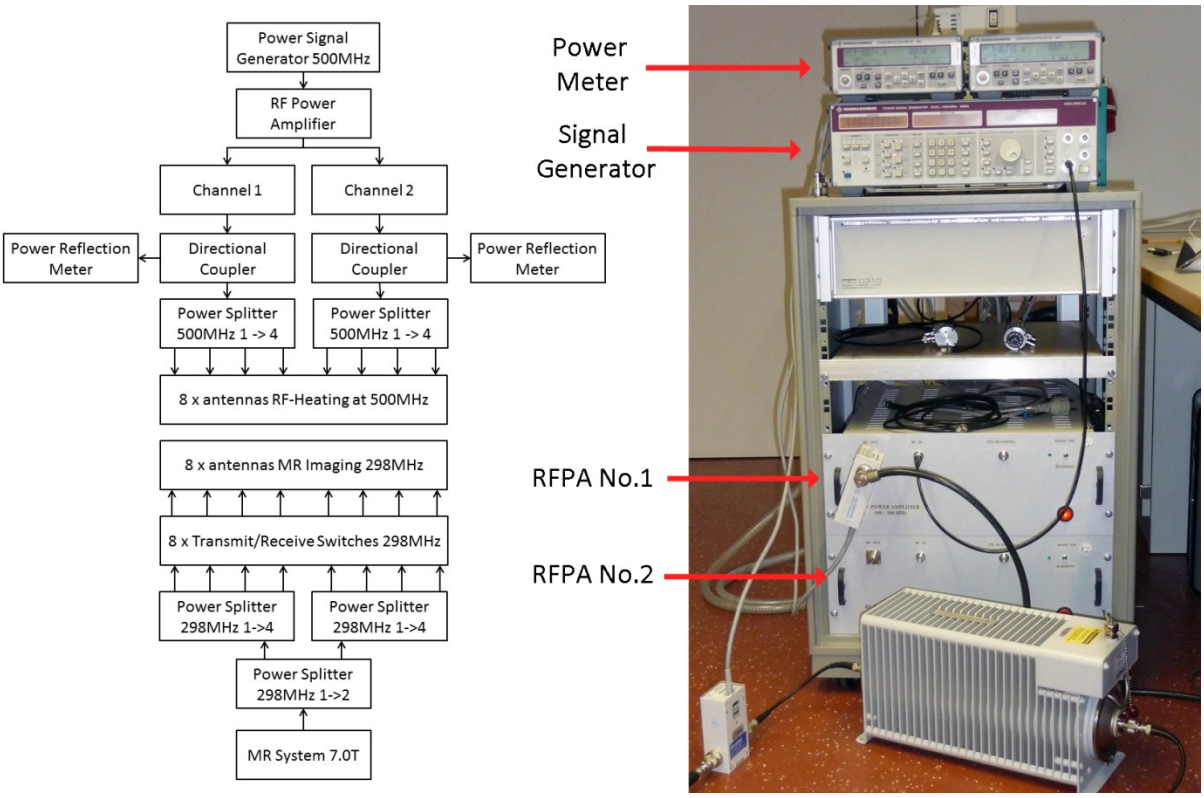

Figure 58: Flowchart (left) of the external RF power transmission concept customized for RF heating experiments at 100-500 MHz. This setup was used to drive an 8-channel applicator at 500 MHz (11.7 T). MR imaging was performed at 298 MHz (7.0 T). Picture photograph of the external RF power transmission unit (right), including a signal generator, two power reflection meters and a two-channel broadband RFPA (PTB, Berlin, Germany).

6.1.3 Experimental Results for Single Channel RF Heating at 500 MHz

To validate the simulations and to test the RF antennas and the external RF power transmission unit, single channel RF heating experiments were performed. A single bow tie dipole antenna (150 x 70 x 40) mm³ at 500 MHz was used for RF heating in a custom made cylindrical phantom (diameter = 172 mm, length = 250 mm, σ_1 = 0.72 S/m, ε_1 = 75) and compared to the simulation setup as demonstrated in Figure 59. The RF heating and simulation duration was 12 minutes with an input power of 70 W. In this particular experimental setup the cable losses accounted to -2.7dB, resulting in a required power output of 130 W at the RFPA to reach 70 W at the antenna. To acquire MR temperature distribution maps, the setup was placed inside a birdcage volume RF coil (Siemens Healthcare, Erlangen, Germany). The results showed a maximum temperature increase of >15°C in the simulations and in the measurements (Figure 59). Along a line through the center of the phantom the temperature difference between simulations and measurements is below 2°C, which suggests a good agreement between the simulations and experimental reality.

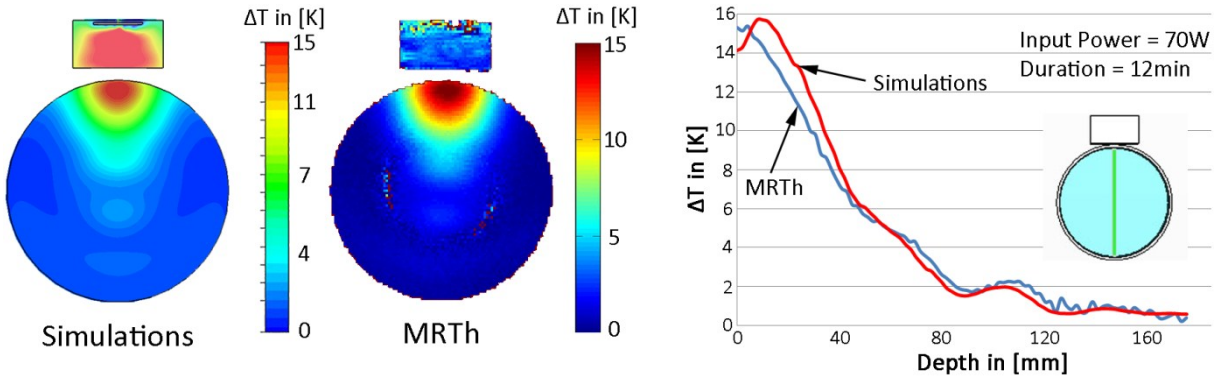

Figure 59: Comparison of the results of the simulated temperature distribution (left) of a single antenna driven at 500 MHz in an axial slice of a cylindrical phantom versus MRTh measurements (middle) for 70W input power and a RF heating duration of 12 minutes. MR thermometry was conducted with the PRFS method using a dual gradient echo technique (TE1 = 2.26 ms, TE2 = 6.34 ms) with a resolution of (1.9x1.9x5) mm³ [39]. B_0 drift (0.02 ppm/h) was compensated using a vegetable oil sample [17]. Relative temperature distribution (ΔT) (right) along a central line (marked in green in the inlay showing the setup). A good agreement could be achieved between temperature simulations (red line) and MRTh (blue line).

6.1.4 Multichannel RF Heating at 500 MHz in Conjunction with Multichannel MRI at 298 MHz

For the single channel RF heating experiments a birdcage RF coil with a diameter of 345 mm was used to acquire the MR temperature maps. Arguably, this setup is suboptimal for multichannel heating experiments since the RF shield of the birdcage RF coil is in close proximity to the RF antennas, which influences the electromagnetic field distribution inside the phantom. Also, a birdcage RF coil supplied by a single feeding channel is suboptimal for UHF MRI of larger objects due to B_1^+ inhomogeneities and furthermore lacks any B_1^+ shimming capabilities. The influence of the RF shield on the RF heating pattern is illustrated in Figure 60. When benchmarked against a setup without an RF shield (Figure 54) the SAR intensity in the center of the phantom drops by factor of ~2 when surrounding the 8 bow tie elements with the RF shield of the birdcage RF coil (Figure 58). Also, for this RF shield configuration two additional hotspots are formed due to resonant behavior along the z-axis of the phantom as demonstrated in Figure 60c.

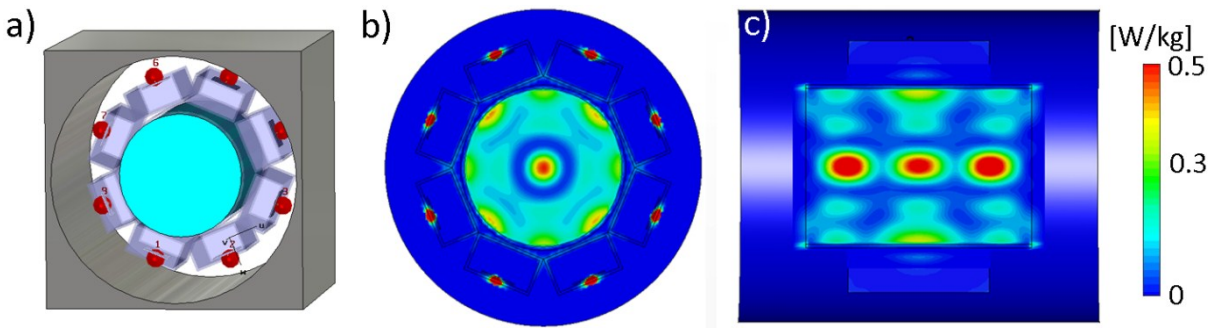

Figure 60: (a) Positioning of an 8-channel bow tie antenna setup at 500 MHz in a MR imaging birdcage RF coil shield equivalent for EMF simulations. (b) Axial and (c) sagittal view of the simulated SAR distribution inside the phantom in the presence of the RF shield.

A solution to this problem is the replacement of the birdcage RF coil with custom made local MR imaging elements at 298 MHz. Certain design criteria need to be fulfilled to seamlessly integrate additional multichannel elements in the existing RF heating setup.

1) The EM field distribution in the center of the phantom of the 500 MHz antennas should not be affected.
2) Surface SAR levels should not be elevated due to the placement of additional MR imaging elements.
3) B_1^+ levels should be sufficient to acquire MRTh data.
4) Decoupling between MR imaging elements should be sufficient to allow for B_1^+-shimming.

A fairly good decoupling (<-15dB) between individual RF antennas due to the high permittivity dielectrics allows the placement of additional 298 MHz elements in between the 500 MHz RF antennas. The field distribution should not be altered significantly if the 298 MHz element is not meeting resonance conditions at 500 MHz. Since the E-field vector is oriented along the length of the dielectric in z-direction, an additional RF antenna that generates an E-field distribution along the same direction would couple to the dielectric leading to wave propagation through the dielectric medium and eventually in the phantom. This concept, which is similar to the concept of multi-feed dielectric resonator antennas [230], can be used for UHF MRI at 7.0 T and targeted RF heating at 500 MHz. The simplest element to generate such a field distribution is a dipole antenna positioned along the z-direction. However, placing a $\lambda/2$-electric dipole in air results in a dipole length of ~50cm at 298 MHz. Although the effective antenna length is modestly shortened by the presence of the deionized or heavy water dielectric from the adjacent 500 MHz bow tie building blocks and the high permittivity properties of the phantom, such antenna length would still be fairly long versus the region of interest. To shorten the physical antenna length, meander shaped electric dipole antennas

which comprise a total length of 11.8 cm were designed and integrated in the 500 MHz targeted RF heating setup as shown in Figure 61. In total eight of these additional RF antennas were built and used. The imaging capabilities and B_1^+ field distribution of the 298 MHz meander shaped dipole antenna array are shown in Figure 62.

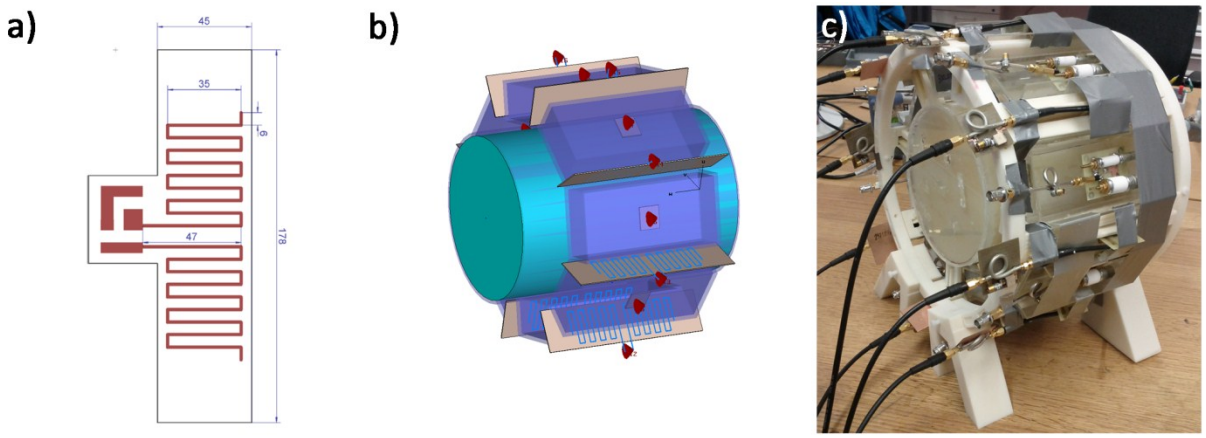

Figure 61: (a) Schematic design and dimensions of the proposed meander antennas used for integration in the 8-channel targeted RF heating applicator at 500 MHz. Simulation (b) and experimental setup (c) of an eight channel meander dipole antenna array at 298 MHz together with an eight channel bow tie RF heating applicator at 500 MHz.

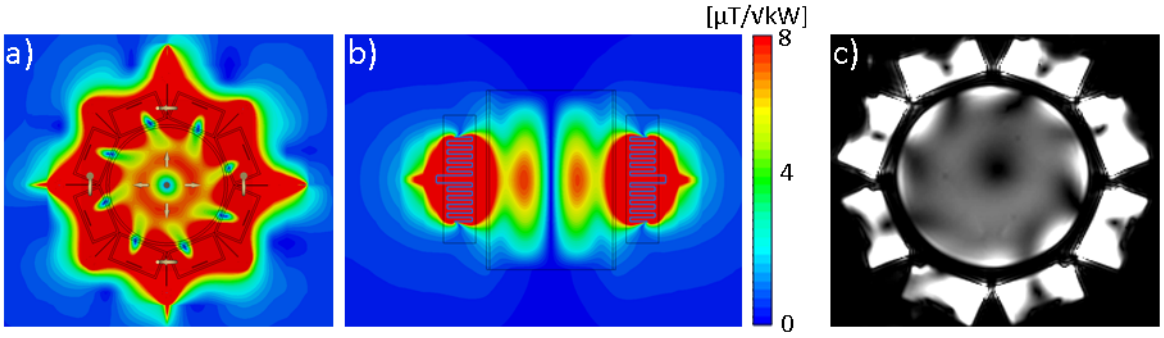

Figure 62: (a) Central axial plane and (b) central sagittal plane of the simulated transmission field distribution of the 8-channel TX/RX meander dipole array in a cylindrical phantom. (c) MR imaging capabilities of the 8-channel meander dipole antennas. Imaging parameters: 2D gradient echo, TE = 4 ms, TR = 8.6ms, FoV = (300 x 300) mm², in-plane resolution (1.2 x 1.2) mm², slice thickness = 8 mm. Please note that for the 500 MHz RF antennas deionized water was used instead of D_20, which has similar electromagnetic properties but can be visualized at 298 MHz.

The imaging capabilities of this array yielded a maximum B_1^+ of $14.9\ \mu T/\sqrt{kW}$ and a mean value of $7.0 \pm 2.1\ \mu T/\sqrt{kW}$ for the central axial slice of the phantom (Figure 62b). While these levels of B_1^+ of

the proposed 8-channel meander antennas are inferior to the 298 MHz bow tie antennas introduced earlier (~$17\mu T/\sqrt{kW}$ in the human brain), the goal to reach sufficient B_1^+ for MRI could be met. Since the meander antennas are narrow band antennas, no major coupling is expected between the 298 MHz and the 500 MHz elements. The simulated influence of the meander antennas on the E-field distribution used for RF heating at 500 MHz is minor as demonstrated in Figure 63. For a simulation setup equipped with the meander antennas the SAR hotspot size and magnitude in the central and surface regions remains similar to a simulation setup without the extra meander antennas.

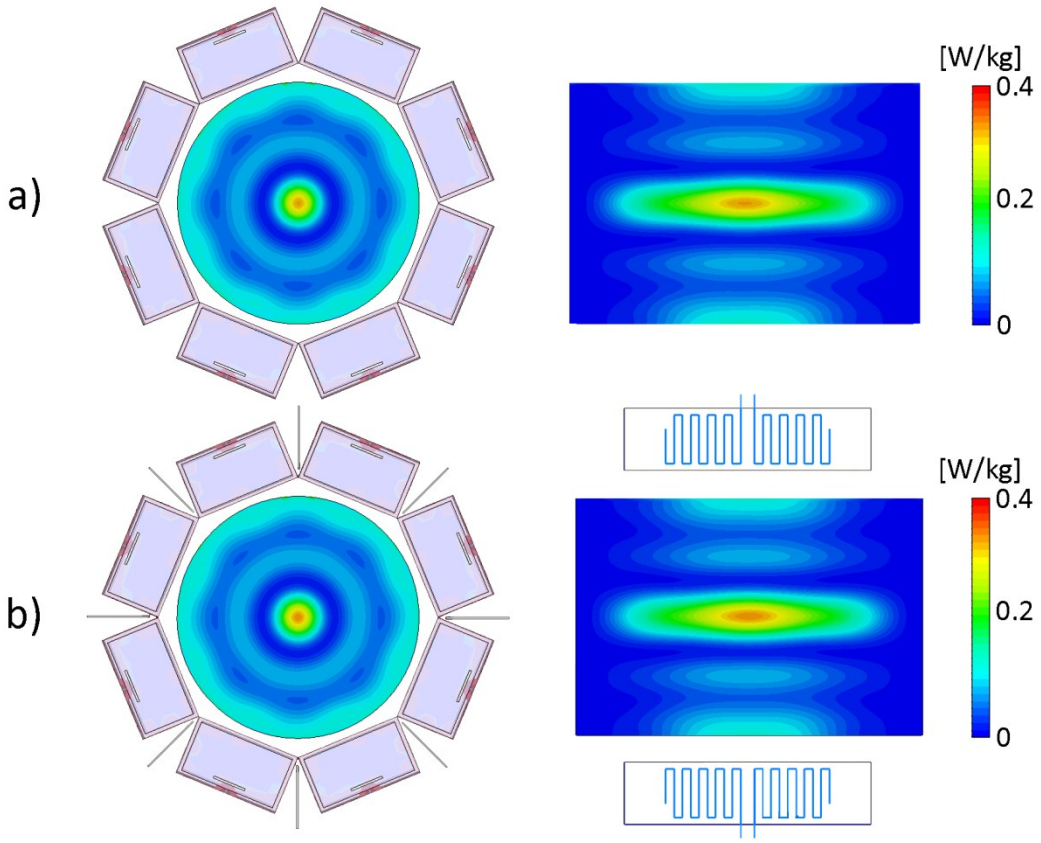

Figure 63: (a) Simulated point SAR distribution produced by an 8-cahnnel bow tie dipole applicator for 1W accepted input power at 500 MHz RF frequency in an axial (left) and coronal (right) central slice of a cylindrical phantom. (b) In comparison, the SAR distribution of the same 500 MHz antennas with an meander dipole antenna positioned between two bow tie antennas resulting in a total of 8 meander dipole antennas. Please note that no major differences in the SAR distribution were found due to the presence of the meander dipole antennas.

The proposed concept of nesting meanders can be transferred to the 298 MHz bow tie building blocks [65, 225] in order to increase SNR and parallel imaging performance. At 298 MHz however, a resonance condition is met between the transmitting path of the bow tie dipole antennas [65] and the meander antennas, both tuned to 298 MHz. This constraint may influence the field distribution as illustrated in Figure 64, even for low coupling values (-13dB). B_1^+ decreases directly below the tuned

meander antenna as can be seen in Figure 64b while at the same time SAR_{10g} increases by a factor of ~2 at the surface of the phantom [231]. Here, an active or passive detuning circuit is able to reduce the influence of the meander antennas on the H-field distribution for imaging and the E-field distribution for RF heating as illustrated in Figure 62. Ultimately, more receive elements can be used with an increase in SNR and parallel imaging performance without performance penalties for targeted RF heating [231].

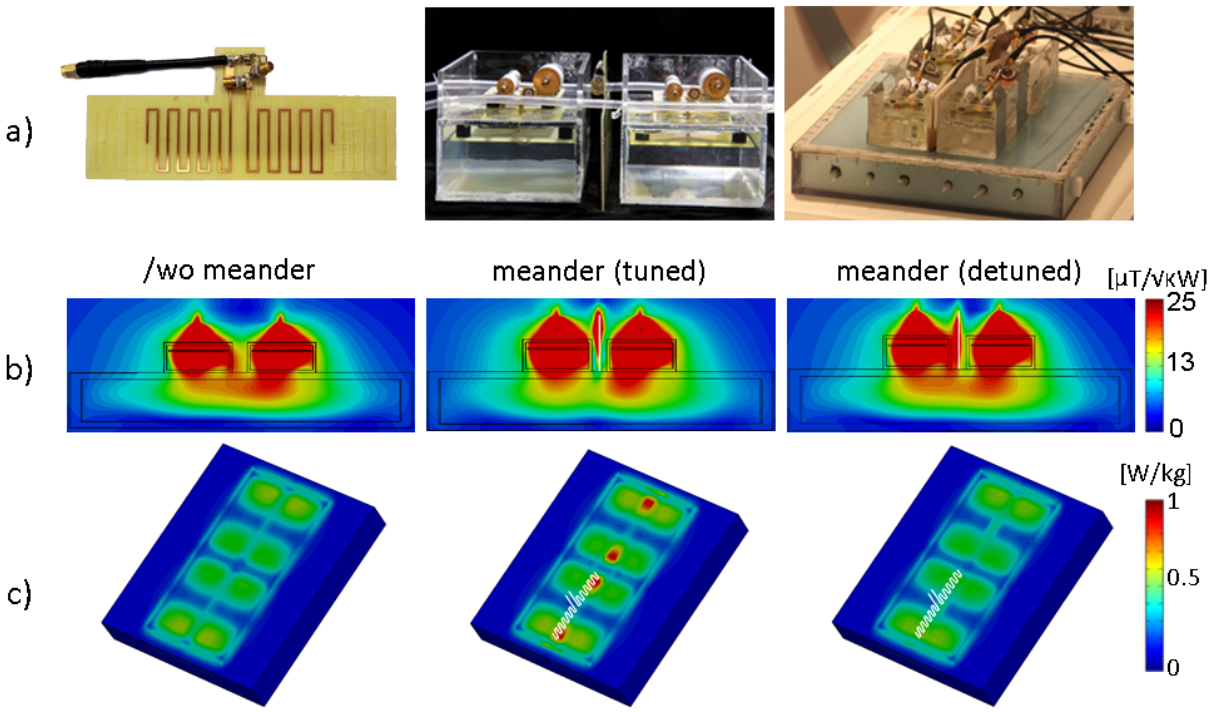

Figure 64: a) Meander antenna design for 7.0 T MR imaging (left), positioning of the meander antenna in between two bow tie dipole building blocks (middle) and experimental setup of four bow tie dipole building blocks together with two nested meander antennas (right). b) Simulated B_1^+ distribution along an axial plane through the middle of two bow tie dipole antennas only (left), with a nested meander configuration and no decoupling (middle) and with a nested decoupled meander configuration (right). c) 3D projection of the SAR distribution of the four bow tie dipole building blocks without meander antennas (left), with two nested meander elements without decoupling (middle) and with two nested meander elements with decoupling (right) [231].

The additional meander elements are not necessarily limited to MRI imaging applications only but can be potentially also be utilized for transmission. If the meander antennas are operated at a frequency of 298 MHz and the bow tie antennas at another frequency that avoids coupling (e.g. 500 MHz), an operation of dual frequency RF heating becomes feasible. Multi-frequency heating enables new degrees of freedom in altering the RF distribution inside the object. The temperature hotspot size is depending on the RF wavelength used and can be altered in size using multiple

frequencies. The RF heating hotspot of the meander antennas operated at 298 MHz is presented in Figure 65. Its dimensions are (17 x 17 x 46) mm³ for iso-SAR 90%, (28 x 28 x 74) mm³ for iso-SAR 75%, (44 x 44 x 115) mm³ for iso-SAR 50% and (63 x 63 x 160) mm³ for iso-SAR 25%. The hotspot can potentially be steered to a deliberately chosen region by changing the phase settings (Ch1 = 0°, Ch2 = 45°, Ch3 = 180°, Ch4 = 225°, Ch5 = 0°, Ch6 = 225°, Ch7 = 135°, Ch8 = 45°). Double frequency heating using nested dipoles can potentially be performed without the need for an external transmitter. One could imagine using e.g. ^{1}H (298 MHz) and ^{31}P (121 MHz) frequencies for targeted RF heating, which are both supported by the RFPA of the MR system. At the same time MR imaging can be performed for all the nuclear spin excitation frequencies supported by the RFPA. Obviously, ^{1}H MRI could be supplemented by ^{1}H MR spectroscopy (MRS) which can be used for metabolic probing during RF heating based therapy. The proposed dual frequency approach would even pave the way for therapeutic monitoring using heteronuclear MRI and MRS (^{31}P MR, ^{23}Na MR etc.).

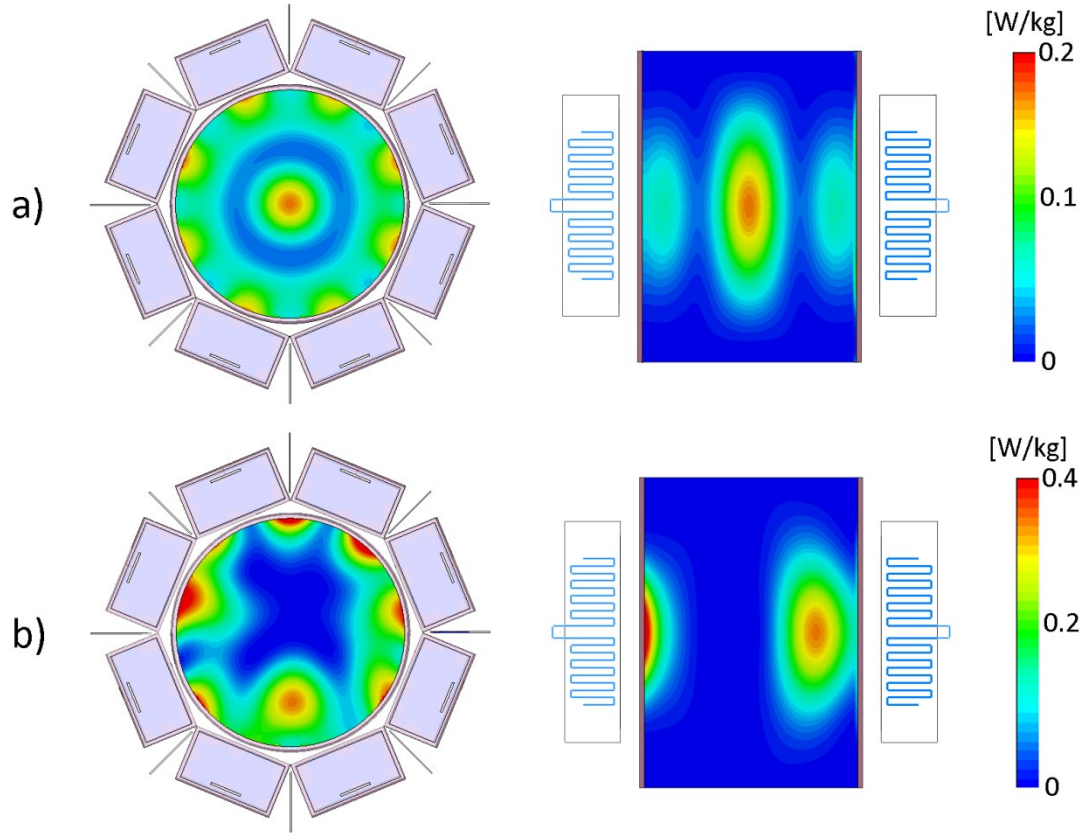

Figure 65: (a) Point SAR distribution for 1 W input power of eight nested meander elements at 298 MHz excited in-phase (0° phase difference between individual channels) to generate a central hotspot in the phantom in an axial (left) and sagittal view (right). (b) Demonstration of phase steering of the nested meander antennas to deliberately change the SAR hotspot location.

To summarize, higher frequencies yielded a decrease in the temperature hotspot size in the phantom and in the human voxel model. With the proposed dual frequency setup first RF heating experiments

were successfully performed with a transmission frequency of 500 MHz while MRI was performed at 7.0 T for MR thermometry. An 8-channel RF heating applicator tailored for 500 MHz was combined with an 8-channel transmit/receive array customized for operating at 298 MHz. This double tuned configuration enabled targeted RF heating experiments with an external power transmission unit, while MR thermometry and MRI was performed at 7.0 T. This setup also facilitates multiple frequency targeted RF heating patterns, which can be put to use to improve the management and control of RF distribution and induced temperature distribution.

6.2 Electrodynamic Constraints for Targeted RF heating and Imaging (f>1GHz)

To further push the envelope and to investigate the performance of even higher frequencies, EMF simulations were conducted for frequencies f>1GHz. This move might be counterintuitive at first glance since the larger the frequency the more pronounced is the power absorption at the surface. While this holds true for a single RF antenna, a multi-channel array is capable of distributing the energy absorption over the surface or entry area of the object with the poynting vector being directed towards the target, which might afford sufficient RF energy levels at depth. The simulation setup used a frequency of 1.44 GHz and consisted of a uniform cylindrical phantom (l = 250 mm, r = 90mm) with material properties ε = 45 and σ = 1.0 S/m, which resembles grey matter (σ = 1.2 S/m, ε = 51) and white matter (σ = 0.77 S/m, ε = 38) at 1.44 GHz [103]. An advantage of the high frequency used is the short wavelength in air of ~21 cm. At such wavelength a λ/2 dipole antenna has length of about 10 cm. Such compact design facilitates RF antenna placement in air without the need of a high permittivity dielectric to further shorten the antenna length. In total 18 rectangular strip dipole antennas were positioned equidistantly around the cylindrical phantom to direct the RF energy towards its center, as shown in Figure 66a.

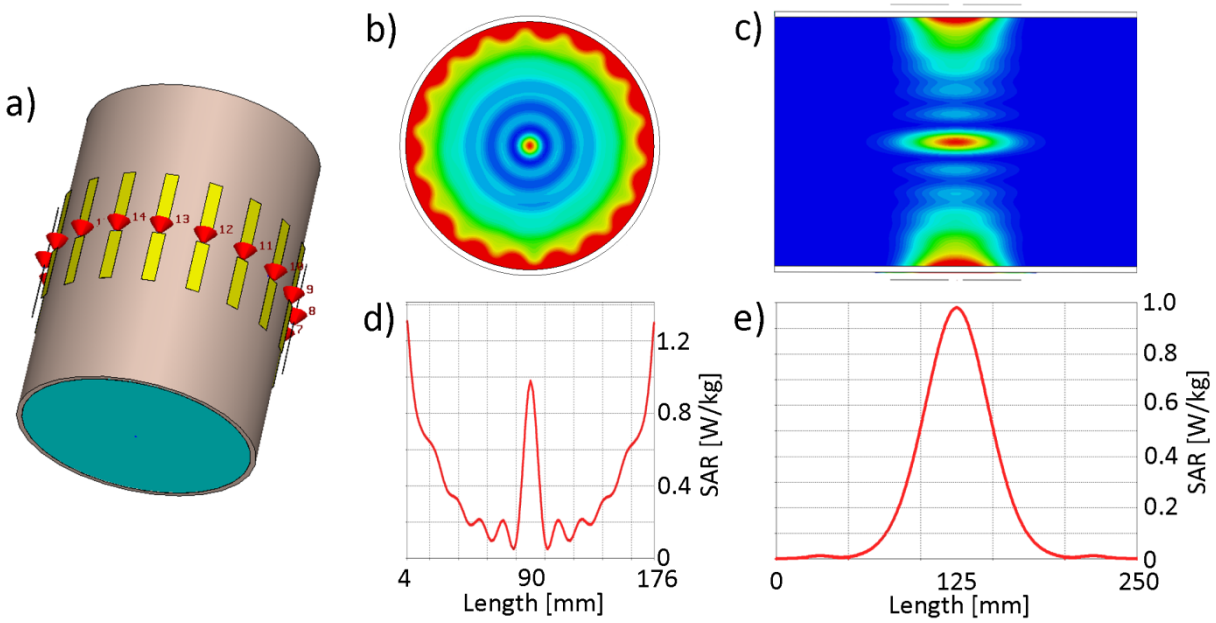

Figure 66: (a) Simulation model of an 18-channel rectangular dipole antenna array positioned around a cylindrical phantom with a transmission frequency of 1.44GHz. Point SAR distribution for 1 W of input power in an axial (b) and a coronal (c) view of the phantom, together with line plots of the SAR distribution along a horizontal line in the axial (d) and coronal (e) view.

The results of the EMF simulations and the successive SAR calculations are illustrated in Figure 66b-d. The 18 dipole antennas are able to generate a SAR hotspot in the center of the phantom with a maximum SAR value of 0.98 W/kg for 1 W of input power, which falls slightly below the maximum SAR values at the surface (1.3 W/kg) of the phantom. The dimensions of this hotspot are significantly reduced versus the frequencies investigated throughout this study. The 1.44 GHz setup provided iso-SAR 90% values as small as (4 x 4 x 20) mm^3, iso-SAR 75% of (7 x 7 x 32) mm^3, iso-SAR 50% of (11 x 11 x 52) mm^3 and iso-SAR 25% of (16 x 16 x 74) mm^3. The results demonstrate that although high power absorption at the surface occurs, EM field interferences in the center of the phantom (Figure 66b-d) show regions with high SAR due to constructive interferences of multi-channel power transmission. To this end sufficient power transfer indicating adequate E-field magnitudes at the center of the phantom could be shown that has also implications for the H- or B-field, which is linked to the E-field in time and space by Maxwell's equations. To draw the line between the SAR simulations and MRI at 1.44 GHz B_1^+ maps were calculated for proton spin excitation at 33.8 T. The results for phantom and *in vivo* simulations are shown in Figure 67c with a maximum B_1^+ of ~13 µT/√kW in the center of the thigh of the human voxel model "Duke" from the virtual family [109].

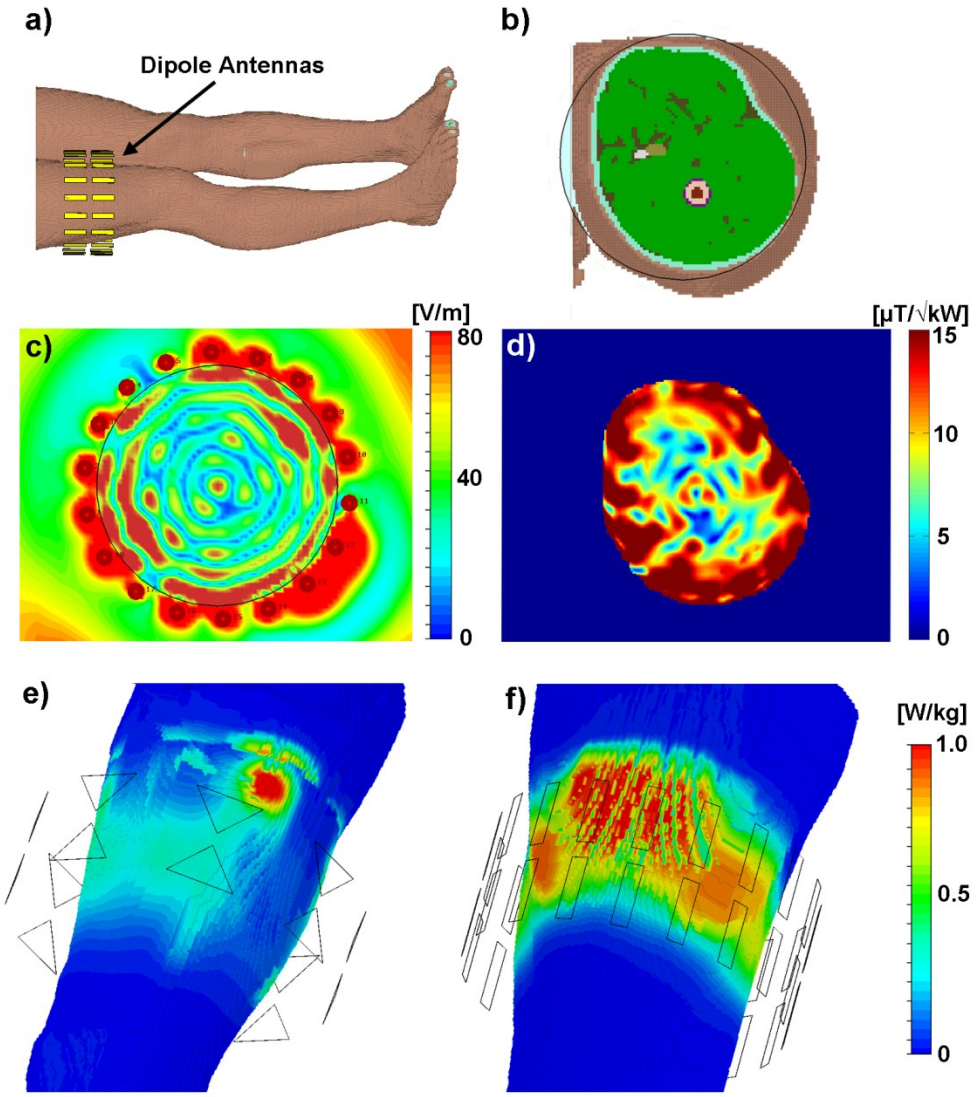

Figure 67: (a) Antenna location and (b) axial view of the thigh of a human voxel model at 1.44 GHz surrounded by an 18-channel transmit array. The array consists of rectangular dipole antennas positioned circularly (diameter = 190 mm) around the leg of the human voxel model "Duke" from the virtual family [109]. (c) Time point (phase = 90°) of the E-field distribution to demonstrate the circular wavelike transmission pattern that results in constructive interferences in the center of the leg. (d) Simulated B_1^+ distribution in the human thigh at 1.44 GHz of the 18-channel dipole transmit array. In the center of the phantom maximum B_1^+ of around 13 µT/√kW was achieved. SAR_{10g} distribution in the human thigh of (e) an 8-channel bow tie dipole array at 298 MHz in comparison to (f) the 18-channel dipoles at 1.44 GHz for the same total input power of 1 W. Maximum local SAR_{10g} values are in both configurations 1.3 W/kg, however the power distribution of the 1.44 GHz setup is distributed more evenly across the surface.

Next to MRI, another implication of these findings can be deduced for EPR, which operates with frequencies 658 times higher for electron spin excitation than used for nuclear spin excitation (Equ. (12)). So far textbook knowledge and published data considers *in vivo* EPR imaging being constrainted since "…too much energy would be deposited in human bodies, if electron spins were 'excited' by

these rf fields." (Haacke et al. [20], p. 25) and therefore "…frequencies that are suboptimal for EPR (usually<1200 MHz) need to be used." (Gallez et al. [18], p. 223). Interestingly, the preliminary simulation results outlined in Figure 67 show an average B_1^+ of 11.6 ± 4.6 µT/√kW in the thigh of a human voxel model using an 18-channel rectangular dipole array for transmission. More interestingly, constructive interferences of the RF fields in the center of the imaging object render B_1^+ values of 13 µT/√kW feasible at this deep lying position. At the same time in this particular example SAR_{10g} levels are not enhanced at 1.44 GHz as compared to 298 MHz (Figure 67d-e). Both scenarios – namely 298 MHz and 1.44 GHz – have a maximum local SAR_{10g} of 1.3 W/kg for 1 W of input power. However the RF power deposition is distributed more evenly across the surface at 1.44 GHz due to the discussed capabilities of the proposed multi-channel RF antenna setup. The preliminary results forwarded in this work suggest that further research into RF antenna design will certainly pave the way for exploring new territory and will help to break ground for targeted RF heating, EPR and MRI in the GHz range.

Discussion & Conclusions

The presented work demonstrates the basic feasibility of combining RF hyperthermia therapy and MR imaging by using the trait of magnetic resonance in the short wave length regime. En route to this achievement RF coil arrays were designed, constructed, evaluated and ultimately applied in cardiac and brain imaging at 7.0 T [57, 93-95]. The lessons learned from this precursor were employed to develop the physical, conceptual and technical underpinnings of an 8-channel hybrid transmit/receive applicator that runs at the 7.0 T proton MR frequency and that supports targeted RF heating, MR imaging and MR thermometry [65]. Unlike previous approaches, where an MR system is combined with an extra RF heating setup running at a different frequency [9, 11, 14], the approach proposed here makes additional RF hardware (RF power amplifiers, RF electronics, filters, RF heating antennas) or software to drive these components obsolete. The proposed hybrid applicator (i) can be used together with commercially available ultrahigh field MR systems equipped with single feeding channel or with multi-channel transmit configurations and (ii) supports diagnostic and interventional applications. Since local multi-channel transmit/receive antennas are used, signal-to-noise ratio and parallel imaging performance are enhanced as compared to a volume resonator [9, 57, 232] and hence provides means for high spatial and temporal MR temperature mapping during RF heating interventions. MR imaging capabilities at 7.0 T of the proposed bow tie antennas were demonstrated for high spatial resolution *in vivo* brain imaging [65] and for high spatial resolution *in vivo* cardiovascular imaging, in particular 2D CINE FLASH [65, 225], steady state free precession (SSFP) [116], rapid acquisition with relaxation enhancement (RARE) [118, 223], 3D fat-water separation [233], T_2^*-mapping [224] and real-time imaging [222]. Targeted RF heating capabilities of the RF antennas were investigated in phantoms. After showing proof-of-principle for focal radiofrequency heating of a hotspot in the center of a phantom the feasibility of steering a SAR/temperature hotspot to a surface location in the phantom was shown. For this purpose a tailored set of excitation phases was derived from EMF simulations and implemented for each of the applicators transmission elements. The experimental results suggest that the proposed setup is capable of providing enough

energy at 7.0 T to heat up an elliptical area as small as (25 x 22 x 41) mm³ (simulated value: (31 x 31 x 47) mm³) for an iso-temperature 75% inside a uniform phantom with a maximum temperature increase of ΔT = 10.7 K within a 180 s heating period using a total input power of 400 W. Interestingly enough, the temperature increase at the surface of the phantom was only ΔT = 6.7 K without using extra surface cooling. EMF and thermal simulations conducted with a human voxel model of a healthy volunteer revealed that an RF induced hotspot inside the human brain can be generated using the proposed hybrid applicator at 7.0 T. After running an RF heating paradigm for five minutes a temperature increase to 48.6 °C was accomplished in the center of the human brain. Driving the proof-of-principle demonstrated in this study closer to the clinical scenario requires real time feedback capabilities to manage temperature measurements and RF power/RF control simultaneously [12]. The results of this PhD thesis work clearly indicate that even higher frequencies show a major benefit for targeted RF heating applications including MR frequencies far beyond 298 MHz. The observation forwarded in this study, that the SAR and temperature hotspot dimensions are more focused when using higher frequencies, has major implications for future hybrid applicator designs. The size of the antenna elements can be significantly reduced at higher frequencies which would afford a placement of even more transmission elements around the object of interest. An increase in the number of independent transmission elements - each with exquisite phase and amplitude control - would also be instrumental to further sharpen the geometry and size of the temperature hotspot. To this end RF antenna design, simulations and experiments were performed at 500 MHz yielding a 70% reduction in iso-SAR 90% hotspot volume versus 298 MHz antennas for a cylindrical phantom [227]. In-vivo temperature simulations demonstrated that the iso-temperature 90% hotspot is as small as (13 x 16 x 37) mm³ at 500 MHz, compared to (19 x 23 x 32) mm³ at 298 MHz, manifesting a reduction in volume of 45%. The design of even smaller RF antennas at 500 MHz enables an improved efficiency along the long axis of the antenna/phantom mounting to a 30% reduction in the length of the iso-SAR 90% hotspot. To this end, first experimental RF heating experiments were conducted at 500 MHz using a custom built RFPA while MR thermometry, fiber optic temperature measurements and MRI were performed with a 7.0 T MR system. For this

configuration validation experiments demonstrated good agreement between temperature simulations and experimental results with a maximum temperature difference of <2°C. To perform MRI at 298 MHz, additional meander RF antennas were integrated in the 500 MHz targeted RF heating setup. These elements showed good decoupling to the 500 MHz antennas and can be potentially driven in a dual frequency heating mode to increase the degree of freedom for customizing temperature profiles. Even more, these elements can be used as extra receive elements in an array, provided a proper decoupling circuit is used, together with the 8-channel 298 MHz hybrid applicator to improve SNR and parallel imaging performance [234]. Targeted RF heating using higher frequencies (f > 500 MHz) comes with pronounced RF power losses that are present in all RF components including cables, connectors and the RF antennas. While at 298 MHz the dielectric losses of D_20 or deionized water are negligible, power losses constitute major design limitations at 500 MHz. High RFPA power is needed to balance the increased transmit cable losses or the use of magnetic field compatible RFPAs positioned close to the RF coil array [235]. When using high RF power the absorption in the high permittivity dielectric may change its temperature significantly. Since the permittivity and conductivity are both temperature dependent the antenna impedance changes, causing reflection losses to increase. To counteract this behavior low loss ceramics such as $BaTiO_3$ can be utilized. An integrated controlled cooling circuit would be an effective alternative since it bears the additional benefit of removing unwanted heat from surface tissue regions.

With basic feasibility shown at 298 MHz and 500 MHz this work was extended to frequencies as high as f = 1.44 GHz. To this end electromagnetic field simulations using an array of 18 dipole antennas demonstrated that the RF heating iso-SAR 90% hotspot is reduced to a size as small as (4 x 4 x 20) mm³. This improvement constitutes an effective reduction in the surrounding volume by a factor ~13 versus 500 MHz and by a factor of ~43 versus 298 MHz. EMF simulations in the upper leg of a human voxel model showed a B_1^+ field of ~13 $\mu T/\sqrt{\ }kW$ at ~10 cm distance from the RF antennas while local SAR_{10g} was not significantly enhanced in comparison to a 298 MHz setup. With these results it is fair to assume that ^1H human *in vivo* MRI at 33.8 T is feasible and that power deposition as

well as B_1^+ are not limited to surface regions only. Even more, the results shown in this work suggest that *in vivo* EPR at L- or even higher wavebands might be feasible too.

To summarize, the opportunities and capabilities of ultrahigh field MR for RF heating based interventions shown here are intriguing and in a creative state of flux. Bringing ultrahigh field RF heating interventions and therapies into the clinic remains a major challenge though it is certainly worth to put further weight behind the solution of the remaining problems.

References

[1] R. D. Issels, L. H. Lindner, J. Verweij, P. Wust, P. Reichardt, B. C. Schem, S. Abdel-Rahman, S. Daugaard, C. Salat, and C. M. Wendtner, "Neo-adjuvant chemotherapy alone or with regional hyperthermia for localised high-risk soft-tissue sarcoma: A randomised phase 3 multicentre study," *The Lancet Oncology,* vol. 11, pp. 561-570, 2010.

[2] J. Overgaard, S. Bentzen, D. Gonzalez Gonzalez, M. Hulshof, G. Arcangeli, O. Dahl, and O. Mella, "Randomised trial of hyperthermia as adjuvant to radiotherapy for recurrent or metastatic malignant melanoma," *The Lancet,* vol. 345, pp. 540-543, 1995.

[3] R. Valdagni and M. Amichetti, "Report of long-term follow-up in a randomized trial comparing radiation therapy and radiation therapy plus hyperthermia to metastatic lymphnodes in stage IV head and neck patients," *International Journal of Radiation Oncology Biology Physics,* vol. 28, pp. 163-169, 1994.

[4] R. Valdagni, M. Amichetti, and G. Pani, "Radical radiation alone versus radical radiation plus microwave hyperthermia for N3 (TNM-UICC) neck nodes: a prospective randomized clinical trial," *International Journal of Radiation Oncology Biology Physics,* vol. 15, pp. 13-24, 1988.

[5] E. L. Jones, J. R. Oleson, L. R. Prosnitz, T. V. Samulski, Z. Vujaskovic, D. Yu, L. L. Sanders, and M. W. Dewhirst, "Randomized trial of hyperthermia and radiation for superficial tumors," *Journal of Clinical Oncology,* vol. 23, pp. 3079-3085, 2005.

[6] C. C. Vernon, J. W. Hand, S. B. Field, D. Machin, J. B. Whaley, J. Van Der Zee, W. Van Putten, G. C. van Rhoon, J. Van Dijk, and G. D. González, "Radiotherapy with or without hyperthermia in the treatment of superficial localized breast cancer: results from five randomized controlled trials. International Collaborative Hyperthermia Group," *International Journal of Radiation Oncology Biology Physics,* vol. 35, pp. 731-744, 1996.

[7] J. van der Zee, D. González, G. C. van Rhoon, J. D. P. van Dijk, W. L. J. van Putten, and A. A. M. Hart, "Comparison of radiotherapy alone with radiotherapy plus hyperthermia in locally advanced pelvic tumours: a prospective, randomised, multicentre trial," *The Lancet,* vol. 355, pp. 1119-1125, 2000.

[8] P. K. Sneed, P. R. Stauffer, M. W. McDermott, C. J. Diederich, K. R. Lamborn, M. D. Prados, S. Chang, K. A. Weaver, L. Spry, and M. K. Malec, "Survival benefit of hyperthermia in a prospective randomized trial of brachytherapy boost+/- hyperthermia for glioblastoma multiforme," *International Journal of Radiation Oncology Biology Physics,* vol. 40, pp. 287-295, 1998.

[9] P. Wust, B. Hildebrandt, G. Sreenivasa, B. Rau, J. Gellermann, H. Riess, R. Felix, and P. Schlag, "Hyperthermia in combined treatment of cancer," *The Lancet Oncology,* vol. 3, pp. 487-497, 2002.

[10] J. Lagendijk, "Hyperthermia treatment planning," *Physics in Medicine and Biology,* vol. 45, pp. R61-76, 2000.

[11] J. Gellermann, B. Hildebrandt, R. Issels, H. Ganter, W. Wlodarczyk, V. Budach, R. Felix, P. U. Tunn, P. Reichardt, and P. Wust, "Noninvasive magnetic resonance thermography of soft tissue sarcomas during regional hyperthermia," *Cancer,* vol. 107, pp. 1373-1382, 2006.

[12] M. Ranneberg, M. Weiser, M. Weihrauch, V. Budach, J. Gellermann, and P. Wust, "Regularized antenna profile adaptation in online hyperthermia treatment," *Medical Physics,* vol. 37, pp. 5382-5394, 2010.

[13] P. F. Turner, "Regional hyperthermia with an annular phased array," *Biomedical Engineering, IEEE Transactions on,* pp. 106-114, 1984.

[14] J. Gellermann, H. Faehling, M. Mielec, C. Cho, V. Budach, and P. Wust, "Image artifacts during MRT hybrid hyperthermia-Causes and elimination," *International Journal of Hyperthermia,* vol. 24, pp. 327-335, 2008.

[15] E. Moser, F. Stahlberg, M. E. Ladd, and S. Trattnig, "7-T MR—from research to clinical applications?," *NMR in Biomedicine,* vol. 25, pp. 695-716, 2012.

[16] T. Niendorf, A. Graessl, C. Thalhammer, M. A. Dieringer, O. Kraus, D. Santoro, K. Fuchs, F. Hezel, S. Waiczies, B. Ittermann, and L. Winter, "Progress and promises of human cardiac magnetic resonance at ultrahigh fields: A physics perspective," *Journal of Magnetic Resonance,* vol. 229, pp. 208-222, 2012.

[17] K. Kuroda, "Non-invasive MR thermography using the water proton chemical shift," *International Journal of Hyperthermia,* vol. 21, pp. 547-560, 2005.

[18] B. Gallez and H. M. Swartz, "In vivo EPR: when, how and why?," *NMR in Biomedicine,* vol. 17, pp. 223-225, 2004.

[19] D. MCRobbie, E. Moore, M. Graves, and M. Prince, *MRI From Picture to Proton*: Cambridge University Press, 2006.

[20] E. M. Haacke, R. W. Brown, M. R. Thompson, and R. Venkatesan, *Magnetic resonance imaging: physical principles and sequence design* vol. 1: Wiley-Liss New York:, 1999.

[21] D. G. Gadian, *Nuclear magnetic resonance and its applications to living systems*: Clarendon Press Oxford, 1982.

[22] P. T. Callaghan, *Principles of nuclear magnetic resonance microscopy*: Oxford University Press, 1993.

[23] I. Rabi, J. Zacharias, S. Millman, and P. Kusch, "A New Method of Measuring the Nuclear Magnetic Moment," *Physical Review,* vol. 35, pp. 318-318, 1938.

[24] F. Bloch, "Nuclear induction," *Physical Review,* vol. 70, p. 460, 1946.

[25] E. M. Purcell, H. Torrey, and R. V. Pound, "Resonance absorption by nuclear magnetic moments in a solid," *Physical Review,* vol. 69, p. 37, 1946.

[26] K. Wüthrich, *NMR in Structural Biology: A Collection of Papers by Kurt Wüthrich*: World Scientific River Edge, NJ, 1995.

[27] P. C. Lauterbur, "Image formation by induced local interactions: examples employing nuclear magnetic resonance," *Nature,* vol. 242, pp. 190-191, 1973.

[28] P. C. Lauterbur, "Magnetic resonance zeugmatography," *Pure and Applied Chemistry,* vol. 40, pp. 149-157, 1974.

[29] P. Mansfield, "Multi-planar image formation using NMR spin echoes," *Journal of Physics C: Solid State Physics,* vol. 10, p. L55, 1977.

[30] E. L. Hahn, "Spin echoes," *Physical Review,* vol. 80, p. 580, 1950.

[31] V. Rieke and K. Pauly, "MR thermometry," *Journal of Magnetic Resonance Imaging,* vol. 27, pp. 376-390, 2008.

[32] Y. Ishihara, A. Calderon, H. Watanabe, K. Okamoto, Y. Suzuki, and K. Kuroda, "A precise and fast temperature mapping using water proton chemical shift," *Magnetic Resonance in Medicine,* vol. 34, pp. 814-823, 1995.

[33] J. Hindman, "Proton resonance shift of water in the gas and liquid states," *The Journal of Chemical Physics,* vol. 44, p. 4582, 1966.

[34] J. Frahm, A. Haase, and D. Matthaei, "Rapid NMR imaging of dynamic processes using the FLASII technique," *Magnetic Resonance in Medicine,* vol. 3, pp. 321-327, 1986.

[35] A. M. El-Sharkawy, M. Schär, P. A. Bottomley, and E. Atalar, "Monitoring and correcting spatio-temporal variations of the MR scanner's static magnetic field," *Magnetic Resonance Materials in Physics, Biology and Medicine,* vol. 19, pp. 223-236, 2006.

[36] K. Kuroda, K. Oshio, A. H. Chung, K. Hynynen, and F. A. Jolesz, "Temperature mapping using the water proton chemical shift: a chemical shift selective phase mapping method," *Magnetic Resonance in Medicine,* vol. 38, pp. 845-851, 1997.

[37] R. D. Peters and R. M. Henkelman, "Proton-resonance frequency shift MR thermometry is affected by changes in the electrical conductivity of tissue," *Magnetic Resonance in Medicine,* vol. 43, pp. 62-71, 2000.

[38] J. Gellermann, W. Wlodarczyk, A. Feussner, H. Fähling, J. Nadobny, B. Hildebrandt, R. Felix, and P. Wust, "Methods and potentials of magnetic resonance imaging for monitoring radiofrequency hyperthermia in a hybrid system," *International Journal of Hyperthermia,* vol. 21, pp. 497-513, 2005.

[39] U. Wonneberger, B. Schnackenburg, W. Wlodarczyk, T. Walter, F. Streitparth, J. Rump, and U. K. M. Teichgräber, "Intradiscal temperature monitoring using double gradient-echo pulse sequences at 1.0 T," *Journal of Magnetic Resonance Imaging,* vol. 31, pp. 1499-1503, 2010.

[40] D. I. Hoult, "Sensitivity and Power Deposition in a High-Field Imaging Experiment," *Journal of Magnetic Resonance Imaging,* vol. 12, pp. 46-67, 2000.

[41] C. E. Hayes, W. A. Edelstein, J. F. Schenck, O. M. Mueller, and M. Eash, "An efficient, highly homogeneous radiofrequency coil for whole-body NMR imaging at 1.5 T," *Journal of Magnetic Resonance (1969),* vol. 63, pp. 622-628, 1985.

[42] R. Pascone, B. Garcia, T. Fitzgerald, T. Vullo, R. Zipagan, and P. Cahill, "Generalized electrical analysis of low-pass and high-pass birdcage resonators," *Magnetic resonance imaging,* vol. 9, pp. 395-408, 1991.

[43] L. Axel, "Surface coil magnetic resonance imaging," *Journal of Computer Assisted Tomography,* vol. 8, pp. 381-384, 1984.

[44] P. Roemer, W. Edelstein, C. Hayes, S. Souza, and O. Mueller, "The NMR phased array," *Magnetic Resonance in Medicine,* vol. 16, pp. 192-225, 1990.

[45] D. K. Sodickson and W. J. Manning, "Simultaneous acquisition of spatial harmonics (SMASH): fast imaging with radiofrequency coil arrays," *Magnetic Resonance in Medicine,* vol. 38, pp. 591-603, 1997.

[46] K. P. Pruessmann, M. Weiger, M. B. Scheidegger, and P. Boesiger, "SENSE: sensitivity encoding for fast MRI," *Magnetic Resonance in Medicine,* vol. 42, pp. 952-962, 1999.

[47] W. Schnell, "Rauschoptimierung von Oberflächen- und Ganzkörperantennen für die Kernspintomographie," PhD thesis, Fakultät für Elektrotechnik, Ruhr-Universität Bochum, Bochum, 1997.

[48] R. Lattanzi and D. K. Sodickson, "Ideal current patterns yielding optimal signal-to-noise ratio and specific absorption rate in magnetic resonance imaging: Computational methods and physical insights," *Magnetic Resonance in Medicine,* vol. 68, pp. 286-304, 2012.

[49] A. Kumar and P. A. Bottomley, "Optimized quadrature surface coil designs," *Magnetic Resonance Materials in Physics, Biology and Medicine,* vol. 21, pp. 41-52, 2008.

[50] R. F. Lee, R. O. Giaquinto, and C. J. Hardy, "Coupling and decoupling theory and its application to the MRI phased array," *Magnetic Resonance in Medicine,* vol. 48, pp. 203-213, 2002.

[51] J. Wang, "A novel method to reduce the signal coupling of surface coils for MRI," in *Proceedings of the 4th Annual Meeting of ISMRM, New York, NY, USA*, 1996, p. 1434.

[52] J. A. de Zwart, P. J. Ledden, P. van Gelderen, J. Bodurka, R. Chu, and J. H. Duyn, "Signal-to-noise ratio and parallel imaging performance of a 16-channel receive-only brain coil array at 3.0 Tesla," *Magnetic Resonance in Medicine,* vol. 51, pp. 22-26, 2004.

[53] C. J. Hardy, H. E. Cline, R. O. Giaquinto, T. Niendorf, A. K. Grant, and D. K. Sodickson, "32-element receiver-coil array for cardiac imaging," *Magnetic Resonance in Medicine,* vol. 55, pp. 1142-1149, 2006.

[54] Y. Zhu, C. J. Hardy, D. K. Sodickson, R. O. Giaquinto, C. L. Dumoulin, G. Kenwood, T. Niendorf, H. Lejay, C. A. McKenzie, and M. A. Ohliger, "Highly parallel volumetric imaging with a 32-element RF coil array," *Magnetic Resonance in Medicine,* vol. 52, pp. 869-877, 2004.

[55] M. Schmitt, A. Potthast, D. E. Sosnovik, J. R. Polimeni, G. C. Wiggins, C. Triantafyllou, and L. L. Wald, "A 128-channel receive-only cardiac coil for highly accelerated cardiac MRI at 3 Tesla," *Magnetic Resonance in Medicine,* vol. 59, pp. 1431-1439, 2008.

[56] T. Redpath, "Signal-to-noise ratio in MRI," *British Journal of Radiology,* vol. 71, pp. 704-707, 1998.

[57] L. Winter, P. Kellman, W. Renz, A. Gräßl, F. Hezel, C. Thalhammer, F. Von Knobelsdorff Brenkenhoff, V. Tkachenko, J. Schulz-Menger, and T. Niendorf, "Comparison of three multichannel transmit/receive radiofrequency coil configurations for anatomic and functional cardiac MRI at 7.0T: implications for clinical imaging," *European Radiology,* vol. 22, pp. 2211-2220, 2012.

[58] M. A. Ohliger and D. K. Sodickson, "An introduction to coil array design for parallel MRI," *NMR in Biomedicine,* vol. 19, pp. 300-315, 2006.

[59] A. Einstein, *Investigations on the Theory of the Brownian Movement*: Courier Dover Publications, 1956.

[60] H. Nyquist, "Thermal agitation of electric charge in conductors," *Physical Review,* vol. 32, pp. 110-113, 1928.

[61] A. Macovski, "Noise in MRI," *Magnetic Resonance in Medicine,* vol. 36, pp. 494-497, 1996.

[62] T. Redpath, "Noise correlation in multicoil receiver systems," *Magnetic Resonance in Medicine,* vol. 24, pp. 85-89, 1992.

[63] R. Brown, Y. Wang, P. Spincemaille, and R. F. Lee, "On the noise correlation matrix for multiple radio frequency coils," *Magnetic Resonance in Medicine,* vol. 58, pp. 218-224, 2007.

[64] P. Kellman and E. R. McVeigh, "Image reconstruction in SNR units: A general method for SNR measurement†," *Magnetic Resonance in Medicine,* vol. 54, pp. 1439-1447, 2005.

[65] L. Winter, C. Özerdem, W. Hoffmann, D. Santoro, A. Müller, H. Waiczies, R. Seemann, A. Graessl, P. Wust, and T. Niendorf, "Design and Evaluation of a Hybrid Radiofrequency Applicator for Magnetic Resonance Imaging and RF Induced Hyperthermia: Electromagnetic Field Simulations up to 14.0 Tesla and Proof-of-Concept at 7.0 Tesla," *PLOS ONE,* vol. 8, p. e61661, 2013.

[66] O. Dietrich, J. G. Raya, S. B. Reeder, M. F. Reiser, and S. O. Schoenberg, "Measurement of signal-to-noise ratios in MR images: Influence of multichannel coils, parallel imaging, and reconstruction filters," *Journal of Magnetic Resonance Imaging,* vol. 26, pp. 375-385, 2007.

[67] P. Kellman, "Erratum to Kellman P, McVeigh ER. Image reconstruction in SNR units: a general method for SNR measurement. Magn Reson Med. 2005; 54: 1439–1447," *Magnetic Resonance in Medicine,* vol. 58, pp. 211-212, 2007.

[68] M. A. Griswold, P. M. Jakob, R. M. Heidemann, M. Nittka, V. Jellus, J. Wang, B. Kiefer, and A. Haase, "Generalized autocalibrating partially parallel acquisitions (GRAPPA)," *Magnetic Resonance in Medicine,* vol. 47, pp. 1202-1210, 2002.

[69] U. Katscher, P. Bornert, C. Leussler, and J. van den Brink, "Transmit SENSE," *Magnetic Resonance in Medicine,* vol. 49, pp. 144-150, 2003.

[70] D. K. Sodickson, C. J. Hardy, Y. Zhu, R. O. Giaquinto, P. Gross, G. Kenwood, T. Niendorf, H. Lejay, C. A. McKenzie, M. A. Ohliger, A. K. Grant, and N. M. Rofsky, "Rapid volumetric MRI using parallel imaging with order-of-magnitude accelerations and a 32-element RF coil array: feasibility and implications," *Academic Radiology,* vol. 12, pp. 626-35, May 2005.

[71] C. J. Hardy, R. O. Giaquinto, J. E. Piel, A. Rohling, W. Kenneth, L. Marinelli, D. J. Blezek, E. W. Fiveland, R. D. Darrow, and T. K. Foo, "128-channel body MRI with a flexible high-density receiver-coil array," *Journal of Magnetic Resonance Imaging,* vol. 28, pp. 1219-1225, 2008.

[72] T. Niendorf and D. K. Sodickson, "Parallel imaging in cardiovascular MRI: methods and applications," *NMR in Biomedicine,* vol. 19, pp. 325-341, 2006.

[73] G. C. Wiggins, J. R. Polimeni, A. Potthast, M. Schmitt, V. Alagappan, and L. L. Wald, "96-Channel receive-only head coil for 3 Tesla: Design optimization and evaluation," *Magnetic Resonance in Medicine,* vol. 62, pp. 754-762, 2009.

[74] M. Blaimer, F. Breuer, M. Mueller, R. M. Heidemann, M. A. Griswold, and P. M. Jakob, "SMASH, SENSE, PILS, GRAPPA: how to choose the optimal method," *Topics in Magnetic Resonance Imaging,* vol. 15, pp. 223-236, 2004.

[75] M. Weiger, K. P. Pruessmann, C. Leussler, P. Röschmann, and P. Boesiger, "Specific coil design for SENSE: A six-element cardiac array," *Magnetic Resonance in Medicine,* vol. 45, pp. 495-504, 2001.

[76] Y. Zhu, "Parallel excitation with an array of transmit coils," *Magnetic Resonance in Medicine,* vol. 51, pp. 775-784, 2004.

[77] K. W. Angel, "Transmit-Receive Switch," US Patent 3.452.299,1969.

[78] G. Shajan, J. Hoffmann, J. Budde, G. Adriany, K. Ugurbil, and R. Pohmann, "Design and evaluation of an RF front-end for 9.4 T human MRI," *Magnetic Resonance in Medicine,* vol. 66, pp. 594-602, 2011.

[79] A. Sotgiu and J. S. Hyde, "High-Order Coils as Transmitters for NMR Imaging," *Magnetic Resonance in Medicine,* vol. 3, pp. 55-62, 1986.

[80] M. A. Dieringer, W. Renz, T. Lindel, F. Seifert, T. Frauenrath, F. von Knobelsdorff-Brenkenhoff, H. Waiczies, W. Hoffmann, J. Rieger, H. Pfeiffer, B. Ittermann, J. Schulz-Menger, and T. Niendorf, "Design and application of a four-channel transmit/receive surface coil for functional cardiac imaging at 7T," *Journal of Magnetic Resonance Imaging,* vol. 33, pp. 736-41, Mar 2011.

[81] K. Setsompop, L. L. Wald, V. Alagappan, B. Gagoski, F. Hebrank, U. Fontius, F. Schmitt, and E. Adalsteinsson, "Parallel RF transmission with eight channels at 3 Tesla," *Magnetic Resonance in Medicine,* vol. 56, pp. 1163-1171, 2006.

[82] T. Niendorf, L. Winter, and T. Frauenrath, "Electrocardiogram in an MRI Environment: Clinical Needs, Practical Considerations, Safety Implications, Technical Solutions and Future Directions," in *Advances in Electrocardiograms - Methods and Analysis*, R. M. Millis, Ed., ed HR: Intech, 2012, pp. 309-324.

[83] E. J. Wilkinson, "An N-way hybrid power divider," *Microwave Theory and Techniques, IRE Transactions on,* vol. 8, pp. 116-118, 1960.

[84] J. Butler, "Beam-forming matrix simplifies design of electronically scanned antennas," *Electron. Des.,* vol. 9, pp. 170-173, 1961.

[85] P. Van de Moortele, C. Akgun, G. Adriany, S. Moeller, J. Ritter, C. Collins, M. Smith, J. Vaughan, and K. U urbil, "B (1) destructive interferences and spatial phase patterns at 7 T with a head transceiver array coil," *Magnetic Resonance in Medicine,* vol. 54, pp. 1503-1518, 2005.

[86] G. Metzger, C. Snyder, C. Akgun, T. Vaughan, K. Ugurbil, and P. Van de Moortele, "Local B1+ shimming for prostate imaging with transceiver arrays at 7T based on subject-dependent transmit phase measurements," *Magnetic Resonance in Medicine,* vol. 59, pp. 396-409, 2008.

[87] P. Ullmann, S. Junge, M. Wick, F. Seifert, W. Ruhm, and J. Hennig, "Experimental analysis of parallel excitation using dedicated coil setups and simultaneous RF transmission on multiple channels," *Magnetic Resonance in Medicine,* vol. 54, pp. 994-1001, 2005.

[88] U. Katscher and P. Börnert, "Parallel RF transmission in MRI," *NMR in Biomedicine,* vol. 19, pp. 393-400, 2006.

[89] B. van den Bergen, C. A. T. Van den Berg, L. W. Bartels, and J. J. W. Lagendijk, "7 T body MRI: B1 shimming with simultaneous SAR reduction," *Physics in Medicine and Biology,* vol. 52, p. 5429, 2007.

[90] G. Eichfelder and M. Gebhardt, "Local specific absorption rate control for parallel transmission by virtual observation points," *Magnetic Resonance in Medicine,* 2011.

[91] IEC, "60601-2-33 Medical electrical equipment - Part 2-33: Particular requirements for the basic safety and essential performance of magnetic resonance equipment for medical diagnosis. Edition 3.0," 2010.

[92] J. T. Vaughan, M. Garwood, C. Collins, W. Liu, L. DelaBarre, G. Adriany, P. Andersen, H. Merkle, R. Goebel, and M. Smith, "7T vs. 4T: RF power, homogeneity, and signal-to-noise comparison in head images," *Magnetic Resonance in Medicine,* vol. 46, pp. 24-30, 2001.

[93] A. Gräßl, L. Winter, C. Thalhammer, W. Renz, P. Kellman, C. Martin, F. Von Knobelsdorff Brenkenhoff, V. Tkachenko, J. Schulz-Menger, and T. Niendorf, "Design, evaluation and application of an eight channel transmit/receive coil array for cardiac MRI at 7.0T," *European Journal of Radiology,* vol. 82, pp. 752-759, 2011.

[94] C. Thalhammer, W. Renz, L. Winter, F. Hezel, J. Rieger, H. Pfeiffer, A. Graessl, F. Seifert, W. Hoffmann, F. Von Knobelsdorff Brenkenhoff, V. Tkachenko, J. Schulz-Menger, P. Kellman, and T. Niendorf, "Two-dimensional Sixteen Channel Transmit/Receive Coil Array for Cardiac MRI at 7.0 Tesla: Design, Evaluation and Application," *Journal of Magnetic Resonance Imaging,* vol. 36, pp. 847-57, 2012.

[95] A. Graessl, W. Renz, F. Hezel, M. Dieringer, L. Winter, Oezerdem C, P. Kellman, D. Santoro, T. Lindel, T. Frauenrath, H. Pfeiffer, and T. Niendorf, "Modular 32 Channel Transceiver Coil Array for Cardiac MRI at 7T," *Magnetic Resonance in Medicine,* 2013.

[96] K. Kollia, S. Maderwald, N. Putzki, M. Schlamann, J. Theysohn, O. Kraff, M. Ladd, M. Forsting, and I. Wanke, "First clinical study on ultra-high-field MR imaging in patients with multiple sclerosis: comparison of 1.5 T and 7T," *American Journal of Neuroradiology,* vol. 30, pp. 699-702, 2009.

[97] C. Laule, P. Kozlowski, E. Leung, D. K. Li, A. L. MacKay, and G. Moore, "Myelin water imaging of multiple sclerosis at 7 T: correlations with histopathology," *Neuroimage,* vol. 40, pp. 1575-1580, 2008.

[98] S. G. van Elderen, M. J. Versluis, J. J. Westenberg, H. Agarwal, N. B. Smith, M. Stuber, A. de Roos, and A. G. Webb, "Right coronary MR angiography at 7 T: a direct quantitative and qualitative comparison with 3 T in young healthy volunteers," *Radiology,* vol. 257, pp. 254-9, Oct 2010.

[99] F. von Knobelsdorff-Brenkenhoff, T. Frauenrath, M. Prothmann, M. A. Dieringer, F. Hezel, W. Renz, K. Kretschel, T. Niendorf, and J. Schulz-Menger, "Cardiac chamber quantification using magnetic resonance imaging at 7 Tesla—a pilot study," *European Radiology,* vol. 20, pp. 2844-52, 2010.

[100] F. von Knobelsdorff-Brenkenhoff, V. Tkachenko, L. Winter, J. Rieger, C. Thalhammer, F. Hezel, A. Graessl, M. A. Dieringer, T. Niendorf, and J. Schulz-Menger, "Assessment of the right ventricle with cardiovascular magnetic resonance at 7 Tesla," *Journal of Cardiovascular Magnetic Resonance,* vol. 15, p. 23, 2013.

[101] C. M. Collins and M. B. Smith, "Signal-to-noise ratio and absorbed power as functions of main magnetic field strength, and definition of "90°" RF pulse for the head in the birdcage coil," *Magnetic Resonance in Medicine,* vol. 45, pp. 684-691, 2001.

[102] J. Vaughan, C. Snyder, L. DelaBarre, P. Bolan, J. Tian, L. Bolinger, G. Adriany, P. Andersen, J. Strupp, and K. Ugurbil, "Whole-body imaging at 7T: preliminary results," *Magn Reson Med,* vol. 61, pp. 244-248, Jan 2009.

[103] C. Gabriel, "Compilation of the Dielectric Properties of Body Tissues at RF and Microwave Frequencies," DTIC Document1996.

[104] S. Gabriel, R. Lau, and C. Gabriel, "The dielectric properties of biological tissues: II. Measurements in the frequency range 10 Hz to 20 GHz," *Physics in Medicine and Biology,* vol. 41, p. 2251, 1996.

[105] D. Andreuccetti, R. Fossi, and C. Petrucci, "An Internet ressource for the calculation of the dielectric properties of body tissues in the frequency range 10 Hz - 100 GHz," *Website at http://niremf.ifac.cnr.it/tissprop/. IFAC-CNR, Florence (Italy). Based on data published by C. Gabriel et al. in 1996,* 1997.

[106] P. Gregor Adriany, F. Moortele, J. Steen Moeller, C. Peter Andersen, W. Xiaoliang Zhang, P. Klaas, and T. Peter Boesiger, "Transmit and receive transmission line arrays for 7 Tesla parallel imaging," *Magnetic Resonance in Medicine,* vol. 53, pp. 434-445, 2005.

[107] A. Ahlbom, U. Bergqvist, J. Bernhardt, J. Cesarini, M. Grandolfo, M. Hietanen, A. Mckinlay, M. Repacholi, D. Sliney, and J. Stolwijk, "Guidelines for limiting exposure to time-varying electric, magnetic, and electromagnetic fields (up to 300 GHz). International Commission on Non-Ionizing Radiation Protection," *Health Physics,* vol. 74, pp. 494-522, 1998.

[108] D. Hoult and P. C. Lauterbur, "The sensitivity of the zeugmatographic experiment involving human samples," *Journal of Magnetic Resonance (1969),* vol. 34, pp. 425-433, 1979.

[109] A. Christ, W. Kainz, E. Hahn, K. Honegger, M. Zefferer, E. Neufeld, W. Rascher, R. Janka, W. Bautz, and J. Chen, "The Virtual Family—development of surface-based anatomical models of two adults and two children for dosimetric simulations," *Physics in Medicine and Biology,* vol. 55, pp. N23-38, 2010.

[110] C. M. Collins and M. B. Smith, "Calculations of B1 distribution, SNR, and SAR for a surface coil adjacent to an anatomically-accurate human body model," *Magnetic Resonance in Medicine,* vol. 45, pp. 692-699, 2001.

[111] Z. Wang, J. C. Lin, W. Mao, W. Liu, M. B. Smith, and C. M. Collins, "SAR and temperature: simulations and comparison to regulatory limits for MRI," *Journal of Magnetic Resonance Imaging,* vol. 26, pp. 437-441, 2007.

[112] P. S. Yarmolenko, E. J. Moon, C. Landon, A. Manzoor, D. W. Hochman, B. L. Viglianti, and M. W. Dewhirst, "Thresholds for thermal damage to normal tissues: An update," *International Journal of Hyperthermia,* vol. 27, pp. 320-343, 2011.

[113] M. Murbach, E. Neufeld, M. Capstick, W. Kainz, D. O. Brunner, T. Samaras, K. P. Pruessmann, and N. Kuster, "Thermal Tissue Damage Model Analyzed for Different Whole-Body SAR and Scan Durations for Standard MR Body Coils," *Magnetic Resonance in Medicine,* 2013.

[114] G. C. van Rhoon, T. Samaras, P. S. Yarmolenko, M. W. Dewhirst, E. Neufeld, and N. Kuster, "CEM43° C thermal dose thresholds: a potential guide for magnetic resonance radiofrequency exposure levels?," *European Radiology,* pp. 1-13, 2013.

[115] K. Scheffler and S. Lehnhardt, "Principles and applications of balanced SSFP techniques," *European Radiology,* vol. 13, pp. 2409-2418, 2003.

[116] O. Kraus, M. Dieringer, F. Hezel, L. Winter, A. Graessl, O. C, and T. Niendorf, "2D CINE SSFP Imaging at 7.0T using 8-channel Bowtie Antenna Transceiver Arrays: A Cardiac MR Feasibility Study," in *Proceedings of the 21st Annual Meeting of ISMRM, Salt Lake City, UT, USA*, 2013.

[117] J. Hennig, A. Nauerth, and H. Friedburg, "RARE imaging: a fast imaging method for clinical MR," *Magnetic Resonance in Medicine,* vol. 3, pp. 823-833, 1986.

[118] K. Fuchs, F. Hezel, L. Winter, O. C, A. Graessl, M. Dieringer, O. Kraus, and T. Niendorf, "Feasibility of Cardiac Fast Spin Echo Imaging at 7.0T Using a Two-Dimensional 16 Channel Array of Bowtie Transceivers," in *Proceedings of the 21st Annual Meeting of ISMRM, Salt Lake City, UT, USA*, 2013.

[119] M. Versluis, N. Tsekos, N. Smith, and A. Webb, "Simple RF design for human functional and morphological cardiac imaging at 7 tesla," *Journal of Magnetic Resonance,* vol. 200, pp. 161-166, 2009.

[120] S. G. van Elderen, M. J. Versluis, A. G. Webb, J. J. Westenberg, J. Doornbos, N. B. Smith, A. de Roos, and M. Stuber, "Initial results on in vivo human coronary MR angiography at 7 T," *Magnetic Resonance in Medicine,* vol. 62, pp. 1379-84, 2009.

[121] C. J. Snyder, L. DelaBarre, G. J. Metzger, P. F. van de Moortele, C. Akgun, K. Ugurbil, and J. T. Vaughan, "Initial results of cardiac imaging at 7 Tesla," *Magnetic Resonance in Medicine,* vol. 61, pp. 517-24, 2009.

[122] A. Raaijmakers, O. Ipek, D. Klomp, C. Possanzini, P. Harvey, J. Lagendijk, and C. van den Berg, "Design of a radiative surface coil array element at 7 T: The single side adapted dipole antenna," *Magnetic Resonance in Medicine,* vol. 66, pp. 1488-1497, 2011.

[123] O. Ocali and E. Atalar, "Ultimate intrinsic signal-to-noise ratio in MRI," *Magnetic Resonance in Medicine,* vol. 39, pp. 462-473, 1998.

[124] J. Wang, Q. X. Yang, X. Zhang, C. M. Collins, M. B. Smith, X. H. Zhu, G. Adriany, K. Ugurbil, and W. Chen, "Polarization of the RF field in a human head at high field: a study with a quadrature surface coil at 7.0 T," *Magnetic Resonance in Medicine,* vol. 48, pp. 362-369, 2002.

[125] G. Shajan, M. Kozlov, J. Hoffmann, R. Turner, K. Scheffler, and R. Pohmann, "A 16-channel dual-row transmit array in combination with a 31-element receive array for human brain imaging at 9.4 T," *Magnetic Resonance in Medicine,* 2013.

[126] P. Gregor Adriany, J. Moortele, E. Steen Moeller, C. Can Akgün, and K. Thomas Vaughan, "A geometrically adjustable 16-channel transmit/receive transmission line array for improved RF efficiency and parallel imaging performance at 7 Tesla," *Magnetic Resonance in Medicine,* vol. 59, pp. 590-597, 2008.

[127] J. Vaughan, G. Adriany, C. Snyder, J. Tian, T. Thiel, L. Bolinger, H. Liu, L. DelaBarre, and K. Ugurbil, "Efficient high-frequency body coil for high-field MRI," *Magnetic Resonance in Medicine,* vol. 52, pp. 851-859, 2004.

[128] D. Brunner, N. Zanche, J. Froehlich, D. Baumann, and K. Pruessmann, "A symmetrically fed microstrip coil array for 7T," in *Proceedings of the 15th Annual Meeting of ISMRM, Berlin, Germany*, 2007, p. 448.

[129] S. Orzada, A. Bahr, and T. Bolz, "A novel 7 T microstrip element using meanders to enhance decoupling," in *Proceedings of the 16th Annual Meeting of ISMRM, Toronto, Canada*, 2008, p. 10.7.

[130] T. Niendorf, C. J. Hardy, R. O. Giaquinto, P. Gross, H. E. Cline, Y. Zhu, G. Kenwood, S. Cohen, A. K. Grant, and S. Joshi, "Toward single breath-hold whole-heart coverage coronary MRA using highly accelerated parallel imaging with a 32-channel MR system," *Magnetic Resonance in Medicine,* vol. 56, pp. 167-176, 2006.

[131] T. Niendorf, D. K. Sodickson, G. A. Krombach, and J. Schulz-Menger, "Toward cardiovascular MRI at 7 T: clinical needs, technical solutions and research promises," *European Radiology,* vol. 20, pp. 2806-16, 2010.

[132] P. A. Bottomley, C. H. L. Olivieri, and R. Giaquinto, "What is the optimum phased array coil design for cardiac and torso magnetic resonance?," *Magnetic Resonance in Medicine,* vol. 37, pp. 591-599, 1997.

[133] G. Adriany, J. Ritter, J. Vaughan, K. Ugurbil, and P. Van de Moortele, "Experimental verification of enhanced B1 shim performance with a Z-encoding RF coil array at 7

Tesla," in *Proceedings of the Joint Annual Meeting of ISMRM-ESMRMB, Stockholm, Sweden*, 2010.

[134] M. A. Ohliger, A. K. Grant, and D. K. Sodickson, "Ultimate intrinsic signal-to-noise ratio for parallel MRI: Electromagnetic field considerations," *Magnetic Resonance in Medicine,* vol. 50, pp. 1018-1030, 2003.

[135] F. Wiesinger, P. Boesiger, and K. P. Pruessmann, "Electrodynamics and ultimate SNR in parallel MR imaging," *Magnetic Resonance in Medicine,* vol. 52, pp. 376-390, 2004.

[136] L. L. Wald and G. Wiggins, "New coil systems for highly parallel MR acquisition strategies," in *Parallel Imaging in Clinical MR Applications*, ed: Springer, 2007, pp. 497-510.

[137] T. Frauenrath, T. Niendorf, and M. Kob, "Acoustic method for synchronization of magnetic resonance imaging (MRI)," *Acta Acustica united with Acustica,* vol. 94, pp. 148-155, 2008.

[138] M. Becker, T. Frauenrath, F. Hezel, G. A. Krombach, U. Kremer, B. Koppers, C. Butenweg, A. Goemmel, J. F. Utting, J. Schulz-Menger, and T. Niendorf, "Comparison of left ventricular function assessment using phonocardiogram- and electrocardiogram-triggered 2D SSFP CINE MR imaging at 1.5 T and 3.0 T," *European Radiology,* vol. 20, pp. 1344-55, Jun 2010.

[139] M. D. Cerqueira, N. J. Weissman, V. Dilsizian, A. K. Jacobs, S. Kaul, W. K. Laskey, D. J. Pennell, J. A. Rumberger, T. Ryan, and M. S. Verani, "Standardized myocardial segmentation and nomenclature for tomographic imaging of the heart: a statement for healthcare professionals from the Cardiac Imaging Committee of the Council on Clinical Cardiology of the American Heart Association," *Circulation,* vol. 105, pp. 539-542, 2002.

[140] K. Levenberg, "A method for the solution of certain problems in least squares," *Quarterly of Applied Mathematics,* vol. 2, pp. 164-168, 1944.

[141] D. W. Marquardt, "An algorithm for least-squares estimation of nonlinear parameters," *Journal of the Society for Industrial & Applied Mathematics,* vol. 11, pp. 431-441, 1963.

[142] R. Jayasundar, L. Hall, and N. Bleehen, "RF coils for combined MR and hyperthermia studies: I. Hyperthermia applicator as an MR coil," *Magnetic resonance imaging,* vol. 19, pp. 111-116, 2001.

[143] R. Jayasundar, L. Hall, and N. Bleehen, "RF coils for combined MR and hyperthermia studies: II. MR coil as an hyperthermic applicator," *Magnetic resonance imaging,* vol. 19, pp. 117-122, 2001.

[144] K. B. Laupland, "Fever in the critically ill medical patient," *Critical Care Medicine,* vol. 37, pp. S273-S278, 2009.

[145] R. B. Roemer, "Engineering aspects of hyperthermia therapy," *Annual Review of Biomedical Engineering,* vol. 1, pp. 347-376, 1999.

[146] M. W. Miller and M. C. Ziskin, "Biological consequences of hyperthermia," *Ultrasound in Medicine & Biology,* vol. 15, pp. 707-722, 1989.

[147] W. Dewey, L. Hopwood, S. Sapareto, and L. Gerweck, "Cellular responses to combinations of hyperthermia and radiation," *Radiology,* vol. 123, pp. 463-474, 1977.

[148] S. Sapareto and W. Dewey, "Thermal dose determination in cancer therapy," *International Journal of Radiation Oncology Biology Physics,* vol. 10, p. 787, 1984.

[149] J. L. Roti Roti, "Cellular responses to hyperthermia (40-46 C): Cell killing and molecular events," *International Journal of Hyperthermia,* vol. 24, pp. 3-15, 2008.

[150] C. Streffer, "Molecular and cellular mechanisms of hyperthermia," in *Thermoradiotherapy and Thermochemotherapy*. vol. 1, ed: Springer, 1995, pp. 47-74.

[151] G. Jego, A. Hazoumé, R. Seigneuric, and C. Garrido, "Targeting heat shock proteins in cancer," *Cancer Letters,* vol. 332, pp. 275-285, 2013.

[152] S. A. Sapareto, L. E. Hopwood, W. C. Dewey, M. R. Raju, and J. W. Gray, "Effects of hyperthermia on survival and progression of Chinese hamster ovary cells," *Cancer Research,* vol. 38, pp. 393-400, 1978.

[153] B. Hildebrandt, P. Wust, O. Ahlers, A. Dieing, G. Sreenivasa, T. Kerner, R. Felix, and H. Riess, "The cellular and molecular basis of hyperthermia," *Critical Reviews in Oncology Hematology,* vol. 43, pp. 33-56, 2002.

[154] M. Mackey, X. Zhang, C. Hunt, S. Sullivan, J. Blum, A. Laszlo, and J. R. Roti, "Uncoupling of M-phase kinase activation from the completion of S-phase by heat shock," *Cancer Research,* vol. 56, pp. 1770-1774, 1996.

[155] J. Sakkers, J. F. Brunsting, A. R. Filon, H. H. Kampinga, A. Konings, and R. Mullenders, "Altered association of transcriptionally active DNA with the nuclear-matrix after heat shock," *International Journal of Radiation Biology,* vol. 75, pp. 875-883, 1999.

[156] B. Frey, E.-M. Weiss, Y. Rubner, R. Wunderlich, O. J. Ott, R. Sauer, R. Fietkau, and U. S. Gaipl, "Old and new facts about hyperthermia-induced modulations of the immune system," *International Journal of Hyperthermia,* vol. 28, pp. 528-542, 2012.

[157] S. K. Calderwood, M. A. Stevenson, and G. M. Hahn, "Effects of heat on cell calcium and inositol lipid metabolism," *Radiation Research,* vol. 113, pp. 414-425, 1988.

[158] C. Dressler, J. Beuthan, G. Mueller, U. Zabarylo, and O. Minet, "Fluorescence imaging of heat-stress induced mitochondrial long-term depolarization in breast cancer cells," *Journal of Fluorescence,* vol. 16, pp. 689-695, 2006.

[159] M. W. Dewhirst, Z. Vujaskovic, E. Jones, and D. Thrall, "Re-setting the biologic rationale for thermal therapy," *International Journal of Hyperthermia,* vol. 21, pp. 779-790, 2005.

[160] I. F. Tannock, "Tumor physiology and drug resistance," *Cancer and Metastasis Reviews,* vol. 20, pp. 123-132, 2001.

[161] P. Schildkopf, O. J Ott, B. Frey, M. Wadepohl, R. Sauer, R. Fietkau, and U. S Gaipl, "Biological Rationales and Clinical Applications of Temperature Controlled Hyperthermia-Implications for Multimodal Cancer Treatments," *Current Medicinal Chemistry,* vol. 17, pp. 3045-3057, 2010.

[162] S. B. Nadin, F. D. Cuello-Carrión, M. L. Sottile, D. R. Ciocca, and L. M. Vargas-Roig, "Effects of hyperthermia on Hsp27 (HSPB1), Hsp72 (HSPA1A) and DNA repair proteins hMLH1 and hMSH2 in human colorectal cancer hMLH1-deficient and hMLH1-proficient cell lines," *International Journal of Hyperthermia,* vol. 28, pp. 191-201, 2012.

[163] J. J. Skitzki, E. A. Repasky, and S. S. Evans, "Hyperthermia as an immunotherapy strategy for cancer," *Current Opinion in Investigational Drugs,* vol. 10, p. 550, 2009.

[164] P. Srivastava, "Interaction of heat shock proteins with peptides and antigen presenting cells: chaperoning of the innate and adaptive immune responses," *Annual Review of Immunology,* vol. 20, pp. 395-425, 2002.

[165] S. K. Calderwood, M. A. Khaleque, D. B. Sawyer, and D. R. Ciocca, "Heat shock proteins in cancer: chaperones of tumorigenesis," *Trends in Biochemical Sciences,* vol. 31, pp. 164-172, 2006.

[166] J. R. Ostberg, C. Gellin, R. Patel, and E. A. Repasky, "Regulatory potential of fever-range whole body hyperthermia on Langerhans cells and lymphocytes in an antigen-dependent cellular immune response," *The Journal of Immunology,* vol. 167, pp. 2666-2670, 2001.

[167] R. Burd, T. S. Dziedzic, Y. Xu, M. A. Caligiuri, J. R. Subjeck, and E. A. Repasky, "Tumor cell apoptosis, lymphocyte recruitment and tumor vascular changes are induced by low temperature, long duration (fever-like) whole body hyperthermia," *Journal of Cellular Physiology,* vol. 177, pp. 137-147, 1998.

[168] J. D. Cox and K. K. Ang, *Radiation Oncology: rationale, technique and results*: Elsevier Health Sciences, 2003.

[169] R. G. Bristow and R. P. Hill, "Hypoxia and metabolism: hypoxia, DNA repair and genetic instability," *Nature Reviews Cancer,* vol. 8, pp. 180-192, 2008.

[170] M. R. Horsman, B. G. Wouters, M. C. Joiner, and J. Overgaard, "The oxygen effect and fractionated radiotherapy," *Basic Clinical Radiobiology,* pp. 207-9, 2009.

[171] M. Urano, "Invited review: for the clinical application of thermochemotherapy given at mild temperatures," *International Journal of Hyperthermia,* vol. 15, pp. 79-107, 1999.

[172] R. D. Issels, "Hyperthermia adds to chemotherapy," *European Journal of Cancer,* vol. 44, pp. 2546-2554, 2008.

[173] C.-T. Lee, T. Mace, and E. A. Repasky, "Hypoxia-driven immunosuppression: a new reason to use thermal therapy in the treatment of cancer?," *International Journal of Hyperthermia,* vol. 26, pp. 232-246, 2010.

[174] R. J. Griffin, R. P. Dings, A. Jamshidi-Parsian, and C. W. Song, "Mild temperature hyperthermia and radiation therapy: Role of tumour vascular thermotolerance and relevant physiological factors," *International Journal of Hyperthermia,* vol. 26, pp. 256-263, 2010.

[175] D. W. Kufe, R. E. Pollock, R. R. Weichselbaum, R. C. Bast, T. S. Gansler, J. F. Holland, and E. Frei, *Holland-Frei Cancer Medicine*, 6th ed.: BC Decker, 2003.

[176] Y. H. Bae and K. Park, "Targeted drug delivery to tumors: myths, reality and possibility," *Journal of Controlled Release,* vol. 153, p. 198, 2011.

[177] J. A. Barreto, W. O'Malley, M. Kubeil, B. Graham, H. Stephan, and L. Spiccia, "Nanomaterials: applications in cancer imaging and therapy," *Advanced Materials,* 2011.

[178] J. R. McDaniel, M. W. Dewhirst, and A. Chilkoti, "Actively targeting solid tumours with thermoresponsive drug delivery systems that respond to mild hyperthermia," *International Journal of Hyperthermia,* pp. 1-10, 2013.

[179] A. Chilkoti, M. R. Dreher, D. E. Meyer, and D. Raucher, "Targeted drug delivery by thermally responsive polymers," *Advanced Drug Delivery Reviews,* vol. 54, pp. 613-630, 2002.

[180] A. Bangham, M. Standish, and J. Watkins, "Diffusion of univalent ions across the lamellae of swollen phospholipids," *Journal of Molecular Biology,* vol. 13, pp. 238-IN27, 1965.

[181] M. B. Yatvin, J. N. Weinstein, W. H. Dennis, and R. Blumenthal, "Design of liposomes for enhanced local release of drugs by hyperthermia," *Science,* vol. 202, pp. 1290-1293, 1978.

[182] A. Gasselhuber, M. R. Dreher, F. Rattay, B. J. Wood, and D. Haemmerich, "Comparison of conventional chemotherapy, stealth liposomes and temperature-sensitive liposomes in a mathematical model," *PLOS ONE,* vol. 7, p. e47453, 2012.

[183] D. Needham, G. Anyarambhatla, G. Kong, and M. W. Dewhirst, "A new temperature-sensitive liposome for use with mild hyperthermia: characterization and testing in a human tumor xenograft model," *Cancer Research,* vol. 60, pp. 1197-1201, 2000.

[184] M. de Smet, S. Langereis, S. den Bosch, and H. Grüll, "Temperature-sensitive liposomes for doxorubicin delivery under MRI guidance," *Journal of Controlled Release,* vol. 143, pp. 120-127, 2010.

[185] G. A. Koning, A. M. M. Eggermont, L. H. Lindner, and T. L. M. ten Hagen, "Hyperthermia and thermosensitive liposomes for improved delivery of chemotherapeutic drugs to solid tumors," *Pharmaceutical Research,* vol. 27, pp. 1750-1754, 2010.

[186] N. McDannold, S. L. Fossheim, H. Rasmussen, H. Martin, N. Vykhodtseva, and K. Hynynen, "Heat-activated Liposomal MR Contrast Agent: Initial in Vivo Results in Rabbit Liver and Kidney1," *Radiology,* vol. 230, p. 743, 2004.

[187] L. Frich, A. Bjørnerud, S. Fossheim, T. Tillung, and I. Gladhaug, "Experimental application of thermosensitive paramagnetic liposomes for monitoring magnetic resonance imaging guided thermal ablation," *Magnetic Resonance in Medicine,* vol. 52, pp. 1302-1309, 2004.

[188] S. Langereis, J. Keupp, J. L. J. van Velthoven, I. H. C. de Roos, D. Burdinski, J. A. Pikkemaat, and H. Grüll, "A temperature-sensitive liposomal 1H CEST and 19F contrast agent for MR image-guided drug delivery," *Journal of the American Chemical Society,* vol. 131, pp. 1380-1381, 2009.

[189] M. R. Horsman and J. Overgaard, "Hyperthermia: a Potent Enhancer of Radiotherapy," *Clinical Oncology,* vol. 19, pp. 418-426, 2007.

[190] J. Van der Zee, "Heating the patient: a promising approach?," *Annals of Oncology,* vol. 13, pp. 1173-1184, 2002.

[191] R. Colombo, A. Salonia, Z. Leib, M. Pavone-Macaluso, and D. Engelstein, "Long-term outcomes of a randomized controlled trial comparing thermochemotherapy with mitomycin-C alone as adjuvant treatment for non-muscle-invasive bladder cancer (NMIBC)," *BJU International,* vol. 107, pp. 912-918, 2011.

[192] V. J. Verwaal, S. Bruin, M. Gooike van Slooten, and H. van Tinteren ScM, "8-year follow-up of randomized trial: cytoreduction and hyperthermic intraperitoneal chemotherapy versus systemic chemotherapy in patients with peritoneal carcinomatosis of colorectal cancer," *Annals of Surgical Oncology,* vol. 15, pp. 2426-2432, 2008.

[193] V. J. Verwaal, S. van Ruth, E. de Bree, G. W. van Slooten, H. van Tinteren, H. Boot, and F. A. Zoetmulder, "Randomized trial of cytoreduction and hyperthermic intraperitoneal chemotherapy versus systemic chemotherapy and palliative surgery in patients with peritoneal carcinomatosis of colorectal cancer," *Journal of Clinical Oncology,* vol. 21, pp. 3737-3743, 2003.

[194] M. Paulides, J. Bakker, E. Neufeld, J. v. d. Zee, P. Jansen, P. Levendag, and G. Van Rhoon, "The HYPERcollar: A novel applicator for hyperthermia in the head and neck*," *International Journal of Hyperthermia,* vol. 23, pp. 567-576, 2007.

[195] P. Wust, J. Nadobny, R. Felix, P. Deulhard, A. Louis, and W. John, "Strategies for optimized application of annular-phased-array systems in clinical hyperthermia," *International Journal of Hyperthermia,* vol. 7, pp. 157-173, 1991.

[196] M. Sherar, F. Liu, D. Newcombe, B. Cooper, W. Levin, W. Taylor, and J. Hunt, "Beam shaping for microwave waveguide hyperthermia applicators," *International Journal of Radiation Oncology Biology Physics,* vol. 25, pp. 849-857, 1993.

[197] J. Van Dijk, D. Gonzalez Gonzalez, L. Blank, T. Sugahara, and M. Saito, "Deep local hyperthermia with a four aperture array system of large waveguide radiators. Results of simulation and clinical application," *Hyperthermic Oncology,* vol. 1, pp. 573-575, 1988.

[198] W. Lee, E. Gelvich, P. Van Der Baan, V. Mazokhin, and G. Van Rhoon, "Assessment of the performance characteristics of a prototype 12-element capacitive contact flexible microstrip applicator (CFMA-12) for superficial hyperthermia," *International Journal of Hyperthermia,* vol. 20, pp. 607-624, 2004.

[199] S. Curto, P. McEvoy, X. Bao, and M. J. Ammann, "Compact patch antenna for electromagnetic interaction with human tissue at 434 MHz," *Antennas and Propagation, IEEE Transactions on,* vol. 57, pp. 2564-2571, 2009.

[200] H. Dobšícek Trefná, J. Vrba, and M. Persson, "Evaluation of a patch antenna applicator for time reversal hyperthemia," *International Journal of Hyperthermia,* vol. 26, pp. 185-197, 2010.

[201] P. Wust, H. Fähling, W. Wlodarczyk, M. Seebass, J. Gellermann, P. Deuflhard, and J. Nadobny, "Antenna arrays in the SIGMA-Eye applicator: Interactions and transforming networks," *Medical Physics,* vol. 28, p. 1793, 2001.

[202] P. Wust, M. Seebass, J. Nadobny, P. Deuflhard, G. Mönich, and R. Felix, "Simulation studies promote technological development of radiofrequency phased array hyperthermia," *Int J Hyperthermia,* vol. 12, pp. 477-494, 1996.

[203] M. M. Paulides, J. F. Bakker, A. P. M. Zwamborn, and G. C. van Rhoon, "A head and neck hyperthermia applicator: Theoretical antenna array design," *International Journal of Hyperthermia,* vol. 23, pp. 59-67, 2007.

[204] P. Togni, Z. Rijnen, W. Numan, R. Verhaart, J. Bakker, G. van Rhoon, and M. Paulides, "Electromagnetic redesign of the HYPERcollar applicator: toward improved deep local head-and-neck hyperthermia," *Physics in Medicine and Biology,* vol. 58, p. 5997, 2013.

[205] J. Nadobny, W. Wlodarczyk, L. Westhoff, J. Gellermann, B. Rau, G. Mönich, and P. Wust, "Development and evaluation of a three-dimensional hyperthermia applicator with Water-COated Antennas (WACOA)," *Medical Physics,* vol. 30, pp. 2052-64, 2003.

[206] M. Paulides, J. Bakker, M. Linthorst, J. Van der Zee, Z. Rijnen, E. Neufeld, P. Pattynama, P. Jansen, P. Levendag, and G. Van Rhoon, "The clinical feasibility of deep

hyperthermia treatment in the head and neck: new challenges for positioning and temperature measurement," *Physics in Medicine and Biology,* vol. 55, p. 2465, 2010.

[207] J. S. Lewin, S. G. Nour, C. F. Connell, A. Sulman, J. L. Duerk, M. I. Resnick, and J. R. Haaga, "Phase II clinical trial of interactive MR imaging–guided interstitial radiofrequency thermal ablation of primary kidney tumors: Initial experience1," *Radiology,* vol. 232, pp. 835-845, 2004.

[208] A. B. Holbrook, J. M. Santos, E. Kaye, V. Rieke, and K. B. Pauly, "Real-time MR thermometry for monitoring HIFU ablations of the liver," *Magnetic Resonance in Medicine,* vol. 63, pp. 365-373, 2010.

[209] B. Hildebrandt, J. Gellermann, H. Riess, and P. Wust, "Induced hyperthermia in the reatment of cancer," in *Cancer Management in Man: Chemotherapy, Biological Therapy, Hyperthermia and supporting Measures*, ed San Diego, USA: Springer, 2011, pp. 365-377.

[210] H. D. Trefná, P. Togni, R. Shiee, J. Vrba, and M. Persson, "Design of a wideband multi-channel system for time reversal hyperthermia," *International Journal of Hyperthermia,* vol. 28, pp. 175-183, 2012.

[211] H. D. Trefná, J. Vrba, and M. Persson, "Time-reversal focusing in microwave hyperthermia for deep-seated tumors," *Physics in Medicine and Biology,* vol. 55, p. 2167, 2010.

[212] T. Frauenrath, H. Pfeiffer, F. Hezel, M. Dieringer, L. Winter, A. Graessl, D. Santoro, O. C, W. Renz, A. Greiser, and T. Niendorf, "Lessons Learned from Cardiac MRI at 7.0T: LV Function Assessment at 3.0T Using Local Multi-Channel Transceiver Coil Arrays," in *Proceedings of the 20th Annual Meeting of ISMRM, Melbourne, Australia*, 2012.

[213] G. J. Metzger, E. J. Auerbach, C. Akgun, J. Simonson, X. Bi, K. Uğurbil, and P. F. van de Moortele, "Dynamically applied B1+ shimming solutions for non-contrast enhanced renal angiography at 7.0 tesla," *Magnetic Resonance in Medicine,* vol. 69, pp. 114-126, 2013.

[214] V. O. Boer, D. W. Klomp, C. Juchem, P. R. Luijten, and R. A. de Graaf, "Multislice 1H MRSI of the human brain at 7 T using dynamic B0 and B1 shimming," *Magnetic Resonance in Medicine,* vol. 68, pp. 662-670, 2012.

[215] L. Winter, C. Özerdem, H. Waiczies, and T. Niendorf, "Simulation of Targeted RF-Heating at 1.5T, 3.0T, 7.0T, 9.4T and 11.7T MR," *Proceedings of the 22nd Annual Meeting of ISMRM, Melbourne, Australia,* 2012.

[216] R. Compton, R. McPhedran, Z. Popovic, G. Rebeiz, P. Tong, and D. Rutledge, "Bow-tie antennas on a dielectric half-space: theory and experiment," *Antennas and Propagation, IEEE Transactions on,* vol. 35, pp. 622-631, 1987.

[217] M. Kozlov and R. Turner, "Fast MRI coil analysis based on 3-D electromagnetic and RF circuit co-simulation," *Journal of Magnetic Resonance,* vol. 200, pp. 147-152, 2009.

[218] L. I. Sacolick, F. Wiesinger, I. Hancu, and M. W. Vogel, "B1 mapping by Bloch-Siegert shift," *Magnetic Resonance in Medicine,* vol. 63, pp. 1315-1322, 2010.

[219] F. Carinci, D. Santoro, F. von Samson-Himmelstjerna, T. D. Lindel, M. A. Dieringer, and T. Niendorf, "Characterization of Phase-Based Methods Used for Transmission Field Uniformity Mapping: A Magnetic Resonance Study at 3.0 T and 7.0 T," *PLOS ONE,* vol. 8, p. e57982, 2013.

[220] Q. X. Yang, J. Wang, C. M. Collins, M. B. Smith, X. Zhang, K. Ugurbil, and W. Chen, "Phantom design method for high field MRI human systems," *Magnetic Resonance in Medicine,* vol. 52, pp. 1016-1020, 2004.

[221] M. A. Griswold, P. M. Jakob, Q. Chen, J. W. Goldfarb, W. J. Manning, R. R. Edelman, and D. K. Sodickson, "Resolution enhancement in single-shot imaging using simultaneous acquisition of spatial harmonics (SMASH)," *Magnetic Resonance in Medicine,* vol. 41, pp. 1236-1245, Jun 1999.

[222] M. Uecker, S. Zhang, and J. Frahm, "Nonlinear inverse reconstruction for real-time MRI of the human heart using undersampled radial FLASH," *Magnetic Resonance in Medicine,* vol. 63, pp. 1456-1462, 2010.

[223] K. Fuchs, F. Hezel, C. Oezerdem, A. Graessl, L. Winter, and T. Niendorf, "Cardiac FSE at 7T with improved fat and blood suppression," in *Proceedings of the Joint Annual Meeting of ISMRM-ESMRMB, Milan, Italy*, 2014.

[224] K. Fuchs, F. Hezel, C. Oezerdem, L. Winter, and T. Niendorf, "Myocardial T2* mapping free of distortion using susceptibility weighted RARE imaging at 7 Tesla," in *Proceedings of the Joint Annual Meeting of ISMRM-ESMRMB, Milan, Italy*, 2014.

[225] A. Graessl, L. Winter, C. Özerdem, F. Hezel, K. Fuchs, H. Pfeiffer, W. Hoffmann, and T. Niendorf, "A two-dimensional 16 Channel Dipole Transceiver Array for Cardiac MR at 7.0T: Design, Evaluation of RF Shimming Behavior and Application in CINE Imaging," in *Proceedings of the 21st Annual Meeting of ISMRM, Salt Lake City, UT, USA*, Salt Lake City, Utah, USA, 2013.

[226] C. A. T. Van den Berg, A. Raaijmakers, and P. R. Luijten, "Innovations in UHF-MR Technology/Methodology: An Update," in *Proceedings of the 21st Annual Meeting of ISMRM, Salt Lake City, UT, USA*, 2013.

[227] L. Winter, T. van de Lindt, C. Özerdem, W. Hoffmann, D. Santoro, A. Müller, A. Graessl, R. Seemann, J. Marek, and T. Niendorf, "Hybrid MRI/RF-Heating at 7.0 Tesla and 11.7 Tesla: Electro-Magnetic Field Simulations, Temperature Simulations/Measurements, Dipole Antenna Design and Heating Experiments," in *Proc. Intl. Soc. Magn. Reson. Med.*, 2013.

[228] P. Hasgall, E. Neufeld, M. C. Gosselin, A. Klingenböck, and N. Kuster. (2013, Version 2.4, July 30th). *IT'IS Database for thermal and electromagnetic parameters of biological tissues*. Available: www.itis.ethz.ch/database

[229] R. Eaton and C. Kmiec, "Electrical Losses in Coaxial Cables," in *International Wire & Cable Symposium*, Providence, USA, 2008.

[230] H. Fayad and P. Record, "Multi-feed dielectric resonator antenna with reconfigurable radiation pattern," *Progress In Electromagnetics Research,* vol. 76, pp. 341-356, 2007.

[231] C. Özerdem, L. Winter, K. Fuchs, and T. Niendorf, "Towards Ultimate SNR: Combination of a Multi-Element TX/RX Dipole Antenna Array with Nested and Meander Shaped RX Dipole Antenna at 7.0 Tesla," in *Proceedings of the 21st Annual Meeting of ISMRM, Salt Lake City, UT, USA*, 2013.

[232] T. Niendorf and D. K. Sodickson, "Highly accelerated cardiovascular MR imaging using many channel technology: concepts and clinical applications," *European Radiology,* vol. 18, pp. 87-102, 2008.

[233] F. Hezel, K. Fuchs, L. Winter, O. Kraus, and T. Niendorf, "Coronary MR Angiography at 7.0 Tesla Using 3D Fat-Water Separated Imaging and a Two-Dimensional 16 Channel Array of Bowtie Dipole Transceivers: A Feasibility Study," in *Proceedings of the 21st Annual Meeting of ISMRM, Salt Lake City, UT, USA*, 2013.

[234] C. Oezerdem, L. Winter, K. Fuchs, and T. Niendorf, "Towards Ultimate SNR: Combination of a Multi-Element TX/RX Dipole Antenna Array with Nested and Meander Shaped RX Dipole Antenna at 7.0 Tesla," in *4th Annual Scientific Symposium, Ultrahigh Field Magnetic Resonance: Clinical Needs, Research Promises and Technical Solutions*, 2013.

[235] N. Gudino, J. A. Heilman, M. J. Riffe, O. Heid, M. Vester, and M. A. Griswold, "On-coil multiple channel transmit system based on class-D amplification and pre-amplification with current amplitude feedback," *Magnetic Resonance in Medicine,* 2012.

Selbstständigkeitserklärung

Ich versichere hiermit, die vorliegende Dissertation selbständig und nur unter der Verwendung der angegebenen Hilfen und Hilfsmittel angefertigt zu haben.

Berlin, 25 Februar 2014

Lukas Winter